NASA-CR-204066

Final
NASA-CR
OCIT
025178

Final Technical Report

Transport Phenomena During Equiaxed Solidification of Alloys

NCC3-290

Principal Investigator: C. Beckermann
Dept. of Mechanical Engineering
The University of Iowa
Iowa City, IA 52242-1527
Phone 319/335-5681
Fax 319/335-5669

Co-Investigator: H.C. deGroh III
NASA Lewis Research Center

April 1997

ABSTRACT

Recent progress in modeling of transport phenomena during dendritic alloy solidification is reviewed. Starting from the basic theorems of volume averaging, a general multiphase modeling framework is outlined. This framework allows for the incorporation of a variety of microscale phenomena in the macroscopic transport equations. For the case of diffusion dominated solidification, a simplified set of model equations is examined in detail and validated through comparisons with numerous experimental data for both columnar and equiaxed dendritic growth. This provides a critical assessment of the various model assumptions. Models that include melt flow and solid phase transport are also discussed, although their validation is still at an early stage. Several numerical results are presented that illustrate some of the profound effects of convective transport on the final compositional and structural characteristics of a solidified part. Important issues that deserve continuing attention are identified.

NOMENCLATURE

A	interfacial surface area
A_s	area of the solid/interdendritic liquid interface
A_e	area of the dendrite envelope
C	concentration of a chemical species
c	specific heat
C_ε	settling ratio
C_p	shape factor function
d_s	mean characteristic length or diameter of the solid phase
d_e	mean characteristic diameter of the dendrite envelope
D	mass diffusion coefficient
G	temperature gradient
h	chill heat transfer coefficient or enthalpy
Iv	Ivantsov function
$\mathbf{j}$	species diffusion flux
J	interfacial species transfer rate per unit of volume
k	thermal conductivity
l	species diffusion length
m_l	liquidus line slope
M_s^d	solid/liquid interfacial drag
n	equiaxed nuclei density
$\dot{n}$	nucleation rate
$\mathbf{n}$	outwardly directed unit normal vector
Pe	envelope growth Peclet number, $\bar{w}_{ne}R_f/D_l$
Pe_ε	multiphase Pelcet number, $\varepsilon_l\lvert v_l - v_s\rvert d_e/D_l$
Pe_t	solutal Peclet number at the dendrite tip, $V_tR_t/2D_l$
Pe_∞	ambient Pelcet number for dendrite tips, $\lvert v_l - v_s\rvert R_t/D_l$

q_{ext} external heat flux

R radius

S interfacial area concentration

t time

T temperature

$\dot{T}$ cooling rate, $\partial T/\partial t$

v velocity

V_k volume of phase k

V_o averaging volume

V_t dendrite tip velocity

w interface velocity

X phase function

Greek Symbols

α diffusion Fourier number, $4D_s t_f/\lambda_2^2$

β dimensionless parameter, Eq.(82)

Γ interfacial phase change rate or Gibbs-Thomson coefficient

Δh latent heat of phase change

ΔT undercooling

ε volume fraction

ε_{si} internal solid fraction, $\varepsilon_s/(\varepsilon_s + \varepsilon_d)$

κ partition coefficient

κ_v flow partition coefficient

λ dendrite arm spacing

λ_p slip coefficient for solid

ϕ shape factor

ρ density

μ	viscosity
σ^*	stability constant
τ	shear stress
Ψ	a field property
Ω	solutal supersaturation

Subscripts

d	interdendritic liquid
e	dendrite envelope
E	eutectic point
f	total liquid phase (d+l)
g	grain
j	phase j
k	phase k
kj	pertinent to phase k on the k-j interface
l	extradendritic liquid
L	liquidus
ld	pertinent to the extradendritic liquid at the inter- and extra-dendritic liquid interface
ls	pertinent to the liquid phase at the solid-liquid interface
m	melting point of pure metals
n	normal direction
N	nucleation
o	initial state
s	solid
sd	pertinent to the solid phase at the solid-interdendritic liquid interface
sl	pertinent to the solid phase at the solid-liquid interface
t	dendrite tip or tangential

w wall

1 primary

2 secondary

Superscripts

c critical

j due to species gradients

t macroscopic dispersion

Γ due to interface movement

- interfacial area-averaged

* effective

^ fluctuating component

1. INTRODUCTION

Microstructural evolution and the distribution of phases and species are some of the most fundamental and important issues in the science and technology of solidification of metal alloys. The structure determines the mechanical properties of a casting or weld, and certain chemical inhomogeneities can cause serious defects. Therefore, the metallurgist has a keen interest in understanding, modeling, and controlling the physical phenomena occurring during the liquid to solid transformation. For millennia, the optimization of material properties essentially relied on a trial-and-error process, where different melt compositions and casting practices were tried and the structure and properties of the solidified part were subsequently examined. It was not until the advent of computers that numerical solutions of the heat equation could be used to analyze casting and welding processes. The connection to microstructure predictions was made by the early work of Oldfield [1] on cast iron in the late 1960s. Almost at the same time, Flemings and coworkers [2,3] started to model melt flow during solidification in order to predict

compositional inhomogeneities, i.e., macrosegregation, on the scale of a casting. Significant progress in rigorously linking microstructural evolution relations to macroscopic (system scale) heat flow calculations has only been made since the mid-1980s. Similarly, but separately, the calculation of melt flow, solid phase transport, and macrosegregation did not become commonplace until fully coupled numerical methods for solving the Navier-Stokes equations reached a considerable level of maturity, in the 1980s. Although there is a tight coupling between microstructure and convective transport, the simultaneous prediction of both has only been attempted in the 1990s. Numerous recent reviews are available that summarize the progress in these areas [4-11], and the latest developments can be found in conference proceedings [12-15].

Solidification of metal alloys is characterized by the presence of a variety of microscopically complex interfacial structures. The most common structure is the dendrite, which can either exist in a columnar or equiaxed form, as illustrated in Fig.1a. The macroscopic region over which such solid/liquid interfaces exist is loosely termed the mushy zone, so as to distinguish it from the pure liquid and fully solidified regions, see Fig.1b. The mushy zone is roughly bounded by the solidus and liquidus isotherms, which can be obtained for a given alloy composition from an equilibrium phase diagram. For the simple phase diagram shown in Fig.1c, the last liquid to solidify is often of the eutectic composition, and the eutectic reaction transforms this liquid into the α and β solid phases. The phase diagram also describes the different solubilities of the solute in the solid and liquid phases as a function of temperature. The segregation of solute at the solid/liquid interface causes the establishment of microscopic concentration gradients in the liquid and solid phases on both sides of the interface, and, in the presence of convection, large-scale compositional inhomogeneities. These and other basics of alloy solidification are well explained in textbooks [3, 16-18].

From a thermal scientist's perspective, the mushy zone can be viewed as a multiphase, multicomponent system with phase change, featuring multiple and disparate microscopic

interfacial length scales. Just as in boiling of liquid mixtures, the system-scale transport of the phases (solid and liquid) by convection, together with heat transfer and solute redistribution, play important roles. Furthermore, the nucleation, growth, and morphology of the evolving phase(s) need careful consideration. However, there are numerous issues that are unique to alloy solidification, the most important of which is the preservation of the microstructure and compositional inhomogeneities in the solidified material. As in the more recent analyses of other multiphase systems, solidification is starting to be modeled using rigorously derived continuum conservation equations [8]. In this regard, the incorporation of proper constitutive relations describing the interface topology and the phase interactions on a microscopic scale continues to be the main challenge. Although the study of microscopic phase interactions during solidification is a time-honored area within metallurgy [18], much of the available information remains empirical. For example, it is still largely impossible to quantify the interactions between an evolving microstructure and convective melt flow. In fact, it can safely be said that the prediction of the structural and compositional features of a solidified metal alloy on the scale of a casting or weld is still more an art than science.

The purpose of this chapter is to review some of the most recent modeling work on alloy solidification, where a tight coupling between microstructure and transport phenomena at both microscopic and macroscopic scales is pursued. The emphasis is on fundamentals and on exposing areas of future research. Despite the fact that some of the recent work is already being applied to industrially relevant multicomponent alloys and real shaped castings (see [15]), the review is limited to primary dendritic solidification of binary alloys in simple molds.

The following section gives several examples of experiments that illustrate important micro-/macroscopic aspects of alloy solidification. Section 3 discusses the general modeling approach propagated here. In order to provide some perspective to the many modeling issues involved, Section 4 concentrates on studies that consider diffusional

transport only. The inclusion of melt convection and the transport of solid phases is reviewed in Section 5, while the conclusions and recommendations for future research are summarized in Section 6.

2. OBSERVATIONS OF MICRO-MACROSCOPIC PHENOMENA IN ALLOY SOLIDIFICATION

Figure 2a shows a typical columnar dendritic mushy zone for solidification from below of the transparent model alloy SCN-ethanol, with a close-up of the dendrite tip region provided in the lower portion of Fig.2b [19]. On the microscopic scale, we observe a porous structure consisting of primary, secondary and higher order dendrite arms. In the figure, the primary dendrite arm spacing is roughly 0.4 mm. The structure in the tip region is highly irregular, and it is shown below that the growth kinetics of the dendrite tips play a special role. The tips grow into an undercooled melt, which can be inferred from the presence of growing equiaxed crystals above the columnar front (Fig.2b). Undercooling refers to the melt being in a metastable state below the equilibrium liquidus line and represents the driving force for dendrite tip growth. On a larger scale, it can be seen that the primary dendrites do not exactly grow in a direction opposite to the heat flow (Fig.2a). Each cluster of dendrites having the same orientation constitutes a crystal or grain, and the boundaries between the grains are a common feature of etched cross sections of solidified metal alloys (see below).

Much research has been performed to predict the microstructural features in dendritic solidification. Important considerations are the stability of a solid/liquid interface, coarsening or ripening of the smallest-scale dendrite arms as a function of time, and the growth velocity and radius of the dendrite tip. Some of the available semi-empirical relations are presented below in Section 4. Almost all quantitative information is limited to diffusion-controlled solidification, and the important effects of convection are mostly ignored in the metallurgical literature. The dendritic structure persists in the as-cast alloy

due to its compositionally segregated nature (microsegregation). Second (solid) phases, such as the eutectic, and microporosity are usually found in the interdendritic spaces.

The microstructure also controls the melt flow through the porous mushy zone during solidification and, thus, the occurrence of macrosegregation. Furthermore, flow/dendrite interactions may play an important role in generating free equiaxed crystals. Figure 3 illustrates the formation of a channel in a columnar dendritic mushy zone due to local flow instabilities [20]. Such flow channels cause severe macrosegregation in the form of A-segregates or freckles in castings. Fragmentation of the dendritic structure within the channels (Fig.3b) and the subsequent ejection of fragments by the flow (Fig.3a) is one of the mechanisms associated with the formation of equiaxed grains (see below).

Figure 4 illustrates several additional aspects of equiaxed solidification. The experiments [21] were performed using the transparent NH_4Cl-H_2O model solution. On the macroscopic scale, a swarm of freely moving crystals exists in the upper portion of the test cell, while the lower portion consists of a packed bed of sedimented crystals. Figure 4a is a shadowgraph image, visualizing the density gradients in the melt. A close inspection reveals the presence of a solutal plume in the wake of each sedimenting crystal, implying that the crystals are growing while moving through the undercooled melt (the latent heat as well as the solute are rejected into the liquid phase). The irregular nature of the packed bed is caused by the complex thermosolutal convection currents in the melt. An important issue is the mechanisms associated with the origin of the equiaxed grains and their number density. Numerous theories have been put forward and quantitative models are not available. The theories can be roughly divided into two groups [22]: (i) heterogeneous nucleation in the bulk melt, which can be promoted through the use of grain refiners (inoculants) and (ii) separation of small dendrite fragments from the mold wall, the upper free liquid surface or already existing columnar dendrites through mechanical forces or, more likely, a localized remelting ("pinch off") process. In the latter mechanism, melt

convection is necessary to transport the fragments into the interior bulk liquid where they may survive and grow into equiaxed crystals.

A fine equiaxed grain structure is often preferred over a columnar structure for a number of reasons (single-crystal turbine blades are an important exception) [23]: (i) uniform mechanical properties and better overall strength and fatigue life, (ii) more finely dispersed second phases and porosity, (iii) less macrosegregation, (iv) improved feeding to compensate for shrinkage and less hot cracking, (v) improved surface properties, and (vi) improved machinability and fabricability. However, in many castings and welds a mixed columnar/equiaxed grain structure is present and it becomes crucial to understand and control the columnar-to-equiaxed transition (CET). A large number of studies have tried to clarify the main factors that influence the CET (Wang and Beckermann [24] review some of them). As an example, consider the simple one-dimensional casting experiments by Ziv and Weinberg [25]. Here, an Al-3wt% Cu alloy was unidirectionally solidified from below. The overall configuration is thermally and solutally stable, thus minimizing the influence of melt convection. Figure 5a shows a sequence of grain structures where the heat transfer coefficient at the bottom was varied. It can be seen that the length of the columnar region increases with stronger cooling. It is clear that a simple heat flow and solid fraction evolution model would not capture this effect. Obviously, a detailed consideration of the competitive growth of columnar and equiaxed crystals on a microscopic scale is necessary. A yet more intriguing effect is shown in Fig.5b, where the cooling rate and all other conditions were identical, except for the addition of minute amounts of a grain refiner (here TiB_2). With increasing amounts of grain refiner, the structure changes from a coarse-grained mixed structure to a fine-grained fully equiaxed one. Other experiments have examined the influences of initial melt superheat, melt composition, mold surface roughness, mold vibration, mold rotation, stirring, and others. Interesting accounts of this research can be found in [26]. These effects have been understood on a qualitative level for decades. Nonetheless, the prediction of the nature and size distribution of grains in

solidified metal alloys has been largely prevented by the intricate physical phenomena involved.

Examples of the effects of microstructure on macroscopic transport are provided in Figs. 6 to 8. Finn et al. [27] performed experiments on continuous casting of a round Al-4.5wt% Cu ingot in the configuration illustrated in Fig.6a. The superheated alloy is poured into the water cooled mold at the same mass flow rate at which the casting is withdrawn at the bottom. Macrosegregation data are shown in Fig.6b for two different experiments. No grain refiner was used in the first experiment, and the microstructure was columnar dendritic as shown in Fig.6c. In the second experiment, the use of a grain refiner resulted in the mixed globular-dendritic equiaxed structure of Fig.6d throughout most of the ingot cross section. The macrosegregation profiles for both experiments show strong positive segregation near the ingot surface (termed inverse segregation), which can be explained by solidification contraction and back flow of Cu-enriched liquid through the coherent ingot shell first formed in the mold [27]. Large differences in the macrosegregation profiles between the two experiments can be observed near the centerline (Fig.6b). These differences were attributed to the influence of the microstructure on the resistance it offers to the interdendritic melt flow, as characterized by the permeability of the mushy zone. In the highly dendritic columnar case without grain refiner, the relatively dense and impermeable mushy region prohibited the advection of enriched interdendritic liquid to the ingot centerline, resulting in negative centerline segregation. On the other hand, the more coarse and permeable equiaxed structure of the grain refined ingot allowed for the advection of enriched fluid toward the centerline producing positive segregation there [27]. This positive centerline macrosegregation does not support previous theories on how the transport and settling of free, unattached, solute lean dendrites causes negative centerline segregation [28]. However, the detection of a duplex structure, consisting of a mixture of fine dendrites and coarse equiaxed grains, near the centerline in the grain refined case (Fig.6d) can be regarded as an indication of the presence of solid phase transport.

Obviously, the ability to model and predict the microstructural evolution together with the melt flow, solid transport, heat transfer, and advection of solute would have a strong impact on understanding and controlling these undesirable macrosegregation patterns.

Another example of the interplay between grain structure and macrosegregation is provided in Fig.7. Figures 7a and 7b are cross sections from a low-alloy steel casting solidified in a simple sand mold [29]. Figure 7a clearly shows an inner equiaxed zone in addition to the columnar dendrites extending from the mold walls. In Fig.7b, the point of significance here is the negative carbon macrosegregation region that directly corresponds to the inner equiaxed zone. Although such observations are not new, the detailed transport phenomena leading to the negative segregation in equiaxed solidification, as well as the interactions between equiaxed and columnar growth, are poorly understood.

As already mentioned, one issue that seriously hampers present modeling efforts is the uncertainty associated with the origin of the equiaxed crystals and their transport. Figure 8 illustrates the settling of equiaxed crystals in a solidifying Pb-Sn eutectic alloy [30]. The micrographs indicate the presence of equiaxed, Pb-rich crystals both near the bottom of the sample and above a stainless steel screen which was inserted near the center. As expected, the corresponding macrosegregation pattern shows a strong increase in the Pb concentration towards the screen and the sample bottom, with a ~20% jump at the location of the screen. This experiment is especially intricate, because the eutectic melt was substantially undercooled before solidification. Without undercooling the entire sample would consist of a eutectic structure with no appreciable macrosegregation [30]. The undercooling causes the primary Pb phase to nucleate first. The Pb-rich crystals settle down and leave a Sn-rich melt behind, so that primary Sn-rich dendrites grow in a columnar fashion both from the top and below the screen. Eutectic exists only between the columnar and equiaxed regions. Apparently, the modeling of the nucleation in the undercooled melt requires a thorough understanding of the interfacial energies in the Pb-Sn system and other non-equilibrium thermodynamics issues.

This section has illustrated no more than a few examples of the complex nucleation, growth, and transport phenomena occurring in alloy solidification. In every case, their modeling involves detailed and simultaneous consideration of processes occurring over multiple and disparate length (or time) scales. It should be clear now that the mushy zone is not just a porous medium of some average structure with the melt flowing through it. Instead, alloy solidification is a physically rich area that has evaded modeling efforts except in a few limiting cases.

3. BASIC MODELING CONSIDERATIONS

Modeling of transport phenomena occurring during dendritic alloy solidification has received considerable research attention in the past several decades [8,10]. Recently, interest has been focusing on an important and promising approach, namely micro-macroscopic modeling. The main goal of this approach is to incorporate descriptions of fundamental microscopic phenomena, such as nucleation, undercooling and grain growth, into macroscopic heat flow calculations in order to predict microstructure formation of a solidifying material on the system scale. Reviews of micro-macroscopic modeling have been provided by Rappaz [4] and Stefanescu [9].

In an attempt to achieve detailed coupling between micro- and macroscopic phenomena, Ni and Beckermann [31] proposed a two-phase model for mass, momentum, energy and species transport in a solidifying system. The model is formulated by viewing the solid and liquid phases separately and averaging the field properties of each phase over a representative elementary volume (REV). Through the volume averaging process, phase interaction terms appear in the resulting macroscopic balance equations that reflect the effects of the transport phenomena occurring on the microscopic scale. These interaction terms are all proportional to the solid/liquid interfacial area per unit volume, which represents the sole microscopic length scale. The same volume averaging technique was employed by Ganesan and Poirier [32] to derive macroscopic mass and momentum equations for a stationary solid phase.

Nevertheless, volume averaged two-phase models are not well suited for incorporating microstructural features present in dendritic solidification. This problem originates from the single-scale averaged description of phase behaviors. In traditional volume averaging, no distinction is made between properties of a phase associated with different microscopic length scales. The phenomena occurring on various microscopic length scales are smeared and modeled using a single mean characteristic length (i.e., the interfacial area concentration). Referring back to Fig.2, it can be seen that, in dendritic growth there exist

at least three disparate microscopic length scales that are smaller than the characteristic size of an averaging volume: (i) the overall size of the crystal or the primary dendrite arm spacing, (ii) the secondary and higher-order dendrite arm spacings, and (iii) the radius of a dendrite tip. The transport phenomena occurring on the various microscopic scales differ greatly from one another and cannot be well described based on a single mean characteristic length, although they are all taking place within the same averaging volume. In other words, a single-scale model provides insufficient resolution to capture dynamic behaviors on several microscopic length scales. Such resolution is, however, required for the complete incorporation of microscopic effects in a macroscopic model and the prediction of microstructure formation in a solidifying system.

Considerable progress has been made to account for the heterogeneous nature of microstructures in the micro-macroscopic modeling of both equiaxed [33-35] and columnar [36,37] dendritic solidification. In the models of equiaxed dendritic growth, the necessary resolution is obtained by viewing the liquid phase in a control volume as two distinct fluids associated with two length scales: the liquid within the dendritic structure and the liquid outside the equiaxed grain. It is then possible to separately account for the different solute diffusion phenomena in the interdendritic structure and the dendrite tip region, and more importantly, to incorporate a growth model for the dendrite tips. Similarly, when analyzing columnar dendritic solidification, Flood and Hunt [36] distinguish between the liquid in the interdendritic region and that outside the columnar front, and also take into account the undercooling at the primary dendrite tips.

Although these recent investigations have obtained successful results, they fail to provide a consistent and general framework for micro-macroscopic modeling of dendritic solidification. For example, in Dustin and Kurz's model [33] of equiaxed growth and in Flood and Hunt's model [36] of columnar solidification, the growth model for the dendrite tips is introduced at the expense of not conserving solute outside of the grain envelope or at the columnar front [4]. The same practice was repeated by Kerr et al. [38]. A model that

not only conserves solute but also incorporates a dendrite tip growth model in a rigorous and consistent manner is due to Rappaz and Thevoz [34]. Unfortunately, lengthy calculations are required to obtain the microscopic solute profile outside each equiaxed grain, which limits its utility in a macroscopic model. Although the analytical version of the model [35] is suitable for incorporation into a macroscopic model, it is implied that the average concentration of the liquid outside of the grain remains at its initial value, which may not be valid in some cases (e.g., in the presence of macrosegregation). Finally, none of the previously mentioned micro-macroscopic models accounts for finite-rate solute diffusion in the solid on a microscopic scale.

More recently, Wang and Beckermann [24, 39-41] developed a unified model for both equiaxed and columnar dendritic solidification, that is based on a multiphase approach and volume averaging. The basic modeling approach is introduced in the next subsections, while more details and applications are discussed in Sections 4 and 5.

3.1 Multiphase Approach

Consider a small volume element that contains several equiaxed or columnar dendritic crystals, as schematically illustrated in Fig.9. An interfacial scale (having the unit of length) is defined as the ratio of the volume of the structure to the interfacial area, so that two different interfacial length scales can be distinguished in Fig.9. In the equiaxed case, the solid crystal and the interdendritic liquid share a common interfacial length scale of 10^{-6} to 10^{-5} m, whereas the interface between the liquid outside the grains and the interdendritic liquid has a larger length scale (of the order of 10^{-4} to 10^{-3} m). The same is true for the columnar case, if one notes the difference between the primary and higher-order arm spacings (see Fig.9b). The size of the volume element is chosen such that it is much larger than all interfacial length scales, but small compared to the system scale (of the order of 10^{-1} to 10^{0} m). Hence, a proper volume element could have a radius between 10^{-3} and 10^{-2} m. A volume element of this size is what all macroscopic models are actually based on.

The hypothetical interface between the interdendritic liquid and the liquid outside the crystals is referred to as the dendrite envelope. The specification of this envelope is somewhat subjective. However, a reasonable choice appears to be a smooth surface connecting the primary and secondary dendrite arm tips, as shown by the interrupted line in Fig.9. More details on the envelope topology can be found below.

Based on the above discussion, the volume element can now be considered to consist of three different phases: the solid phase and the two liquid phases. The two liquid phases separated by the dendrite envelope are distinguished by their different interfacial length scales. This multiphase approach to a heterogeneous system is realistic since a fluid within a structure of a larger scale really could have different macroscopic properties than the same fluid in a smaller scale structure. It has long been recognized that the effective transport properties of a fluid within a microstructure are not only dependent on its physical properties, but also on the geometry of the structure [42-44].

In the multiphase approach, separate macroscopic conservation equations are formulated for each phase. These macroscopic equations are linked through interfacial transfer terms, which reflect the microscopic transport phenomena present at the interfaces. The new interface between the two liquid phases (i.e., the envelope), thus, provides an opportunity to incorporate additional microscopic phenomena in the model and transmit information from the two different length scales into the macroscopic equations. The macroscopic conservation equations are derived using the volume averaging technique, which is described next.

3.2 Volume Averaging

Volume averaging has been a popular technique to derive macroscopic conservation equations for multiphase transport phenomena with and without phase change. In its application to solidification, a number of advantages have been pointed out [31]. Volume averaging shows how the various terms in the macroscopic equations arise and how the

resulting macroscopic variables are related to the corresponding microscopic ones. This gives considerable insight into the formulation of constitutive relations for the incorporation of the microscopic phenomena. In this work on heterogeneous solidification systems, volume averaging is also attractive because it shows how physical phenomena occurring on one length scale are linked to those on another scale in a macroscopic description.

The averaging volume, V_o, is shown in Fig.9. Rigorously, the spatial smoothing of a physical property belonging to the smaller scale phase over the averaging volume, V_o, requires the knowledge of the transport equations first averaged over a smaller volume. Hence, in order to develop a macroscopic equation for the smaller scale phase in a heterogeneous system, based on the volume V_o, the microscopic or *point* equation must be spatially averaged successively over two averaging volumes of different size. This is the basic idea underlying the so-called dual-scale volume averaging technique that was recently developed by Wang and Beckermann [45]. However, the averaging theorems established for that technique reduce identically to those in the conventional volume averaging method, if it is assumed that the smaller averaging volume is spatially independent (but it can be time dependent) inside the larger volume, V_o. Therefore, for the sake of simplicity, the conventional volume averaging method is employed here, and each fluid having a distinct length scale is viewed as a separate phase. Since the details of the method have been well documented [46-49], only the averaging theorems are provided in the following:

$$\left\langle \frac{\partial \Psi_k}{\partial t} \right\rangle = \frac{\partial \langle \Psi_k \rangle}{\partial t} - \frac{1}{V_o} \int_{A_k} \Psi_k \mathbf{w} \cdot \mathbf{n} \, dA \tag{1}$$

$$\langle \nabla \Psi_k \rangle = \nabla \langle \Psi_k \rangle + \frac{1}{V_o} \int_{A_k} \Psi_k \mathbf{n} \, dA \tag{2}$$

where the averaging operator and the intrinsic volume average are defined, respectively, as

$$\langle \Psi_k \rangle = \frac{1}{V_o} \int_{V_o} X_k \Psi_k \, dV \tag{3}$$

$$\langle \Psi_k \rangle^k = \frac{1}{V_k} \int_{V_o} X_k \Psi_k dV \tag{4}$$

with X_k denoting a phase function, equal to unity in phase k and zero elsewhere, and V_k is the volume of phase k in V_o.

The factor **n** in Eqs.(1) and (2) denotes the outwardly directed unit vector normal to an interface, and **w** is the velocity of the interface. Note that A_k stands for the total interfacial area of the k-phase adjacent to all other phases j; i.e.,

$$A_k = \sum_{j,j \neq k} A_{kj} \tag{5}$$

For Ψ_k=1, we obtain from Eq.(3) the definition of the volume fraction, ε_k, as

$$\varepsilon_k = V_k / V_o \tag{6}$$

In addition, it follows that

$$\sum \varepsilon_k = 1 \tag{7}$$

and

$$\langle \Psi_k \rangle = \varepsilon_k \langle \Psi_k \rangle^k \tag{8}$$

Furthermore, the fluctuating component of Ψ_k can be defined as

$$\hat{\Psi}_k = \Psi_k - \langle \Psi_k \rangle^k \tag{9}$$

3.3 Macroscopic Equations

The microscopic (point) equations governing mass, momentum, energy, and species conservation within a phase k are summarized in the first colunm of Table 1. Through integration over V_o, and making use of Eqs.(1) and (2), the corresponding macroscopic equations and interfacial balances can be derived. The details of the derivations have been well documented [8, 46-50], and only the final, simplified result is shown in Table 1. All interfacial integrals are already modeled using well-accepted basic constitutive relations (e.g., see [31]). The overbar denotes interfacial quantities. The volume-averaged diffusive

fluxes and the shear stress may be modeled by introducing effective (macroscopic) diffusion coefficients and viscosities, which depend on the microstructure, and the fluctuating components of the thermophysical properties may be neglected (see below). The dispersive fluxes are left unmodeled in the averaged equations.

At this point, the macroscopic equations in Table 1 are valid for almost any multiphase system. The adaptation to alloy solidification requires careful specification of the interfacial area relations, interfacial transport coefficients, and other supplementary relations, in accordance with the multi-phase/-scale approach outlined in Section 3.1. This is illustrated in Sections 4 and 5 for diffusion-controlled and convection-dominated dendritic alloy solidification, respectively.

4. DIFFUSIONAL TRANSPORT IN DENDRITIC ALLOY SOLIDIFICATION

The vast majority of alloy solidification models neglects melt convection and solid phase transport. Such a simplification is quite instructive from a fundamental point of view, but cannot be justified for most real solidification processes. Nonetheless, this section attempts to provide a unified overview of present diffusional theories of dendritic alloy solidification.

4.1 Reduced Macroscopic Equations

With $\mathbf{v}_k=0$, the averaged equations of Table 1 reduce to relatively simple heat and solute diffusion equations for each phase k together with the mass conservation equations and the interfacial mass, energy, and solute balances. Before embarking on their solution, it is important to examine the time (or length) scales for heat and solute diffusion. The Lewis number (i.e., the ratio of the thermal to the mass diffusivity) of metal alloys in the liquid state is of the order of 10^4. In the solid state it is even higher. A straightforward analysis then shows that, for common solidification and cooling rates, (i) the phases in the averaging volume can be assumed to be in thermal equilibrium so that the averaging volume is isothermal, and (ii) solute diffusion on the macroscopic scale does not need to be considered. Under the first assumption, the energy equations for each phase can be added up and a single heat conduction equation can be written for the mixture temperature:

$$\rho c \frac{\partial T}{\partial t} = \nabla\cdot(k\nabla T) + \rho\Delta h \frac{\partial \varepsilon_s}{\partial t} \qquad (10)$$

where ρc and k are the mixture thermal capacitance and effective thermal conductivity, respectively. The last term on the RHS of Eq.(10) arises from converting the phase enthalpies to temperature and accounts for the latent heat release in the mushy zone due to an increase in the solid volume fraction, ε_s. Equation (10) is valid for all phase volume

fractions and reduces to the correct limits in the pure solid and liquid regions. The validity of Eq.(10) is examined in more detail in [8].

With the neglect of macroscopic solute diffusion, the mass and solute conservation equations for a phase k reduce to

$$\frac{\partial}{\partial t}(\varepsilon_k \rho_k) = \sum_{(j,\, j\neq k)} \Gamma_{kj} = \sum_{(j,\, j\neq k)} S_{kj}\rho_k \overline{w}_{nkj} \tag{11}$$

$$\frac{\partial}{\partial t}(\varepsilon_k \rho_k \langle C_k \rangle^k) = \sum_{(j,\, j\neq k)} J_{kj} = \sum_{(j,\, j\neq k)} (J^{\Gamma}_{kj} + J^{j}_{kj})$$

$$= \sum_{(j,\, j\neq k)} \left[\Gamma_{kj}\overline{C}_{kj} + \frac{S_{kj}\rho_k D_k}{l_{kj}} (\overline{C}_{kj} - \langle C_k \rangle^k)\right] \tag{12}$$

and the interfacial balances

$$\Gamma_{kj} + \Gamma_{jk} = 0 \quad \text{and} \quad J_{kj} + J_{jk} = 0 \tag{13}$$

where $\overline{w}_{nkj}$ and S_{kj} $(=A_{kj}/V_o)$ are the normal velocity and the area concentration, respectively, of the interface between phases k and j. Other symbols are defined in the Nomenclature.

In accordance with the multiphase approach for dendritic solidification outlined in Section 3, we will consider a three-phase system consisting of the solid (k=s), the interdendritic liquid (k=d), and the extradendritic liquid outside the dendrite envelope (k=l), so that $\varepsilon_s + \varepsilon_d + \varepsilon_l = 1$. It is further assumed that according to Fig.9 the dendrite tips have only pointwise contact with the dendrite envelope. Hence,

$$S_{sd} = S_{ds} = S_s; \quad S_{dl} = S_{ld} = S_e \quad \text{and} \quad S_{sl} = S_{ls} = 0$$

$$\overline{w}_{nsd} = -\overline{w}_{nds} = \overline{w}_{ns}\,; \quad \overline{w}_{ndl} = -\overline{w}_{nld} = \overline{w}_{ne} \tag{14}$$

These relations imply that there exists no direct coupling between phases s and l, while phase d interacts with both phases s and l. At the d-l interface, phases d and l are actually the same liquid, so that

$$\overline{C}_{dl} = \overline{C}_{ld} = \overline{C}_e \tag{15}$$

where subscript e in the above two equations denotes the dendrite envelope. At the s-d interface local thermodynamic equilibrium prevails, and the linearized liquidus and solidus lines of the equilibrium phase diagram (Fig.1c) give the following

$$\bar{C}_{sd}/\ \bar{C}_{ds} = \kappa; \quad \bar{C}_{ds} = \frac{T - T_m}{m_l} \tag{16}$$

Assuming further that the densities of the liquid and solid phases are equal and constant, the mass conservation equations can be written as

$$\frac{d\varepsilon_s}{dt} = S_s \bar{w}_{ns} \tag{17}$$

$$\frac{d}{dt}(\varepsilon_s+\varepsilon_d) = -\frac{d\varepsilon_l}{dt} = S_e \bar{w}_{ne} \tag{18}$$

and, after a few manipulations [39], the solute balances become

phase s

$$\frac{\partial(\varepsilon_s<C_s>^s)}{\partial t} = \bar{C}_{sd}\frac{\partial \varepsilon_s}{\partial t} + \frac{S_s D_s}{l_{sd}}(\bar{C}_{sd} - <C_s>^s) \tag{19}$$

phase d

$$\frac{\partial(\varepsilon_d<C_d>^d)}{\partial t} = (\bar{C}_e - \bar{C}_{ds})\frac{\partial \varepsilon_s}{\partial t} + \bar{C}_e\frac{\partial \varepsilon_d}{\partial t} + \frac{S_s D_l}{l_{ds}}(\bar{C}_{ds} - <C_d>^d) + \frac{S_e D_l}{l_{dl}}(\bar{C}_e - <C_d>^d) \tag{20}$$

phase l

$$\frac{\partial(\varepsilon_l<C_l>^l)}{\partial t} = \bar{C}_e\frac{\partial \varepsilon_l}{\partial t} + \frac{S_e D_l}{l_{ld}}(\bar{C}_e - <C_l>^l) \tag{21}$$

s-d interface

$$(\bar{C}_{ds} - \bar{C}_{sd})\frac{\partial \varepsilon_s}{\partial t} = \frac{S_s D_l}{l_{ds}}(\bar{C}_{ds} - <C_d>^d) + \frac{S_s D_s}{l_{sd}}(\bar{C}_{sd} - <C_s>^s) \tag{22}$$

d-l interface (dendrite envelope)

$$\bar{C}_e = \frac{\frac{1}{l_{ld}}<C_l>^l + \frac{1}{l_{dl}}<C_d>^d}{\frac{1}{l_{ld}} + \frac{1}{l_{dl}}} \tag{23}$$

The meanings of the various solute diffusion lengths, l_{kj}, in the present three-phase system are schematically illustrated in Fig.10 and further discussed in Section 4.3. Geometrical

relations for the interfacial area concentrations, S_s and S_e, are derived in Section 4.2. Because the normal envelope velocity, $\bar{w}_e$, does not appear in Eq.(23) (since $\bar{C}_{dl} = \bar{C}_{ld}$), the kinetics of the dendrite envelope need to be prescribed separately, which is shown in Section 4.4. Otherwise, the above equations constitute a full system for the unknown volume fractions, concentrations, and temperature, if supplemented by proper initial and boundary conditions.

It is noteworthy that all model equations have clear physical interpretations. For example, Eq.(19) simply states that the change in mass of solute in the solid results from the combined contributions of movement of the solid/liquid interface and solute diffusion across the interface. The solute balance at the s-d interface, Eq.(22), implies that the solute rejected during phase change is diffused into both the solid and interdendritic liquid phases. Finally, Eq.(23) indicates that the concentration at the envelope interface, $\bar{C}_e$, is a diffusion-resistance weighted mean of the averaged concentrations in the adjacent phases, since no phase change occurs at this interface.

Another salient feature of the present model is that it provides the same set of conservation equations for both equiaxed and columnar dendritic solidification. In other words, the model represents a unified theoretical framework for both modes of solidification, while leaving descriptions of the different physical characteristics of each mode to supplementary relations, as shown next.

4.2 Morphological Relations

The interfacial area concentrations, S_s and S_e, characterize the topology of the interfacial structures, and are thus related to complex microscopic phenomena, such as the growth of various solid microstructures, impingement of interfaces and coarsening of dendrite arms. The area concentrations play important roles in the modeling of the interfacial transfer terms and need to be modeled through supplementary relations, which can be developed from either experiments or certain theoretical considerations. In fact, it

has recently been proposed to base micro-macroscopic models directly on the specific surface area, S_v [51]. The inverse of the specific surface area is a more accurate measure of the length scale of a microstructure than the traditionally employed spacings and can easily be measured. The interfacial area concentration, S, is related to S_v by $S = S_v(1-\varepsilon)$, where ε is the volume fraction of the microstructure under consideration. Hence, once relations for S_v become available, they can be used in the present model.

In the following, a more traditional approach is taken, and an attempt is made to relate the interfacial area concentrations to certain dendrite spacings, the nuclei density, time (through coarsening), and the various volume fractions (which are also functions of time). In the present model, different length scales have been distinguished and, thus, it is possible to relate the interfacial area concentrations to such metallurgical parameters. This also enables the incorporation of microstructural phenomena (e.g., coarsening) that occur only on a particular length scale [52]. This matter is obscured in regular two-phase models through the use of mean geometrical parameters for the averaging volume [31].

4.2.1 Solid/Liquid Interface. The area concentration of the interface between the solid and the interdendritic liquid can be modeled by assuming a simple one-dimensional plate-like geometry of the secondary dendrite arms as shown in Fig.11. This is applicable to both equiaxed and columnar structures and is traditionally adopted in most microscopic analyses. For such a geometry, it is readily shown that

$$d_s = \frac{\varepsilon_s \lambda_2}{1-\varepsilon_l} \tag{24}$$

and

$$S_s = \frac{2}{\lambda_2} \tag{25}$$

Substituting Eq.(24) into Eq.(25), we obtain a relation between S_s and the mean characteristic length (diameter) as

$$S_s = \frac{2\varepsilon_s}{(1-\varepsilon_l)d_s} \tag{26}$$

It is interesting to see that this result matches well with the general expressions obtained by DeHoff and Rhines [53] and Bird et al. [54]. The numerical factor can be adjusted for other choices of the geometry. In addition, we note that Eq.(25) is ready for the incorporation of the coarsening effect. For example, by using the coarsening law established by Kattamis et al. [55]:

$$\lambda_2 = \beta t_a^{1/3} \tag{27}$$

Eq.(25) gives

$$S_S \sim t_a^{-1/3} \tag{28}$$

where t_a is the local 'aging' time. This result is consistent with the coarsening experiments conducted by Marsh and Glicksman [56] at a constant solid fraction.

Note that due to the assumption of a one-dimensional plate-like geometry for the solid/liquid interface, the interfacial area concentration, S_S, is not an explicit function of the solid volume fraction (but S_V is; see above). This may not be a good approximation during the initial and final stages of solidification, when the interface experiences qualitative changes in its topology. This problem can be overcome by using the correction factor for the interfacial area due to Avrami [57] to account for impingement of interfaces or the empirical relation proposed by Speich and Fisher [58].

4.2.2 Dendrite Envelope. The area concentration of the dendrite envelope is modeled by introducing an envelope shape factor defined as

$$\phi = A_{equivalent}/A_{actual} \tag{29}$$

By equivalent we mean an equivalent sphere or cylinder of the same volume as the actual crystal envelope. Equiaxed crystal envelopes are most appropriately described by equivalent spheres, while equivalent cylinders are chosen for the columnar case. The shape factors are schematically illustrated in Figs.12a and 12b. A shape factor always lies between zero and unity since a sphere and a cylinder have the least possible surface area for three-dimensional and axisymmetric bodies, respectively; however, for envelope shapes

similar to the ones shown in Fig.12, ϕ_e is relatively close to unity [59]. If the envelope is shape preserving during growth, ϕ_e can be taken as a constant.

A. Equiaxed Growth

For equiaxed growth, the diameter of the equivalent sphere, d_e, can be related to the number of crystals per unit volume, n, as

$$d_e = \left(\frac{6(1-\varepsilon_l)}{n\pi}\right)^{1/3} \tag{30}$$

Then, the following relation for S_e can be written:

$$S_e = \frac{1}{\phi_e}(36\pi)^{1/3}\, n^{1/3}\, (1-\varepsilon_l)^{2/3} \tag{31}$$

The number of equiaxed crystals per unit volume, n, must be calculated from a nucleation model, according to

$$\frac{\partial n}{\partial t} = \dot{n} \tag{32}$$

where $\dot{n}$ is the nucleation rate. In the present context of diffusion-controlled solidification, the source of equiaxed grains would be solely due to heterogeneous nucleation. The basic theory of heterogeneous nucleation has been outlined by Turnbull [60]. As reviewed in Rappaz [4]

$$\dot{n} = K_1(n_o - n)\exp\left[\frac{-K_2}{T\,(\Delta T)^2}\right] \tag{33}$$

where n_o is the initial nucleation site density, ΔT is the undercooling, K_1 is a constant related to the collision frequency of atoms of the melt with the nucleation sites of the heterogeneous particles, and K_2 is related to the interfacial energy balance between the nucleus, the liquid, and the foreign substrate on which nucleation occurs [4].

This nucleation theory has been shown to predict incorrect equiaxed grain sizes (see [4]) and more pragmatic approaches have been developed. Among them are the statistically based continuous nucleation theory due to Thevoz et al. [61] and the instantaneous nucleation concept due to Stefanescu et al. [62]. The latter can be simply written as

$$\dot{n} = n_o\, \delta(T - T_N) \tag{34}$$

where T_N is the critical nucleation temperature and δ is the Dirac delta function. The number of nucleation sites, n_o, must in turn be calculated from an empirical relation reflecting the influence of the cooling rate on the activity of the foreign substrates. All of the above approaches require the measurement of the grain density in a solidified melt sample for calibration. In other words, they are not truly predictive. Other complications arise in the presence of convection, which is discussed in more detail in Section 5.

B. Columnar Growth

By assuming a square pattern of the columnar dendrites on a transverse cross-section, as shown in Fig.12b, the equivalent diameter, d_e, can be related to the familiar primary arm spacing, λ_1 , such that

$$d_e = \left(\frac{4(1-\varepsilon_l)}{\pi}\right)^{1/2}\lambda_1 \tag{35}$$

For the equivalent cylinders assumed in columnar growth, the envelope area concentration becomes

$$S_e = \frac{1}{\phi_e}(4\pi)^{1/2}(1-\varepsilon_l)^{1/2}\frac{1}{\lambda_1} \tag{36}$$

It should be mentioned that Eqs.(35) and (36) are also valid for other arrangements of the dendrites, except for a slight change in the numerical factor.

The primary arm spacing, λ_1, depends mainly on V_t and G, the columnar front velocity and the temperature gradient. Hunt [63] developed a theory to predict the primary dendrite arm spacing:

$$\lambda_1 = \{64\Gamma D_l m_l(1-\kappa)C_o\}^{1/4} G^{-1/2} V_t^{-1/4} \tag{37}$$

Other theories result in essentially the same equation except for a different numerical constant [18].

By comparing Eq.(31) with Eq.(36), it is apparent that the number density of equiaxed crystals, n, can equivalently be viewed as the number density of primary arms in columnar

solidification, that is $n^{1/3} \sim 1/\lambda_1$. Furthermore, Eqs.(31) and (36) reveal the following important parametric relation:

$$S_e \sim n^{1/3} \text{ or } 1/\lambda_1 \tag{38}$$

The final equivalent radius ($R_f=d_e/2$) of a dendrite, which is useful in the calculation of the diffusion lengths, can be obtained from Eq.(30) or (35) by taking $\varepsilon_l=0$. Similar to the solid/liquid interface, the envelope area concentrations expressed by Eqs.(31) and (36) need to be modified during the initial and final stages of solidification. In particular, S_e should be equal to zero for $\varepsilon_l=0$.

4.3 Diffusion Lengths

The diffusion lengths characterize the magnitude of the diffusive flux between an interface and the adjacent phase. In view of Fig.10, they can be defined as

$$l_{kj} = \frac{\bar{C}_{kj} - \langle C_k \rangle^k}{-\left.\frac{\partial C_k}{\partial n}\right|_{kj}} \tag{39}$$

where the denominator represents the mean concentration gradient in phase k normal to the kj interface. The diffusion length is generally a complicated function of the micro-scale phenomena. Several simple analytical results are described below. Here, it is important to realize that analytical results are desirable so as to minimize the numerical effort. In the presence of convection, the diffusion lengths are closely related to the drag, and heat and mass transfer coefficients at the interfaces within V_o, which is discussed in more detail in Section 5.

4.3.1 Solid Region. The modeling of the diffusion length in the solid is important for the prediction of finite-rate solute diffusion and, hence, microsegregation in a solidified alloy. For dendritic solidification, Ohnaka [64] has presented an elegant model that gives good agreement with experimental data and fits well into the framework of the present

formulation. Following his procedure, the present derivation is based on a 1-D plate-like dendrite arm geometry, as shown in Fig.11. A parabolic concentration distribution is assumed in the solid phase. The centerline of the dendrite is taken to be a line of symmetry and the concentration at the solid/liquid interface is given by the phase diagram. Then, with the definition of the diffusion length, Eq.(39), it is readily shown that [39]

$$l_{sd} = d_s/6 \tag{40}$$

The mean diameter of the solid phase, d_s, can be related to the secondary dendrite arm spacing, λ_2, and the volume fraction ε_s [see Eq.(24)]. The derivation can be modified for other dendrite arm geometries such as cylinders and spheres. The same result is obtained except for a change in the numerical factor of the order of unity.

4.3.2 Interdendritic Liquid. For a dendrite envelope closely encompassing the dendrite arms, a similar analysis as that for the solid yields that the diffusion lengths in the interdendritic liquid, l_{ds} and l_{dl}, are proportional to the characteristic interdendritic spacing, i.e.,

$$l_{ds} \text{ and } l_{dl} \sim \lambda_2 \tag{41}$$

Together with Eq.(40), this implies that the diffusion lengths in the interdendritic liquid and the solid are of the same order of magnitude. However, because the liquid mass diffusivity is typically several orders of magnitude larger than that of the solid, it is usually safe to assume that the interdendritic liquid is solutally well-mixed and, thus, it is not necessary to accurately model finite-rate solute diffusion in the interdendritic liquid.

4.3.3 Extradendritic Liquid. In contrast, one has to carefully model the diffusion length in the liquid outside the dendrite envelope, in order to account for solutal undercooling of the liquid ahead of the dendrite tips. This can be done by assuming that (i) the envelope is spherical with an equivalent radius R_e and (ii) solute diffusion is one-

dimensional and quasi-steady in the moving coordinate system fixed to the envelope surface, as illustrated in Fig.13.

By solving the differential equation governing solute diffusion in the extradendritic liquid, it can be shown that the concentration profile is of an exponential nature [39]. Substitution of the profile into the definition of the diffusion length yields

$$l_{ld}/R_f = \frac{1}{Pe}\left(1 - \frac{3}{\varepsilon_l}\exp[-Pe(1-\varepsilon_l)^{1/3}]\int_{(1-\varepsilon_l)^{1/3}}^{1} x^2\exp[\frac{Pe(1-\varepsilon_l)^{2/3}}{x}]\,dx\right) \quad (42)$$

where x is a dummy variable of integration and the Peclet number, Pe, is based on the final equivalent radius, R_f, of the dendrite envelope

$$Pe = \frac{\bar{w}_{ne}R_f}{D_l} \quad (43)$$

A similar expression for the liquid diffusion length results for a cylindrical coordinate system, which is applicable to the columnar case [39].

It is worth noting that the diffusion length given by Eq.(42) has the property that

$$l_{ld} \leq \frac{D_l}{\bar{w}_{ne}} \quad (44)$$

The equality sign in Eq.(44) corresponds exactly to the analytical result of Rappaz and Thevoz [35]. More recent analyses of a similar nature have been presented by Nastac and Stefanescu [65].

4.4 Growth Kinetics of the Dendrite Envelope

As shown in Fig.9, the envelope is a smooth surface connecting both the primary and secondary dendrite arm tips. Therefore, the envelope velocity, $\bar{w}_{ne}$, can be taken to be equal to some mean tip velocity. Generally, each tip moves at a different speed depending on the local solutal undercooling in the extradendritic liquid adjacent to the tip. In particular, there may be considerable differences in the speeds of the primary and secondary dendrite arm tips. In spite of this complex situation, it may be assumed that the mean dendrite tip

velocity and, hence, the envelope velocity can be uniquely related to the average solutal undercooling in the extradendritic liquid, i.e., $\bar{C}_e - \langle C_l \rangle^I$. The irregular topography of the envelope caused by the different speeds of the dendrite tips is accounted for through the use of the envelope shape factor as described in Section 4.2.2.

Numerous studies have been performed to establish a relation between the dendrite tip undercooling and its growth velocity, and the detailed derivations can be found in [18]. Physically, the growth model is obtained by considering two phenomena: solute transport near the tip and tip stability. Assuming no back diffusion in the solid and using the common marginal stability condition for tip growth proposed by Lipton et al. [66], it can be shown that

$$\bar{w}_{ne} = \frac{D_l m(\kappa-1)\bar{C}_e}{\pi^2 \Gamma} Pe_t^2 \tag{45}$$

where the tip Peclet number, Pe_t, is related the dimensionless solutal undercooling, Ω:

$$\Omega = \frac{\bar{C}_e - \langle C_l \rangle^I}{\bar{C}_e(1-\kappa)} \tag{46}$$

via the solution of the solute diffusion problem near the tip. For diffusion-dominated growth, the exact solution, called the Ivantsov function, can be written as

$$Iv(Pe_t) = Pe_t \exp(Pe_t) E_1(Pe_t) = \Omega \tag{47}$$

where $E_1(Pe_t)$ is the exponential integral function. Combining Eqs.(45) and (47) yields a growth model for diffusion-dominated solidification.

The inclusion of a dendrite tip growth law has an important implication for the present multiphase model. The interface between the two liquid phases (i.e., the envelope) is no longer hypothetical but mathematically characterized by the growth law. Hence, it is as meaningful as the solid-liquid interface, which is mathematically represented by equilibrium conditions.

4.5 Limiting Cases and Comparisons

The previous subsections constitute the complete diffusional model for dendritic alloy solidification. An energy equation is used to calculate the temperature evolution and distribution and the solute diffusion equations can be integrated to obtain the solid fraction evolution, which then feeds back into the latent heat term. Because the solute diffusion model rests on numerous assumptions, it is necessary to first validate the predictions for certain limiting cases, which is the subject of this subsection. Details of the comparisons can be found in [40].

As reviewed by Rappaz [4], previous solute diffusion models for dendritic solidification can be classified as follows: (i) Equilibrium models which do not consider nucleation and undercooling in the liquid; (ii) Models for columnar growth which incorporate dendrite tip undercooling; (iii) Models for equiaxed growth focusing on coupling the growth kinetics of dendrite tips to the evolution of an equiaxed grain. The following subsections are divided according to this classification.

4.5.1 Complete Solute Mixing in the Liquid. This category of solute diffusion models essentially aims at investigating the effects of back diffusion in the solid. By neglecting dendrite tip undercooling, namely assuming complete solute mixing in the inter- and extradendritic liquid, the only solute diffusion equation of interest is the one for the solid, Eq.(40). Further restricting attention to a locally parabolic solidification rate, i.e.,

$$\varepsilon_s \frac{\partial \varepsilon_s}{\partial t} = \frac{1}{2t_f} \tag{48}$$

where t_f is the local solidification time, the present model admits a closed-form analytical solution [40]

$$\frac{\overline{C}_e}{C_o} = \frac{6\alpha(1 - \varepsilon_s)^{(1+6\alpha)\kappa-1}}{\varepsilon_s^{6\alpha}} \int_0^{\varepsilon_s} \varepsilon^{6\alpha-1}(1-\varepsilon)^{-(1+6\alpha)\kappa}\, d\varepsilon \tag{49}$$

where

$$\alpha = \frac{4D_s t_f}{\lambda_2^2} \tag{50}$$

is the traditional diffusion Fourier number based on the secondary arm spacing and C_o is the initial composition. For $\alpha \to \infty$ and $\alpha \to 0$, the well-known Lever rule and Scheil equation, respectively, can be recovered. For an intermediate α, Fig.14 compares Eq.(49) with other available microsegregation models. It can be seen that the present model agrees better with Kobayashi's exact solution [67] than the other analytical models due to Brody and Flemings [68], Clyne and Kurz [69], and Ohnaka [64]. Available in the literature are also a number of numerical models that can handle variable thermophysical properties and coarsening (see [70]).

4.5.2 Columnar Growth with Dendrite Tip Undercooling. At intermediate and high cooling rates, diffusion in the solid is found to be negligible. However, another effect begins to influence the relation between the solid fraction and temperature: the dendrite tip temperature falls significantly below the equilibrium liquidus temperature. Some recent theoretical studies of the tip undercooling effect have been reported by Flood and Hunt [36], Giovanola and Kurz [37] for an Ag-Cu alloy, and by Flemings [71] for an Al-Cu alloy. The latter two studies are based on the "patching" method due to Giovanola and Kurz [37]. This model divides the mushy zone into two regions, with nonequilibrium growth allowed only in the tip region and a state of complete solute mixing in the liquid assumed in the other region. Then, a curve-fitted polynomial and the Scheil equation are utilized for the solid fraction profiles in the two regions, respectively. The KGT model [72] is used for the dendrite tip growth and back diffusion in the solid is neglected. Without presenting the details of the calculations [40], the present model is compared in the following to these and other studies of columnar solidification. The interdendritic liquid is assumed to be solutally well mixed.

To examine the sole effect of dendrite tip undercooling, calculations have been carried out for two cooling rates of $\dot{T} = 10^3$ and 10^6 K/s and by setting $D_S=0$ in the model equations. The predicted temperature *vs.* solid fraction curves are plotted in Fig.15 together with Flemings' results. It can be seen that the two predictions basically produce the same trend. The temperature undergoes little change during the initial long stage of solidification, and significantly decreases only during the last short period of solidification. The other consequence of dendrite tip undercooling is a decrease in the fraction eutectic. It should be realized that, opposed to the patching method of Giovanola and Kurz [37], a single set of equations is used in the present model throughout the entire mushy region.

Another numerical study using the present model is conducted for an Ag-15wt% Cu alloy, again assuming negligible back diffusion in the solid. Calculations have been carried out using the data from the experiment of Bendersky and Boettinger [73]. The predicted microsegregation profile is plotted in Fig.16, together with Giovanola and Kurz's result [37] as well as the experimental data measured by Bendersky and Boettinger [73]. It can be seen that all three results are in good agreement, thus validating the present model in accounting for the influence of dendrite tip undercooling. Slight differences between the present results and those from the Giovanola and Kurz model can be observed in both Figs.15 and 16. They can be attributed to the simplified treatment of the dendrite morphology in Giovanola and Kurz' patching method [37]. In fact, it can be argued that the present predictions in Fig.16 are in somewhat better agreement with the experimental data.

In order to predict microsegregation over a wide range of cooling rates, however, the effects of back diffusion in the solid and dendrite tip undercooling need to be taken into account simultaneously. Recently, Sarreal and Abbaschian [74] presented a set of experimental data for an Al-4.9wt% Cu alloy in order to demonstrate the influence of the cooling rate on microsegregation. Interestingly, they found that the eutectic fraction first increases as the cooling rate rises up to 187 K/s and then decreases with increasing cooling rate. This behavior cannot be captured by a solute diffusion model that considers either

solid diffusion only or dendrite tip undercooling alone, as indicated in Battle and Pehlke [75]. Since the present model includes both of the above mentioned factors, it can be expected to be an appropriate theoretical tool for explaining the experimental observation. Several numerical simulations have been performed for solidification of an Al-4.9wt% Cu alloy at the cooling rates and growth velocities present in the experiments. In the calculations, eutectic undercooling was neglected and constant alloy properties were assumed. Figure 17 compares the predictions with the experimental results of Sarreal and Abbaschian [74] for the eutectic fraction as a function of the cooling rate. In the figure, ϵ_{Emax} is the theoretical maximum eutectic fraction as computed from the Scheil equation. It is found that the agreement between the model predictions and the experimental results is fairly good, with the relative error ranging from 1.73% to 11.5%. By including eutectic undercooling and variable alloy properties, Roosz and Exner [76] and Voller and Sundarraj [77] obtained even better agreement. Nonetheless, the important fact that the eutectic fraction is reduced at a very high cooling rate is predicted by the present model. This is known to be due to the effect of dendrite tip undercooling on microsegregation. At low cooling rates, back diffusion in the solid causes a reduction in the eutectic fraction, while at high rates, dendrite tip undercooling tends to decrease the eutectic fraction. However, the two effects are not additive. At low cooling rates, the effect of dendrite tip undercooling does not exist, while at very high cooling rates, diffusion in the solid phase becomes negligible due to the short duration of the solidification process.

4.5.3 Equiaxed Growth. The solute diffusion processes occurring in equiaxed dendritic growth are even more difficult to model, mainly because an equiaxed dendrite is not fully solid. Several approaches have been reported in the literature. Dustin and Kurz [33] presumed that a mushy grain has a constant internal solid fraction. As already mentioned, Rappaz and Thevoz [34,35] were the first to fully account for nucleation and growth kinetics, and introduced the idea of a spherical grain envelope which separates the

inter- from the extra-dendritic liquids. The interdendritic liquid was assumed to be solutally well mixed, and the dynamics of the envelope were determined by the growth kinetics of the dendrite tips. Both numerical and analytical versions of this solute diffusion model were formulated.

In order to validate the present model for equiaxed dendritic growth, solidification of an Al-5wt% Si alloy has been simulated and compared with the results of Rappaz and Thevoz [34]. Again, the interdendritic liquid is assumed to be solutally well mixed. The simulations correspond to isothermal solidification of a small sample, where the following energy equation applies:

$$q_{ext}\frac{A}{V_o} = \rho c\dot{T} = \rho\Delta h\frac{d\varepsilon_s}{dt} + \rho c\frac{dT}{dt} \tag{51}$$

A series of predicted cooling curves for a cooling rate of 45 K/s and three different final grain radii is compared against the more exact solution of Rappaz and Thevoz [34], as shown in Fig.18. The latter was obtained by solving a microscopic partial differential equation for solute diffusion in the extradendritic liquid by a finite difference technique. It can be seen that excellent agreement between the two predictions exists, although the present model utilizes the simpler concept of a diffusion length together with an integral formulation. The predicted recalescence is typical of equiaxed solidification. The increase in the temperature at later times is due to the latent heat release being larger than the external cooling. Rappaz and Thevoz [34] and Thevoz et al. [61] also compare their predictions to a variety of experiments, including multidimensional castings, and the reader is referred to the original literature for a more detailed discussion.

4.6 Application to the Prediction of the Columnar-to-Equiaxed Transition (CET)

Only recently, efforts have been made to theoretically model the CET. Hunt [78] first developed an analytical model by considering steady state columnar and equiaxed growth.

The model qualitatively reveals the influences of alloy composition, nuclei density and cooling rate on the CET. Subsequently, Flood and Hunt [36] extended the work to dynamically model the CET in a one-dimensional ingot. They incorporated grain nucleation and growth principles into a heat flow calculation, and simulated the CET as a Stefan-like discontinuity interface. Although their work significantly advances the prediction of the CET, it suffers from several limitations. First, solute is not conserved in their model, as noticed in a number of subsequent investigations [4,37]. This leads to erroneous predictions of the volume fraction of equiaxed grains whose growth is mainly controlled by constitutional undercooling, and therefore makes it impossible to capture the CET accurately. Secondly, their model is a multi-domain formulation in which different governing equations are applied to the columnar and equiaxed zones. The solution of such equations requires explicit tracking of the interface separating the two zones and the use of appropriate matching conditions between the two regions. It is well known that great difficulties are associated with the numerical implementation of such a model, in particular in multi-dimensional situations.

Other numerical studies of predicting the grain growth and CET adopt a completely different approach, namely a probabilistic method based on the Monte-Carlo procedure. Notable work includes that by Brown and Spittle [79], Zhu and Smith [80], and Rappaz and Gandin [81]. Capable of producing computed two-dimensional microstructures which closely resemble those observed in real micrographic cross-sections, these models, however, either lack a rigorous physical basis or invoke certain simplifications. For example, the physical mechanisms of nucleation and growth of dendritic grains have not been properly accounted for in the statistical models by Brown and Spittle [79] and Zhu and Smith [80]. A uniform temperature field has been assumed and solute diffusion not considered by Rappaz and Gandin [81].

Comprehensive experiments on the CET have been conducted by Weinberg and coworkers in laboratory ingots cooled from below for various Sn-Pb alloys [82] and an Al-

3wt% Cu alloy [25]. The relationship between the casting parameters and the CET position has been established for these alloys. However, no systematic comparisons between these experiments and theory have been attempted so far [83].

In this section, selected results of a recent study by Wang and Beckermann [24] are presented. All results shown are directly based on the multiphase/scale model of Sections 4.1 to 4.4. All thermophysical property data and other conditions can be found in the original reference.

4.6.1 System Description. The system investigated is shown in Fig.19 and consists, in the most simple case, of a one-dimensional casting in which mixed columnar and equiaxed growth occurs. The equiaxed grains compete with the advancing columnar grains; when the equiaxed crystals are small, they are swallowed by the approaching columnar front and transformed into columnar dendrites. Conversely, if the undercooled zone ahead of the columnar front is relatively large and the density of crystals high, the equiaxed grains may have enough time to reach a sufficiently high volume fraction to block the columnar crystal growth. The latter case results in the CET in the final microstructure of a solidified material. A criterion for the CET to occur was first proposed by Hunt [78] and later confirmed by Brown and Spittle [79]. That is, the equiaxed grain volume fraction ($\varepsilon_s+\varepsilon_d$) immediately ahead of the columnar front must exceed 0.49 to stop the columnar growth.

The boundary and initial conditions for the energy equation, Eq.(10), and the solute diffusion model, Eqs.(19-22), can be summarized as follows:

$$-k\frac{\partial T}{\partial x} = h(T - T_a) \text{ (at the lower wall)}; \quad \frac{\partial T}{\partial x} = 0 \text{ (at the upper wall)} \tag{52}$$

and

$$\text{at } t = 0, \quad T = T_o, \ \overline{C}_e = \langle C_l \rangle^l = C_o, \ \langle C_s \rangle^s = \kappa C_o, \ \varepsilon_s = \varepsilon_{so}, \ \varepsilon_d = 0, \ \varepsilon_l = 1-\varepsilon_{so} \tag{53}$$

where h is the heat transfer coefficient at the chill wall. The initial temperature, T_o, is not necessarily equal to the liquidus temperature corresponding to the initial concentration,

$T_L(C_o)$, and their difference, $\Delta T_o = T_o - T_L(C_o)$, represents the pouring superheat. The initial solid fraction ε_{so} is a small positive number to account for the finite size of the nuclei present in the liquid melt. In the numerical simulations presented below, ε_{so} was chosen to be small enough that the later predictions are insensitive to ε_{so}.

As in the comparisons presented in Section 4.5, the interdendritic liquid is assumed to be solutally well mixed, resulting in certain simplifications in the model equations [24]. Back diffusion in the solid is also neglected (i.e., D_S=0).

4.6.2 Numerical Results. Because all the macroscopic diffusion equations are equally valid for columnar and equiaxed growth, a fixed grid can be utilized and no internal matching conditions between the various regions need to be considered. Other numerical procedures include a two-time-step scheme, inspired by Thevoz et al. [61], and a special columnar front tracking algorithm [24].

A representative one-dimensional simulation was first carried out for an Al-3wt% Cu alloy in a one-dimensional mold of 100mm length, and the results are presented in Figs.20 and 21. The conditions are: h=65 W/m^{2}K, n=10^5 m^{-3} and ΔT_o = 20 K.

Figure 20a shows the calculated cooling curves at five locations between x/L=0.025 and 0.825 with an interval of 0.2. Negligible bouncing or reheating effects are seen in the cooling curves near the recalescence stage (see the inset of Fig.20a), although a relatively coarse grid was used. Significant recalescence is only observed in the first curve for the location nearest to the chill wall, whereas the other curves exhibit thermal plateaus. It can be concluded that for the mixed mode of solidification, recalescence is less pronounced than in purely equiaxed solidification [61]. This is because the cooling curve for mixed growth embodies features of columnar solidification, namely a temperature plateau in the cooling curve [36]. The fact that the cooling curves for various modes of solidification are distinctive in shape has been utilized by Lipton et al. [84] for *in situ* measurements of the CET positions in castings.

The computed solid and grain fractions are displayed in Fig.20b at the same locations as the cooling curves. Again, the grain fraction is defined as the sum of the solid and interdendritic liquid volume fractions. This figure clearly shows that the two quantities do evolve at disparate rates, as mentioned earlier. Hence, a two-time step scheme is necessary for accurate calculations of both macro- and microscopic features of solidification. In addition, it is noticed from Fig.20b that the grain fraction at some locations does not reach the maximum value of unity. This is because complete mixing of solute in the extradendritic region is reached before the grain envelopes impinge. In other words, the dendrite tips do not advance further, because undercooling at the tips is no longer significant. The remaining liquid in the extradendritic region is ultimately solidified during the eutectic reaction.

The evolution of the different regions in the ingot is depicted in Fig.21, where the dashed line denotes the liquidus isotherm corresponding to the initial alloy concentration, and the solid line stands for the CET interface which divides the mushy zone into the columnar and equiaxed regions. The final CET position corresponds to the vertical part of the solid line. Hence, the CET occurs about 650 seconds after the initiation of cooling of the ingot.

Selected two-dimensional simulations were also performed for the Al-3wt% Cu alloy. Figures 22a and 22b depict the evolution of the interface between the columnar and equiaxed zones in 100×100mm square and 50×100mm rectangular castings, respectively. The left and bottom walls were cooled with a heat transfer coefficient of 65 W/m^2K, while the upper and right boundaries were insulated to represent symmetry conditions. Other conditions are the same as in the one-dimensional simulation. The predicted CET interfaces are quite similar to the ones observed in the experiments of Brown and Spittle [85] for the square geometry, and to the simulation results obtained by Zhu and Smith [80] for the rectangular geometry.

4.6.3 Experimental Verification. This section presents some validation of the present model using the experimental data of Weinberg and coworkers for both Sn-Pb [82] and Al-Cu [25] alloys. In Weinberg's experiments, the various alloys were poured into a 100mm long cylindrical mold and solidified vertically upward from a water-cooled copper chill at the bottom. One-dimensional solidification results by avoiding lateral heat losses. The CET position was observed and measured by sectioning the solidified ingots along the vertical center plane, and polishing and etching the sectioned surface. Since for both alloys the solute-rich interdendritic liquid has a higher density than the overlying alloy melt and the axial temperature gradients are stable, melt convection due to buoyancy forces is minimal and, thus, the CET data are well suited for comparison with the present model where convection is omitted. Some uncertainties remain, however, with respect to the effects of sedimentation or floating of equiaxed grains due to the density difference between the solid and liquid phases. The experiments covered a wide range of chill heat transfer coefficients, pouring superheats, and alloy compositions.

In the absence of a reliable nucleation model, a parametric study was first performed to investigate the effect of the equiaxed nuclei density on the CET. Figure 23 compares the model predictions to the Al-3wt% Cu alloy data of Ziv and Weinberg [25]. It can be seen that for all chill heat transfer coefficients the predicted CET positions agree fairly well with the experimental data for a nuclei density in the equiaxed zone of 10^5 m^{-3}. This value was thus used in all comparisons with the Al-3wt% Cu experiments. A similar procedure for the Pb-Sn alloy experiments of Mahapatra and Weinberg [82] showed that a single nuclei density of 10^7 m^{-3} resulted in good overall agreement with all 24 experimental runs. The value of $n=10^7$ m^{-3} (which corresponds to a final equiaxed grain size of about 2.8 mm) is of a reasonable magnitude, although some variations can be expected for the different cases. A summary of all comparisons is presented in Fig.24.

Returning to Figure 23, one can also examine the effect of inoculation on the CET. In the inoculation experiments with $h=50$ W/m^2K [25], it was found that the equiaxed grain

size decreased from 5.4 to 1 mm by adding 172ppm of TiB_2 to the liquid melt. The 1mm grain size corresponds to an equiaxed nuclei density of about 1.9×10^9 m^{-3}. Figure 23 shows that, at this value of the nuclei density and h=50 W/m^2K, a wholly equiaxed structure is predicted, which agrees with the experimental observations [25]. In fact, Figure 23 indicates that the transition to a wholly equiaxed structure takes place at a nuclei density of roughly 10^8 m^{-3}.

The above comparisons show that, given a realistic nucleation model, quantitative agreement between measured and calculated CET positions can be obtained. More well-controlled experiments are needed to fully validate the model. Furthermore, melt convection and crystal multiplication/transport remain to be included for situations where diffusion is not dominant.

5. CONVECTIVE TRANSPORT IN DENDRITIC ALLOY SOLIDIFICATION

While the prediction of diffusion-dominated alloy solidification has reached a considerable level of sophistication in recent years, the inclusion of melt convection and the transport of solid phases in the form of dendrite fragments and small equiaxed crystals, has only begun to receive serious research attention. The major challenge lying ahead is the quantitative modeling of the interactions between the flow and the dendritic microstructure, leading to the kind of micro/macroscopic predictions discussed in Section 4 for diffusional transport. Instead of providing a complete account of all studies in this area, the following subsections focus on several selected issues that are the subject of intensive present research efforts, but are largely unresolved. The discussion is conveniently divided into two sections corresponding to columnar solidification with a rigid and stationary solid phase and equiaxed solidification with melt convection and solid transport. A third subsection briefly discusses important issues in coupled columnar/equiaxed solidification with convection. In the following, all volume averaging symbols are omitted, and $\langle \Psi_k \rangle^k$ is simply denoted by Ψ_k. The overbar is retained to designate interfacial quantities.

5.1 Columnar Solidification with Stationary Solid

Models of columnar solidification with melt convection and a rigid, stationary solid phase typically neglect dendrite tip undercooling and calculate microstructural parameters, such as the dendrite arm spacings "after-the-fact" rather than as an integral part of the model. While numerical solutions of the model equations that describe columnar solidification have illustrated the capabilities of such models to predict the development of an irregular liquidus front, local remelting of solid, the development of flow channels in the mushy zone and the establishment of macrosegregation patterns for the solidification of salt-water solutions [86-88] as well as metal alloys [89-92], few studies have addressed the

effects of microscopic behaviors on the macroscopic transport phenomena. There are two important areas where what occurs on a microscopic level influences macroscopic transport in columnar solidification: the influence of the morphology of the mushy zone on the resistance it offers to flow, as characterized by the mushy zone permeability, and the effects of microsegregation on macrosegregation. In addition, most attempts at modeling convection during columnar solidification have considered only flow driven by the action of gravity on density gradients caused by temperature and concentration variations in the melt, i.e., thermosolutal buoyancy. Since the density of the solid and liquid phases is usually quite different, however, the volume change that occurs upon solidification (i.e., solidification shrinkage) also causes fluid motion, and can lead to macrosegregation. While there are other topics of concern in modeling columnar solidification, these issues have been the subject of recent research efforts and are discussed in more detail in following subsections.

5.1.1 Reduced Macroscopic Equations. Before discussing the roles of microscopic behaviors and solidification shrinkage in macroscopic model predictions, some background on the assumptions used in deriving the model equations and the physical interpretation of those equations is necessary. In this subsection, a macroscopic model [93] is described that is, in essence, a generalization of models used by Bennon and Incropera [86], Beckermann and Viskanta [87], Voller et al. [88], and others to predict convection and macrosegregation during the columnar solidification of binary alloys. The model accounts for the presence of at most three phases: liquid (subscript l), alpha-phase solid (subscript α) and gamma-phase solid (subscript γ). The macroscopic conservation equations in the model can be directly obtained from the volume-averaged equations of Table 1, and are summarized in Table 2.

The assumptions made to obtain the equations listed in Table 2 include:

(1) The solid phases are attached to the mold wall and are rigid so that

$$\mathbf{v}_\alpha = \mathbf{v}_\gamma = 0 \tag{54}$$

The model is also restricted to creeping flow in the mushy zone and laminar flow in the bulk liquid regions so that all dispersion fluxes may be neglected.

(2) All of the phases within an averaging volume are in thermal equilibrium, i.e.,

$$T_\alpha = T_\gamma = T_l = T \tag{55}$$

The justification for this assumption is the same as in Section 4.1, and this enables the use of the mixture energy equation in Table 2.

(3) As in Section 4.5.1, the liquid within an averaging volume is considered to be solutally well mixed so that the interfacial average and volume average concentrations are equal, i.e.,

$$C_l = \overline{C}_{ls} \tag{56}$$

Due to solutal undercooling, this approximation may introduce some error at the dendrite tips, but is reasonable in the porous dendritic mush. This assumption also makes it unnecessary to distinguish between inter- and extra-dendritic liquid.

(4) Microscopic species diffusion in the solid phases is assumed to take one of two limiting cases: complete diffusion, where the interfacial average and volume average concentrations are equal, i.e.,

$$\overline{C}_{sl} = C_s \qquad s = \alpha, \gamma \tag{57}$$

or no diffusion, where there is a microscopic solute profile in the solid, i.e.,

$$\overline{C}_{sl} \neq C_s \qquad s = \alpha, \gamma \tag{58}$$

This covers two important limiting cases of solid microsegregation, and will be discussed in more detail in Section 5.1.2.

(5) While all macroscopic solid species fluxes are assumed to be negligible, in order to predict double-diffusive phenomena in the melt finite-rate macroscopic liquid species diffusion is included. Only ordinary (Fickian) diffusion is considered.

(6) Thermodynamic equilibrium is assumed to exist at the solid-liquid interfaces so that the interfacial temperature and concentrations can be related through the phase diagram.

(7) The phase enthalpies are assumed to vary with both temperature and concentration. Also, all macroscopic species diffusion terms appearing in the mixture energy equation are neglected.

(8) Gravity is assumed to be the only body force, and the viscous stresses are assumed to be proportional to the rates of deformation.

(9) The flow through the porous matrix of columnar dendrites in the mushy zone is typically very slow so that the dissipative interfacial stress can be modeled using the mushy zone permeability, $\mathbf{K}^{(2)}$, in analogy with Darcy's law. More details regarding the mushy zone permeability are given in Section 5.1.3.

(10) The phase diffusion coefficients that appear in the conservation equations are not effective values that are functions of the local microstructure, but are set equal to their microscopic counterparts.

The assumptions given by equations (2) through (5) are also illustrated in Fig.25.

5.1.2 Microsegregation in the Solid. The first way that microscopic behavior can affect macroscopic transport is through the influence of solid microsegregation. Since melt flow can redistribute species segregated on a microscopic scale, accurate modeling of microsegregation should, in principle, be even more important in the presence of convection than for purely diffusional transport. Since microsegregation introduces solutal gradients into the melt and influences the solid fraction evolution in the mushy zone, it can also affect the fluid flow.

As discussed in Section 4.5.1, the term $(S_S\rho_S D_S/l_{sl})(\overline{C}_{sl} - C_S)$ in the solid species conservation equations in Table 2 physically represents the transfer of species at the solid/liquid interface in an averaging volume due to microscopic species concentration gradients within the solid. Since the quantity $\sqrt{(l_S/S_S)}$ can be considered a characteristic length for the local solid microstructure, and if t_f denotes the local solidification time, the

quantity $(S_S D_S / l_{sl}) t_f$ is a dimensionless diffusion time (Fourier number). Note that for a simple plate-like dendrite geometry and parabolic solidification rate this quantity reduces to α in Eq.(50). Then, two limiting cases of microscopic solid species diffusion can be considered [18]:

$$\frac{S_S D_S}{l_{sl}} t_f >> 1 \tag{59}$$

or

$$\frac{S_S D_S}{l_{sl}} t_f << 1 \tag{60}$$

Equation (59) implies that the time required for species diffusion in the solid on a microscopic scale is short in comparison with the local solidification time. Then, examination of the solid species conservation equations in Table 2 reveals that the volume average solid concentrations will be equal to the average interfacial solid concentrations, i.e., the solid phases will be solutally well mixed and Eq.(57) will be satisfied. Conversely, Eq.(60) means that the time required for microscopic species diffusion in the solid is much longer than the local solidification time, and the solid species conservation equations show that there will be a microscopic concentration profile within the solid in an averaging volume as noted by Eq.(58). In other words, the solid will have "layers" of different compositions, with the concentration of each layer uniquely related to the concentration of the liquid from which it formed. In the absence of macroscopic advection and diffusion of solute, these two cases reduce to the lever rule and Scheil model [3,94] that have been used by metallurgists for many years.

In the majority of numerical simulations of columnar solidification, either Eq.(57) or (58) is chosen as the model for microsegregation. Only two studies have directly compared macrosegregation patterns for these two limiting cases. By simulating the solidification of an NH_4Cl-H_2O mixture, Voller et al. [88] determined that the general behavior for the two cases was qualitatively similar, with the predicted macrosegregation for the case of no solute diffusion slightly worse than that for complete solute diffusion. Schneider and

Beckermann [93] simulated the solidification of a Pb-20 wt% Sn alloy using the domain and boundary conditions shown in Figure 25. The final macrosegregation patterns for the two limiting cases of microsegregation again produced very similar macrosegregation patterns, as shown in Figures 26a and 26b. In contrast with Voller et al. [88] the assumption of complete diffusion led to slightly more severe macrosegregation. For the diffusion-dominated solidification of a Pb-Sn alloy, the movement of the liquidus isotherm for the two cases was also shown to differ only slightly [93,96]. However, those results also indicate that the volume fraction of eutectic in the final solid can be quite different for the two cases [96]. The results of Schneider and Beckermann [93], as illustrated by the final eutectic fraction distributions in Figs.26c and 26d, indicate similar behavior when melt convection is considered. Figure 26c shows that when no solid species diffusion is assumed a large portion of eutectic is formed throughout the casting, with more eutectic in regions that are more severely segregated. Fig.26d shows that when complete solid species diffusion is assumed, a large portion of the casting contains little or no eutectic. These results indicate that it may not be necessary to use more complicated microsegregation models (e.g., including finite rate solute diffusion in the solid microscopically or more carefully incorporating coarsening effects) if one is solely interested in predicting macrosegregation. However, such complicated microsegregation models are probably necessary to accurately predict eutectic formation.

Another issue closely related to microsegregation is how to model the local remelting of some of the solid that has formed. Since the solid is assumed to be solutally well mixed on a microscopic scale when using Eq.(57), this presents no difficulty. When using Eq.(58), however, the presence of a microscopic concentration profile in the solid creates problems during remelting [94,96]. In this case, the manner in which the average solid concentration varies during remelting depends on the concentration of the solid that is melting. Clearly, careful experimentation is necessary to obtain accurate and realistic models of remelting.

5.1.3 Mushy Zone Permeability. The permeability of columnar dendritic mushy zones has been measured in several studies (Poirier [97] and Liu et al. [98] provide summaries), and can be correlated as a function of the solid volume fraction as well as the primary and/or secondary dendrite arm spacings. The anisotropic structure of the columnar dendrites also causes the permeability along the primary dendrite arms and perpendicular to the primary arms to be unequal [97]. Unfortunately, experimental measurement of the permeability is only practical for a limited range of liquid fractions (from 0.15 to 0.65). A promising solution to this problem has been presented by Ganesan et al. [99], where descriptions of real microstructures taken from quenched solidification experiments were combined with numerical simulations of the microscopic flow along primary dendrite arms for liquid fractions above 0.65. The results showed that the permeability could be described well by analytical solutions for the flow through arrays of cylinders. Further complications arise when the velocities in the mushy zone become high, and the assumption of creeping flow breaks down. Two models have been proposed where higher order friction terms are used to account for this effect [87,32], although at the present time there is not sufficient experimental evidence to justify the inclusion of such terms in modeling the flow through mushy zones.

The use of advanced permeability models in columnar solidification simulations has been relatively limited. Neglecting the anisotropy of the mushy zone was shown to have an effect on the convective flow during the solidification of an NH_4Cl-H_2O solution [100,101]. This, in turn, led to significant differences in the prediction of the growth of double diffusive layers, remelting of solid and macrosegregation [101]. Felicelli et al. [90] used correlations for measured perpendicular and parallel permeabilities at low liquid fractions and analytical permeability relations for the flow through arrays of cylinders at high liquid fractions, but did not examine the effects of using these permeability relations.

To determine the influence of permeability relations on the flow and macrosegregation during solidification simulations, Schneider and Beckermann [93] examined the use of two

different permeability models. In the first case anisotropic permeability relations like those of Felicelli et al. [90] were used, while in the second case an isotropic permeability relation, based on the Blake-Kozeny model and used extensively in solidification simulations, was utilized. In the anisotropic case, the dendrites were assumed to grow in a direction opposite the flow of heat. Figure 27 shows that the anisotropic permeabilities jump by nearly a factor of 100 at the transition point between the experimental and analytical permeability expressions. The figure also shows that the permeability parallel to the primary arms is always larger than that perpendicular to the arms, although the difference is a factor of around 2 over a large range of liquid fractions. The largest difference between the isotropic and anisotropic permeabilities is at high liquid fractions. Since the initiation of the formation of channels in the mushy zone occurs in regions where the liquid fraction is high, these difference are significant. The large difference between the permeability parallel to the primary arms and the isotropic permeability at low liquid fractions is not of critical importance, since the flow velocities in regions of low liquid fractions are comparatively small. To illustrate the differences in the macroscopic model predictions when using these different permeability relations, Fig.28 shows predicted velocity and macrosegregation distributions after 250 seconds for the solidification of a Pb-20 wt% Sn alloy with the domain and boundary conditions given in Fig.25. Figure 28a shows that due to the jump between the experimental and analytical anisotropic permeabilities, flow in regions characterized by a liquid fraction of greater than 0.7 is much stronger than in regions of smaller liquid fractions. Obviously, such a jump is not physically realistic and illustrates the need for continued work to develop permeability relations valid for all liquid fractions.

Examining Fig.28, the most noticeable difference in the solid fraction and macrosegregation distributions predicted using the two permeability models is in the number, length and orientation of the channels formed in the mushy zone. These channels are preferred flow paths for the solutal buoyancy driven interdendritic flow. The presence of tin-rich interdendritic liquid in the channels serves to lower the liquidus temperature,

resulting in both local remelting and the delayed formation of solid. Many short channels are predicted with the isotropic permeability model because at very high liquid fractions (i.e., at the edge of the mushy zone) the resistance to flow is small (in comparison with the anisotropic case) due to the high permeability. Therefore, it is easy for flow channels to begin to form. As the liquid fraction decreases slightly, the permeability decreases rapidly, it becomes more difficult for flow to "feed" the channel, and its development is slowed or stopped. Figure 28b confirms this behavior since near the edge of the mushy zone there appears to be flow into and out of the mushy zone via the many channels while in areas of lower liquid fraction the flow is comparatively slow and mostly upward. In the anisotropic case, the relatively high permeability over a range of liquid fractions provides less resistance to the upward, solutally driven flow in the mushy zone. Figure 28a shows that this has resulted in long, vertically oriented channels.

Since the uncertainty in experimentally measured permeabilities is large, and especially since no experimental measurements have been made for high liquid fractions, these results show a definite need for further investigation into the permeability of mushy zones. Furthermore, the results suggest information on the mushy zone permeability could be backed out from solidification experiments. For instance, one could measure the length and orientation of the channels in a solidified sample, and then use model predictions to determine what type of permeability (e.g., degree of anisotropy, relative magnitude, etc.) is necessary to reproduce similar channels. Another important issue that has remained nearly unexplored is the three-dimensional nature of the channels [92]. It is unclear whether two-dimensional simulations can accurately describe such an inherently three-dimensional process.

5.1.4 Shrinkage Driven Flow. The densities of the solid and liquid phases of an alloy will be unequal as well as functions of both temperature and concentration. Hence, bulk liquid motion in the melt is necessary to account for the volume contraction, or

shrinkage, that accompanies solid/liquid phase change. Typically, the density of the solid phase is larger than that of the liquid and it becomes necessary to "feed" the volume shrinkage. In the foundry, this is accomplished by attaching risers to the casting, much like the upper-right portion of the domain shown in Fig.25. Since this shrinkage flow is towards the cooled boundaries, it redistributes any rejected solute in the mushy zone and forms a positively segregated region near these boundaries, termed inverse segregation.

Including contraction driven flow, in addition to buoyancy driven flow, in single-domain alloy solidification simulations has also received attention recently. Chiang and Tsai [102,103] investigated flow patterns caused by shrinkage driven flow, as well as the interaction of buoyancy and shrinkage driven flow during the solidification of a 1% Cr-steel. However, species conservation was not considered and the solid volume fraction in the mushy zone was assumed to vary linearly with temperature. Tsai and co-workers [104-107] obtained good agreement between predicted and measured inverse segregation profiles for unidirectionally solidified aluminum-copper alloys. Since those studies focused on the upward solidification of an Al-4.1 wt% Cu alloy, where the heavier copper is rejected in the mushy zone, stable thermal and solutal gradients reduced thermosolutal buoyancy driven flow so that the segregation was primarily due to contraction driven flow. Therefore, the combined effects of natural convection and contraction flow on macrosegregation were not investigated. Xu and Li [108,109] solved the complete set of conservation equations with both buoyancy and contraction driven flow for the solidification of an Al-Cu alloy. The computational grid used in the simulations, however, was too coarse to capture double-diffusive flows and local remelting of solid. While no effort was made to examine the effects of the combined flow on the final macrosegregation patterns, good agreement with experimental results was obtained [110].

The model equations summarized in Table 2 are also applicable when the solid and liquid densities are unequal. Schneider and Beckermann [93] have included shrinkage driven flow, in addition to buoyancy driven flow, in their simulation of the solidification of

a Pb-20 wt% Sn alloy. The results showed that shrinkage driven flow was most important during the latter stages of solidification when buoyancy driven flow has been damped out. Figure 29 shows the shrinkage dominated velocity fields near the end of solidification for the two limiting cases of microsegregation discussed in Section 5.1.2. This figure also illustrates the coupling of the prediction of shrinkage driven flow with the choice of microsegregation model. Close comparison of Figures 29a and 29b shows that the magnitude of the flow (especially in the riser) is slightly larger in Fig.29b, where complete diffusion in the solid is assumed. This is due to the fact that in this case mostly primary-phase solid is forming while in the case where no solid diffusion is assumed eutectic is forming. Since the eutectic density is considerably less than that of the primary-phase solid, more flow is needed to feed the solidification shrinkage.

Schneider and Beckermann [93] also observed an interesting interplay between shrinkage driven flow and macroscopic species diffusion in the liquid phase. Figure 30 shows inverse segregation profiles for the unidirectional solidification of a Pb-20 wt% Sn alloy with no buoyancy driven flow. Previous investigations of contraction driven flow and macrosegregation have shown only positive (inverse) segregation near the cooled boundary [104-107]. Figure 30b also shows this inverse segregation, except when the solid and liquid densities are equal (i.e., no flow) where there is a nearly uniform mixture concentration across most of the casting. Figure 30a, however, shows that when species diffusion in the liquid is considered, there is a small negatively segregated region very near the chill that is not present when species diffusion in the liquid is neglected. The cause of this behavior is diffusion of species away from the wall due to the concentration gradient in the liquid formed by the rejection of tin into the liquid during solidification.

5.2 Equiaxed Solidification with Melt Convection and Solid Transport

A relative new topic is the modeling of combined liquid and solid convection in alloy solidification, as may be present in equiaxed growth. Several studies have addressed this

problem by using averaged mixture equations and neglecting undercooling and grain growth kinetics. Because only a single (mixture) momentum equation is solved, some *a priori* assumption must be made about the relationship between the liquid and solid velocities. Voller et al. [88] investigated the limiting case where the solid and liquid velocities are equal, which is valid for a highly dispersed solid phase. The viscosity of the mixture was enhanced with increasing solid fraction to simulate the formation of a coherent and rigid solid structure. When compared to a fully columnar structure, a more uniform macrosegregation pattern was predicted. A hybrid model was developed by Oldenburg and Spera [111], where for a solid fraction below 0.5, the equal phase velocity/enhanced viscosity concept was utilized, while for ε_s above 0.5 a zero solid velocity model was used. The transition was accomplished through the use of certain switching functions. Flood et al. [112] and Voller [113], on the other hand, introduced the concept of a consolidation factor that specifies the relationship between the liquid and solid velocities. This factor is a simple linear function of the solid fraction and varies from unity for $\varepsilon_s \rightarrow 0$ (equal phase velocities) to zero at some given value of ε_s corresponding to a stationary solid. Prescott et al. [114] switched from a zero solid velocity model with melt flow to an equal phase velocity model (with the viscosity equal to that of the liquid) for solid fractions below 0.01. In order to model recalescence, they introduced a solid fraction model that accounts for undercooling by specifying a certain decay rate of the undercooling from a maximum value. The undercooling model was calibrated using experimental data and produced fair agreement with temperature measurements for solidification of a Pb-Sn alloy. In general, the validity of the previous models cannot be established, due to a lack of suitable experimental data.

A different approach to the modeling of equiaxed solidification is provided by the use of a so-called two-phase model [31,115,116]. Separate volume averaged conservation equations are utilized for the solid and liquid phases. Therefore, no assumption about the relationship between the liquid and solid velocities needs to be made, and phenomena such

as floating or settling of free solid grains can be modeled. In addition, the two-phase model distinguishes between the interfacial and bulk concentrations and temperatures, allowing for the prediction of liquid undercooling, microsegregation and other effects on a microscopic scale. Another key ingredient is the use of a transport equation for the number density of grains, which allows for the inclusion of nucleation and the calculation of the local dimension of grains [31]. Prakash [115,116] neglected the size influence of the grains on the transport and solidification phenomena. Beckermann and Ni [117,118] presented results for the macrosegregation pattern and final grain size distribution in equiaxed solidification of an Al-Cu alloy.

Most recently, Wang [119] introduced a multiphase model of equiaxed solidification that is patterned after the multi-phase/-scale approach outlined in Section 4, but includes melt convection and solid transport. Results were obtained for a number of cases involving equiaxed solidification of an Al-Cu alloy, and the model was partially validated against experiments using the transparent NH_4Cl-H_2O analogue alloy. In the following subsections, this model is presented and the critical model assumptions are discussed. Some of the work is of a rather preliminary nature, but the discussion will allow for the identification of future research needs.

5.2.1 Reduced Macroscopic Equations. As in Section 4, the system is assumed to be occupied by three phases: the solid, and the interdendritic and extradendritic liquids, which are separated by the dendrite envelope. Each of the three phases in V_o may have a different velocity, concentration, and temperature. Again, the solid/interdendritic interface is characterized by phase change, whereas the relative envelope motion is governed by dendrite tip growth. The following assumptions are introduced:

(1) Local mechanical equilibrium exists, i.e., $p_s = p_d = p_l = p$.

(2) The momentum exchange due to interfacial movement is neglected.

(3) A certain flow partitioning between the inter- and extra-dendritic regions is assumed. As schematically shown in Fig.31, the liquid may flow either through the inter- or the extra-dendritic region. The relative portions can be quantified by introducing a flow partition tensor, κ_v, which is defined as the ratio of the liquid mass flux through the porous dendrites to the total liquid mass flux; i.e.,

$$\varepsilon_d\rho_d(v_d - v_s) = \kappa_v \varepsilon_f\rho_f(v_f - v_s) \tag{61}$$

and

$$\varepsilon_l\rho_l(v_l - v_s) = (1 - \kappa_v)\varepsilon_f\rho_f(v_f - v_s) \tag{62}$$

where ε_f and v_f stand for the total liquid fraction, consisting of both the interdendritic and extradendritic phases, and the mixture velocity vector for both phases, respectively: $\varepsilon_f=\varepsilon_d + \varepsilon_l$, and $\varepsilon_f\rho_f v_f = \varepsilon_d\rho_d v_d + \varepsilon_l\rho_l v_l$. Note that when $\kappa_v=\rho_d\varepsilon_d/(\rho_f\varepsilon_f)$, a uniform flow distribution results; i.e., $v_d = v_l = v_f$. The coefficient κ_v is also called the fluid collection efficiency of porous aggregates in chemical engineering [120]. A correlation for κ_v is developed in a later section. The concept of flow partitioning between the inter- and extra-dendritic regions is introduced to simplify the solution of the momentum equations in the multiphase model. Once κ_v is calculated, only the momentum equation for the total liquid phase needs to be solved, and the individual liquid velocity fields, v_d and v_l, can be algebraically obtained from Eqs.(61) and (62).

(4) Local thermal equilibrium exists, i.e., $T_k = \overline{T}_{kj} = T$. The justification of this assumption is the same as in Section 5.1.

(5) The interdendritic liquid is well mixed so that $\overline{C}_{ds} = \overline{C}_{dl} = \overline{C}_{ld} = C_d = \overline{C}_e$. The validity of this assumption has been discussed in Section 4.

(6) The dendrite envelope is spherical.

(7) Thermophysical properties are the same for the interdendritic and extradendritic liquid phases.

(8) All dispersive fluxes are neglected.

As discussed in Assumption 3, only the solid and the total liquid phases require principal consideration. The distinction between the variables pertinent to the inter- and extra-dendritic liquids can be made algebraically after the primary variables pertinent to the total liquid phase (f) are obtained. These primary variables pertinent to the total liquid are defined by the rule-of-mixtures, i.e.,

volume fraction	$\varepsilon_f = \varepsilon_d + \varepsilon_l$	(63)
density	$\rho_f \varepsilon_f = \rho_d \varepsilon_d + \rho_l \varepsilon_l$	(64)
viscosity	$\rho_f \varepsilon_f \mu_f^* = \rho_d \varepsilon_d \mu_d^* + \rho_l \varepsilon_l \mu_l^*$	(65)
mass diffusivity	$\rho_f \varepsilon_f D_f^* = \rho_d \varepsilon_d D_d^* + \rho_l \varepsilon_l D_l^*$	(66)
thermal conductivity	$\varepsilon_f k_f^* = \varepsilon_d k_d^* + \varepsilon_l k_l^*$	(67)
specific heat	$\rho_f \varepsilon_f c_f = \rho_d \varepsilon_d c_d + \rho_l \varepsilon_l c_l$	(68)
concentration	$\rho_f \varepsilon_f C_f = \rho_d \varepsilon_d C_d + \rho_l \varepsilon_l C_l$	(69)
velocity	$\rho_f \varepsilon_f v_f = \rho_d \varepsilon_d v_d + \rho_l \varepsilon_l v_l$	(70)

With the assumptions stated above, a reduced set of model equations can be derived from the general formulation presented in Table 1. These equations are summarized in Table 3. Several observations on the equations listed in Table 3 are made in the following.

A. Remarks on the Model Equations

First, the phase change rate Γ_s, a critical parameter in the solidification model, is determined from the interfacial species balance listed in Table 3. Physically, this equation implies that the species flux rejected into the interdendritic liquid due to phase change (LHS) is either diffused into the solid and extradendritic liquid through interphase exchanges within the control volume (the 1st and 2nd terms on the RHS), or stored in the interdendritic region (3rd term on the RHS), or advected and diffused out of the control volume (4th and 5th terms on the RHS).

Secondly, the momentum equation for phase (f) is obtained by summing up the momentum conservation equations for phases (d) and (l) as listed in Table 1. The viscous terms are linear so that they are additive, whereas the summation of the nonlinear advective

terms results in an additional term (the last term on the RHS), where γ is called the momentum dispersion coefficient and is given by

$$\gamma = 1 - \rho_f \varepsilon_f \left[\frac{\kappa_v^2}{\rho_d \varepsilon_d} + \frac{(1-\kappa_v)^2}{\rho_l \varepsilon_l} \right] \tag{71}$$

When $\kappa_v = \rho_d \varepsilon_d / \rho_f \varepsilon_f$ (i.e., uniform flow through the inter- and extra-dendritic regions), $\gamma = 0$ so that the last term in the momentum equation for phase (f) vanishes. This is why γ is called the dispersion coefficient.

A similar term also arises in the species conservation equation for the total liquid phase of Table 3.

B. Secondary Variables

The model equations listed in Table 3 constitute a complete mathematical formulation for eight primary variables: ε_s, Γ_s, v_s, v_f, p, C_s, C_f and T, while the total liquid fraction, ε_f, can be obtained from the constraint: $\varepsilon_s + \varepsilon_f = 1$. All quantities pertinent to the interdendritic and extradendritic liquid phases are classified as secondary variables whose determination from the above primary variables is explained below.

To distinguish the interdendritic and extradendritic liquid fractions from the total liquid fraction ε_f, one can resort to the following mass conservation equation for the interdendritic liquid phase:

$$\frac{\partial}{\partial t}(\rho_d \varepsilon_d) + \nabla \cdot (\rho_d \varepsilon_d v_d) = \Gamma_e - \Gamma_s \tag{72}$$

where Γ_e is related to the growth velocity of the dendrite envelope:

$$\Gamma_e = S_e \rho_l \, \bar{w}_{ne} \tag{73}$$

Hence, the term Γ_e can be calculated from the growth model for the dendrite envelope, which is provided in Section 5.2.3. Once ε_d is obtained, the extradendritic liquid fraction is simply equal to $(\varepsilon_f - \varepsilon_d)$.

By definition, the extradendritic liquid concentration can be calculated, once C_f is available, from

$$C_l = (\rho_f \varepsilon_f C_f - \rho_d \varepsilon_d \bar{C}_e)/(\rho_l \varepsilon_l) \tag{74}$$

where the relation $C_d = \bar{C}_e$ has been used due to the assumption that the interdendritic liquid is well mixed, namely Assumption 5.

Likewise, the liquid velocities in the inter- and extra-dendritic regions are obtained, respectively, from the definition of the flow partition coefficient:

$$\mathbf{v}_d = \mathbf{v}_s + \kappa_v \frac{\rho_f \varepsilon_f}{\rho_d \varepsilon_d} (\mathbf{v}_f - \mathbf{v}_s) \tag{75}$$

$$\mathbf{v}_l = \mathbf{v}_s + (1-\kappa_v) \frac{\rho_f \varepsilon_f}{\rho_l \varepsilon_l} (\mathbf{v}_f - \mathbf{v}_s) \tag{76}$$

in which κ_v is calculated as shown in Section 5.2.4.

The above auxiliary relations for calculating the secondary variables from the primary variables are also summarized in Table 3. To complete the mathematical system, supplementary relations are, however, needed for the growth velocity of dendrite envelope $\bar{w}_{ne}$, the solid/liquid interfacial drag, M_s^d, the flow partition coefficient κ_v, the interfacial diffusion lengths, l_{sd} and l_{ld}, and the macroscopic transport properties as well. These additional inputs to the multiphase model are provided in the following subsections. The interfacial area concentrations, S_s and S_e, are given by the same morphological relations as those derived in Section 4.2.

5.2.2 Grain Nucleation. As an important microstructural parameter, the grain density is needed for the evaluation of the envelope area concentration, S_e (see Section 4.2). Due to solid motion, this grain density, n, is not only determined by nucleation mechanisms but also modified by the flow field during solidification, according to the following conservation equation [31]:

$$\frac{\partial n}{\partial t} + \nabla \cdot (\mathbf{v}_s n) = \dot{n} \tag{77}$$

where the second term on the LHS is the flux of grains due to a finite solid velocity, $\mathbf{v}_s$. The term $\dot{n}$ is the net nucleation rate accounting for both the birth and death of grains due to

heterogeneous nucleation, remelting, dendrite arm pinch-off, agglomeration and other effects. Although a number of semi-empirical nucleation models are available, they do not explicitly account for fragmentation and agglomeration effects in the presence of convection. The realistic modeling of grain structure formation on the macroscopic scale will largely depend on resolving these issues. Careful experimentation coupled with solutions of the present model equations may help in this respect. It is important to realize that for $v_s \neq 0$ the measured local grain density in a solidified structure has little in common with the number of grains that nucleated at that same location.

At the present time, the simplest nucleation model, namely the instantaneous nucleation model proposed by Stefanescu et al. [62] may be used, i.e. Eq.(34). However, due to the transport of grains, several complications arise. It is assumed that nucleation can only occur if the local grain density in a control volume before nucleation is equal to zero. This implies that no new grains will nucleate in the immediate neighborhood of existing grains that may have been transported into the control volume. In the presence of solid movement, grains may be advected into regions of higher temperature and remelt to a sufficiently small diameter d_{si}. In this case, death of the grains takes place, and the present nucleation model instantaneously resets the local grain density to zero. The control volume in question is then allowed to re-nucleate later when the conditions are right. Thus, grains may exist in regions of superheated melt as long as their diameter is above d_{si}.

5.2.3 Grain Envelope Growth. For convection-dominated dendrite tip growth, there is ample experimental evidence showing that both the stability criterion and the species gradients are affected by the flow field around the dendrite tips [121], and the diffusional model presented in Section 4.4 is not applicable. A reliable and accurate model accounting for the convection effects is, however, not yet available. To a first approximation, one can assume a negligible influence of convection on the stability criterion, and thus the focus can be placed on the fluid flow effect on the species transport field around the dendrite tips.

Considerable research has been conducted in the literature in order to find analytical solutions of the species transport problem around dendrite tips in the presence of convection. A summary has been given by Ananth and Gill [122]. It was found that the Stokes approximation of the Navier-Stokes equations for convection in a subcooled melt yields an exact solution for shape preserving growth of a parabolic dendrite. The solution was also found to be in good agreement with the available experimental data of Huang and Glicksman [123]. In terms of the tip Peclet number Pe_t and the dimensionless undercooling Ω, this solution can be written as

$$\Omega = 2Pe_t \left(\int_1^\infty \frac{\exp[-\int_1^\eta (f/\eta)d\eta]}{\eta} d\eta \right) \tag{78}$$

where the function $f(\eta)$ is given by

$$f(\eta) = 2Pe_t \eta^2 + \frac{2Pe_\infty}{E_1[(Pe_\infty + 2Pe_t)/Sc]} [\eta^2(2\ln \eta - 1) + 1] \tag{79}$$

and the ambient Peclet number is based on the relative velocity between the liquid and the solid dendrite; i.e.,

$$Pe_\infty = |v_l - v_s| R_t/D_l \tag{80}$$

When $Pe_\infty=0$, which implies no convection, Eq.(80) yields $f(\eta)=2Pe_t\eta^2$ and Eq.(78) reduces to the Ivantsov solution for pure diffusion as given in Eq.(47).

The solution of Eqs.(78-79) together with Eq.(45) provides a first-order approximation for convection-dominated dendrite tip growth. It should, however, be cautioned that much additional research remains to verify the applicability of this dendrite tip growth law in the presence of convection.

5.2.4 Solid/Liquid Interfacial Drag. The dissipative interfacial stress in a multiparticle system has traditionally been modeled using various approaches. For high solid fractions (i.e., the packed bed regime), the porous medium approach is often adopted

(see also Section 5.1), with the permeability representing a key parameter [124, 3]; while at low solid fractions (i.e., the free particle regime), the submerged object model is more frequently used in which the drag coefficient is important [125]. Recently, both approaches have been unified by Wang et al. [126] for the multiparticle system of equiaxed solidification, and a general correlation (valid for all solid fractions ranging from zero to unity) for the dissipative interfacial stress, M_s^d, on the solid crystals has been obtained; i.e.,

$$M_s^d = \varepsilon_f \beta^2 \frac{\mu_f}{R_e^2} \varepsilon_f (v_f - v_s) \tag{81}$$

where β is a dimensionless parameter which is only a function of the particle volume fraction and its morphology and R_e is the envelope radius. The expression for β is given by

$$\beta = \frac{\beta_d}{[(1 - \varepsilon_l)^n + (\beta_d/\beta_l)^{2n}]^{1/2n}} \tag{82}$$

where

$$\beta_d = \frac{3\sqrt{5}}{(1 - \varepsilon_{si})^{3/2}} \frac{S_s}{\phi_e S_e} \tag{83}$$

$$\beta_l = \left\{ \frac{9}{2}(1 - \varepsilon_l) \frac{2 + 4/3\eta^5}{2 - 3\eta + 3\eta^5 - 2\eta^6} \frac{1}{C_p(\phi_e)} \frac{2\beta_d^2 (1 - tanh\ \beta_d/\beta_d)}{2\beta_d^2 + 3(1 - tanh\ \beta_d/\beta_d)} \right\}^{1/2} \tag{84}$$

$$n = 0.176 log\ \beta_d + 0.275 \tag{85}$$

The function $C_p(\phi_e)$ accounts for the effect of an aspherical dendrite envelope, with ϕ_e being the sphericity of the dendrite envelope [39,127]. The following expression for $C_p(\phi_e)$ has been proposed by Wang et al. [126]:

$$C_p(\phi_e) = \begin{cases} \phi_e^2 & \text{for } 0.7 > \varepsilon_l > 0.0 \\ 1.26 log_{10}(\dfrac{\phi_e}{0.163}) & \text{for } 1 > \varepsilon_l > 0.7 \end{cases} \tag{86}$$

While other details on the drag model are available elsewhere [126], several salient features of the model are outlined here. First, note that this drag model accounts for the

multiple length scales present in a dendritic structure, namely S_s and S_e (or R_e). Secondly, the drag model encompasses many important limiting cases, which include the single equiaxed dendrite [59,127], and packed beds of impermeable and permeable spheres. Thirdly, the model has been validated against various experimental data available in the literature for both globular and dendritic equiaxed crystals [126]. In particular, it was found that this model improves the prediction of permeabilities of equiaxed dendritic structures due to its explicit consideration of multiple length scales. For spherical solid particles, this drag model reduces identically to the well known Stokes law for the drag coefficient in the free particle regime [125], while it coincides with the Kozeny-Carman permeability relation in the packed bed regime.

5.2.5 Flow Partitioning between Inter- and Extra-dendritic Regions. In equiaxed solidification, it can be assumed that the flow partition coefficient is isotropic, so that only a single value of κ_v is required. It has been shown by Wang et al. [126] that

$$\kappa_v = (1 - \varepsilon_l)(\beta/\beta_d)^2 \tag{87}$$

where β and β_d are given by Eqs.(82) and (83). Figure 32 illustrates the effects of the extradendritic liquid fraction, ε_l, and internal solid fraction, ε_{si} (i.e., the ratio of the solid fraction to the grain fraction), on the flow partition coefficient in an equiaxed dendritic system with S_s/S_e=0.1. As can be seen, the portion of the flow through the dendrites approaches zero in the free particle regime (i.e. higher ε_l). On the other hand, in the packed bed regime, the flow partition coefficient quickly increases as ε_l decreases and reaches unity at ε_l=0, at which point all flow must be through the interdendritic spaces.

5.2.6 Interfacial Mass Transfer. The solid diffusion length l_{sd} is the same as in the absence of convection, and thus Eq.(40) of Section 4.3 can be used. However, the liquid diffusion length ahead of the dendrite envelope, l_{ld}, needs to be modified to reflect the

effects of flow. This can be accomplished through the use of the following correlation [119]:

$$\frac{d_e}{l_d} = 2 + 0.865\left(\frac{C_\varepsilon}{\varepsilon_l}\right)^{1/3} Pe_\varepsilon^{1/3} \tag{88}$$

where

$$Pe_\varepsilon = \frac{\varepsilon_l |v_l - v_s| d_e}{D_l} \tag{89}$$

and

$$C_\varepsilon = \frac{2 + \frac{4}{3}(1-\varepsilon_l)^{5/3}}{2 - 3(1-\varepsilon_l)^{1/3} + 3(1-\varepsilon_l)^{5/3} - 2(1-\varepsilon_l)^2} \tag{90}$$

This correlation is based on the momentum-mass transfer analogy, and is derived along the same lines as the interfacial drag expressions given by Eqs.(88-90). A comparison between this correlation and Agarwal's formula [128], which was employed previously by Ni and Beckermann [117], indicated a discrepancy of less than 20 percent for all solid fractions [119]. In addition, it should be mentioned that the correlation given by Eqs.(88-90) neglects the effect of interfacial movement and does not reduce to Eq.(42) of Section 4.3 in the limit of Pe_ε=0. This may be justified by the fact that in the presence of convection, the convection effect overrides that of interfacial movement in determining mass transfer rates. Experimental work is underway to verify the above correlation for equiaxed dendritic solidification [129].

5.2.7 Macroscopic Transport Properties. The effective macroscopic viscosities μ_s^* and μ_l^* represent the rheological behavior of a multiphase mixture. They are dependent on the viscous properties and deformations of the phases, the flow field, and the distribution and geometry of the dispersed or suspended phase. To a first approximation, the liquid macroscopic viscosity can be taken to be equal to its microscopic counterpart; i.e.,

$$\mu_l^* = \mu_l \tag{91}$$

In modeling of the solid macroscopic viscosity, the packing limit must be taken into account when the grains impinge upon each other (i.e., when $\varepsilon_g=\varepsilon_g^c$), and form a coherent and rigid solid structure. In this limit, μ_s^* must approach an infinite value so that the macroscopic velocity gradients of the solid phase vanish. If the rigid solid is fixed to a wall, the solid velocity will then be uniformly equal to the velocity of the wall (which may be zero).

In the other extreme where $\varepsilon_g \to 0$, the seminal theory of Einstein predicts that $\mu_s^*=3.5\mu_l$ [130]. In solidification systems where the grain fraction may vary anywhere from zero to unity, a smooth transition between these two limits is necessary. Ni and Beckermann [117] proposed the use of the Krieger model [131], which results in the following expression for μ_s^*:

$$\mu_s^* = \frac{\mu_l}{\varepsilon_g}\left[(1 - \varepsilon_g/\varepsilon_g^c)^{-2.5\varepsilon_g^c} - (1 - \varepsilon_g)\right] \tag{92}$$

Note that the right hand side of Eq.(92) reduces to $3.5\,\mu_l$ for $\varepsilon_g \to 0$ and to an infinite value for $\varepsilon_g \geq \varepsilon_g^c$. It should also be emphasized that for dendritic structures, the solid viscosity is not directly dependent on the solid fraction but rather on the grain fraction. In other words, as soon as the grains reach the packing limit (ε_g^c is about 0.6), the solid structure becomes rigid, even though the solid fraction may be much lower than ε_g^c. There has been ample experimental evidence to support this hypothesis. For example, experimental data for different alloys [71,132] indicate that the packing limit can be reached at solid fractions between 0.1 and 0.3 in a large-grained casting where the grain fraction is much higher than the solid fraction. In contrast, in well-grain-refined castings, packing of the crystals was found to occur at much higher solid fractions, between 0.5 and 0.65. This is because the grain fraction is nearly equal to the solid fraction for small grains. Again, careful experimentation is needed to verify the use of Eq.(92).

As a first approximation, the macroscopic thermal conductivity and mass diffusivity are taken to be equal to their microscopic counterparts:

$$k_k^* = k_k \; ; \quad D_k^* = D_k \tag{93}$$

More discussion on these approximations can be found in Beckermann and Viskanta [8].

5.2.8 Application to Solidification of an Al-4wt% Cu Alloy. Illustrative numerical results have recently been reported by Wang and Beckermann [41] for a physical system consisting of a two-dimensional rectangular cavity, as shown in Fig.33. The left vertical wall is subject to convective cooling, while all other walls are adiabatic. The thermal conditions fall roughly into the range of equiaxed solidification according to the diagram of Kurz and Fisher [18]. The melt has an initial temperature of 930 K (10 K superheat) and initial concentration of 4 weight percent of copper in aluminum. In the Al-Cu system, the melt density increases with increasing copper concentration and decreasing temperature, so that the thermal and solutal buoyancy forces in and near the mushy zone augment each other. The solid density is generally greater than the liquid density [133]. Hence, crystal sedimentation is expected during solidification. The crystals may experience partial slip at the walls if the diameter of the grains is larger than the length scale of the surface roughness. To a first approximation, this effect may be modeled by the use of the following boundary condition [134]:

$$(v_s)_t \big|_w = -\lambda_p \frac{\partial (v_s)_t}{\partial n} \Big|_w \tag{94}$$

The mean distance between particles, λ_p, can be estimated from ([135])

$$\lambda_p = \frac{d_e}{\varepsilon_g^{1/3}} \tag{95}$$

For a small grain diameter, d_e, the slip coefficient λ_p approaches zero so that a no-slip condition for the grains results. Apparently, the issue of adhesion/separation of equiaxed grains at mold walls deserves further research attention. Other details of the numerical implementation may be found in Wang and Beckermann [41].

Representative results are shown in Fig.34 (at t=50 s) for a simulation where the nuclei density, n_o, in the nucleation law, Eq.(34), was arbitrarily set to 10^9 m^{-3}. The flow field (Fig.34a) indicates a strong downflow adjacent to the cold, left wall. This flow is not only driven by thermosolutal buoyancy forces, but also by the sedimentation of the solid grains. The relatively small crystals, nucleated near the wall exert a large interfacial drag on the liquid and "pull" it downward. Convection driven by sedimentation has been little researched. A crystal sediment bed can be observed in the bottom fourth of the cavity. The coherent and dense dendrite network in this bed forces the majority of the flow to bypass it. Above the packed bed, a mixture of solid and liquid flows simultaneously. An almost solid-free liquid region exists only in the upper one-third of the cavity, except for a narrow layer on the left side. The mixture concentration distribution (Fig.34b) shows that the relative motion between the liquid and solid phases causes negative segregation in the regions of higher solid fraction. The negative segregation is strongest at the bottom where the solute-poor crystals have settled. The isotherm plot in Fig.34c reveals that the lower right corner is as warm as the upper portion of the cavity. This is a consequence of the crystals that have settled there and are releasing a large amount of latent heat. The relative velocity vectors in Fig.34d are defined as $(\mathbf{v}_f - \mathbf{v}_s)$, and further illustrate the movement of the solid relative to the liquid. Above the packed bed, the relative velocity vectors are upwards, implying that the downward component of the solid velocity is larger than the one of the liquid; this is a direct evidence of sedimentation. In the packed bed region, on the other hand, the solid velocity vanishes ($\mathbf{v}_s$=0), so that the relative velocity vectors represent the liquid velocity only. In the upper one-third of the cavity, the nuclei are so small that the relative velocity vanishes.

The motion of the grains is illustrated in more detail in Fig.35. As already mentioned, the local grain density is not only determined by the nucleation rate, but is also influenced by the solid transport during solidification. It can be seen from Fig.35a that initially a stream of highly concentrated nuclei is swept into the central part of the cavity. At t=30 s

(Fig.35b), the crystals lifted by the liquid flow along the right wall begin to re-settle near the left wall. In addition, a central region of lower grain density appears. This is because the crystals in this region grew to such a large size that they settled down. This effect is more evident in Fig.35c (t=50 s), which shows a pronounced vertical variation in the nuclei density due to settling. The interface between the lower mushy zone and the upper nearly solid-free liquid region (compare to Fig.34a) coincides with a relatively sharp vertical gradient in the grain density. At t=100 s (Fig.35d), this interface is shifted upwards as the sediment bed increased in height. The grain density above the bed is comparably lower. An isolated region of lower grain density can also be observed at the bottom wall. This can be explained by a remelting phenomenon, which kills a number of grains. The remelting is due to the continued advection and deposition of solute-rich liquid in the already established sediment bed at the bottom, resulting in a severe depression of the liquidus temperature in this region.

The final grain size distribution is shown in Fig.36a. Note that in the absence of solid transport the grain size (i.e., radius) would be uniformly equal to 0.62 mm corresponding to $n_0=10^9$ m^{-3}. The top zone of larger grains (~2 mm) can be directly attributed to the sedimentation effect, while the large grains at the very bottom are due to the above explained remelting phenomenon. A string of relatively small grains (less than 0.5 mm) extends upwards from the lower-left corner and along the right wall. Referring back to Fig.35, it can be seen that the location of this string coincides with the path of the highly concentrated nuclei stream during the early parts of solidification. Also shown in Fig.36 is the final grain size distribution for another simulation, where the nuclei density, n_0, in the nucleation law was increased to 10^{11} m^{-3} (Fig.36b). This second simulation may be viewed to correspond to a more grain-refined casting. The resulting overall smaller grain size in this case has a profound effect on the solidification and transport phenomena [41]: (i) the equiaxed crystals tend to grow in a more globulitic fashion, and (ii) there is less relative motion between the liquid and solid phases due to the larger interfacial drag. One of

the consequences is a much more uniform grain size distribution in the case of $n_o=10^{11}$ m^{-3} (Fig.36b) than for 10^9 m^{-3} (Fig.36a).

The effects of solid transport and different grain sizes on macrosegregation are illustrated in Fig.37a to 37c, by comparing the results of three different simulations. Figure 37a corresponds to the case of a stationary solid phase, but with thermosolutal melt convection, and $n_o=10^9$ m^{-3}. Overall, large variations in the copper concentration are present. The most prominent feature is the channel segregates. As opposed to the Pb-Sn simulations presented in Section 5.1, the channels are oriented downward due to the different direction of the solutal buoyancy forces in the Al-Cu alloy. Also, a highly segregated Cu-rich region exists at the bottom of the cavity and near the right wall due to the advection of solute-rich liquid during solidification. This macrosegregation pattern should be contrasted with Figs.37b and 37c, which correspond to a moving solid phase and $n_o=10^9$ m^{-3} and 10^{11} m^{-3}, respectively. In general, the macrosegregation is much less severe than in Fig.37a, and no channel segregates are predicted. Since macrosegregation is due to relative motion between the solid and liquid phases, solid transport can be expected to reduce macrosegregation in the present system. However, in cases where the solute-rich liquid is less dense and the solute-poor solid is more dense than the initial melt (as, for example, for hypoeutectic Pb-Sn alloys) a counter-current liquid-solid flow would result, causing very strong macrosegregation [30]. Comparing Figs.37b and 37c, it can be seen that a finer grain size ($n_o=10^{11}$ m^{-3}) in the Al-Cu system results not only in a more uniform grain pattern, as already observed in Fig.36b, but also reduces the extent of macrosegregation (due to less relative phase motion).

5.2.9 Comparison of the Model Predictions with NH_4Cl-H_2O Experiments. Some limited validation of the model presented in Section 5.2 has been provided by Beckermann and Wang [136] through comparison of model predictions with the NH_4Cl-H_2O experiments of Beckermann et al. [21]. The test cell used in the experiments is

schematically illustrated in Fig.38a and consists of a square enclosure surrounded on four sides by heat exchangers through which a temperature-regulated coolant was circulated. Initially, the enclosure contained an NH_4Cl-70wt% H_2O solution slightly above the liquidus temperature. Upon initiation of cooling, melt convection and, with some delay, equiaxed solidification commenced. Density gradients were visualized using a shadowgraph system and internal cell temperatures were measured using small thermocouple probes. A description of the experiments can be found in [21].

In the simulation, measured cell wall temperatures were used as boundary conditions. Without presenting further details, a representative comparison of measured and predicted results at an intermediate time is shown in Figs.38b and 38c. There appears to be good agreement between the measured and predicted extent and shape of the bed of sedimented NH_4Cl crystals at the bottom of the enclosure. Considering that this bed is the result of complex melt convection and solid transport processes, even this limited comparison can be viewed as an encouraging result. The two most critical uncertainties were found to be the modeling of the generation of equiaxed crystals (the grain density, n_o, was adjusted in the model to achieve realistic crystal sizes) and their growth in the convecting melt (i.e., the dendrite tip growth and the convective mass transfer from the crystals, both of which control the internal solid fraction of the crystals). Future research will be aimed at resolving these issues.

5.3 Issues in Coupled Columnar and Equiaxed Solidification with Convection

Although Sections 5.1 and 5.2 show some promise with regard to modeling of purely columnar and equiaxed dendritic solidification, there are numerous additional issues that need to be addressed before coupled columnar/equiaxed solidification and the CET can be predicted for situations where convective transport is important. First, the columnar model presented in Section 5.1 needs to be extended to account for dendrite tip undercooling at the

columnar front, because without this undercooling the growth of equiaxed crystals ahead of the front would not be possible. This can be done using the multi-phase/-scale approach along the same lines as shown in Sections 4 and 5.2. Special attention needs to be paid to proper modeling of the flow in the columnar dendrite tip region, since it is in this region where dendrite/flow interactions are especially important.

Probably the most critical modeling element will be the development of quantitative models for the sources of equiaxed grains in the presence of convection. Convection is an important mechanism in the separation or fragmentation of dendrites. The small solid particles or fragments can be transported into the interior bulk melt where they may survive and grow into equiaxed crystals. Crystals have been found to separate from mold walls and from the upper, free liquid surface [26]. However, in the case of an already existing columnar mushy zone, separation of dendrite fragments ("grain multiplication") can occur in the columnar tip region or inside channel segregates. Two mechanisms have been proposed: (i) mechanical, by the shear forces of the melt flow [17] and (ii) localized remelting or "pinch off" [137], where coarsening kinetics play an important role [138]. All theories have been experimentally confirmed in various situations, and the different mechanisms may, in fact, operate simultaneously. To date, no quantitative models are available to predict the fragmentation occurrence and rate.

In the area of grain multiplication by localized remelting, some recent work by Paradies et al. [139] has shed considerable light on the physical phenomena involved and has produced some first quantitative measurements. The fragmentation rate was measured in a model experiment using the transparent SCN-acetone alloy and a growth chamber, where the melt flow was along the columnar mushy zone with a precisely controlled flow rate, concentration, and temperature. It was found that the dendrite side branches pinch off via localized melting occurring close to the primary dendrite stem. The imposed velocity of the melt flow altered the mushy zone morphology, and the fragmentation rate dramatically increased with the flow rate. In these experiments, the velocity, temperature, and

concentration were controlled globally, and the results were presented in terms of total system parameters, such as chamber Reynolds number and time from the start of the experiment. However, for this data to be useful in a continuum model (that solves for the velocity, concentration and temperature distributions), the fragmentation rate would need to be correlated in terms of the local parameters. Much work remains, and the need for more experiments cannot be overemphasized.

6. CONCLUSIONS AND RECOMMENDATIONS

This chapter has summarized a number of fundamental studies of alloy solidification, which have the goal of providing comprehensive models of the transport phenomena occurring at the system scale while accounting for microstructural interactions. A large variety of topics has been covered, ranging from diffusion dominated columnar and equiaxed dendritic solidification to the simultaneous presence of melt convection and solid transport. Nonetheless, all models propagate the same multiphase approach and the use of volume-averaged continuum equations for each phase. Although the general procedures are not new, their application to alloy solidification results in a unique framework for incorporating both micro- and macroscale effects. In any case, the key to successful modeling is the proper specification of the interface topology and the phase interactions. Several examples have demonstrated that in the case of diffusion dominated solidification, considerable progress has been made in the prediction of the compositional and structural features of solidified parts. With the consideration of convective transport, the field has moved away from traditional metallurgy into the domain of thermal scientists, who can bring their tools to bear. Improved communication and close collaboration will be necessary to resolve the many remaining modeling issues.

One advantage of the theoretical framework reviewed here is that it allows for the identification of the critical modeling elements requiring further research attention. The main issues can be summarized as follows:

- quantitative models for the origin and destruction of grains, especially in the presence of convection where fragmentation, agglomeration, remelting, etc. can become important;
- topological relations that do not rely on *a priori* knowledge of the dendrite shapes and also take into account the rapid changes in the interface geometry during the very initial and final growth stages;
- validated models for dendrite tip growth in an undercooled and convecting melt;
- improved multiparticle interfacial drag models, particularly at high liquid fractions;
- multiparticle interfacial solute transfer models, with and without convection, that are valid during solid/liquid phase change;
- models describing the two-phase rheology as a function of the microstructure;
- models for the effective thermal conductivities and mass diffusivities in the averaged equations for each phase;
- modeling of the dispersive fluxes in the presence of turbulent convection.

Other issues arise in the extension of the models to rapid solidification rates, multi-component alloys, realistic phase diagrams including the eutectic and peritectic reactions, mold filling, porosity formation, hot cracking, and others, none of which are discussed here. Furthermore, the modeling work must be accompanied by the development of improved numerical algorithms for multiphase problems.

In closing it should be noted that the transfer of this modeling and simulation technology to industry is taking place, to a large extent, through commercial casting solidification codes (see [15]). It is fortunate that these codes are finding rapid and widespread acceptance in industry and are being integrated with other product and manufacturing process design software. However, despite the obvious successes, caution should be exercised when using the codes, particularly because of the many modeling approximations or empiricism incorporated in some of them. As the appetite for more

advanced models continues to grow, the need for more fundamental research cannot be neglected.

REFERENCES

1. W. Oldfield, A Quantitative Approach to Casting Solidification: Freezing of Cast Iron, *Trans. ASM*, Vol.59, pp.945-959, 1966.
2. M.C. Flemings and G.E. Nero, Macrosegregation: Part I, *Trans. TMS-AIME*, Vol.239, pp.1449-1461, 1967.
3. M.C. Flemings, *Solidification Processing*, McGraw-Hill, New York, 1974.
4. M. Rappaz, Modeling of Microstructure Fromation in Solidification Processes, *Int. Mater. Rev.*, Vol.34, pp.93-123, 1989.
5. R. Viskanta, Mathematical Modeling of Transport Processes during Solidification of Binary Systems, JSME *Int. J.* , Vol.33, Series II, pp.409-423, 1990.
6. H.E. Huppert, The Fluid Mechanics of Solidfication, *J. Fluid Mech.*, Vol.212, pp.209-240, 1990.
7. F.P. Incropera and R. Viskanta, Effects of Convection on the Solidification of Binary Mixtures, presented at *Oji International Seminar on Advanced Heat Transfer in Manufacturing and Processing of New Materials*, Tomakomai, Hokkaido, Japan. Oct. 28-31, 1992.
8. C. Beckermann and R. Viskanta, Mathematical Modeling of Transport Phenomena during Solidification of Alloys, *Appl. Mechanics Review*, Vol.46, pp.1-27, 1993.
9. D.M. Stefanescu, Critical Review of the Second Generation of Solidification Models for Castings: Macro Transport -- Transformation, in *Modeling of Casting, Welding and Advanced Solidification Processes VI*, eds. by T.S. Piwonka, V.Voller and L. Katgerman, TMS, Warrendale, Pennsylvania, pp.3-20, 1993.
10. C. Beckermann, Modeling of Transport Phenomena in Mushy Zones, in *Modeling of Casting, Welding and Advanced Solidification Processes VI*, eds. by T.S. Piwonka, V.Voller and L. Katgerman, TMS, Warrendale, Pennsylvania, pp.181-192, 1993.

11. I. Ohnaka, Modeling of Fluid Flow and Solidification in Casting, in *Modeling of Casting, Welding and Advanced Solidification Processes VI*, eds. by T.S. Piwonka, V. Voller and L. Kategerman, TMS, Warrendale, Pennsylvania, pp.337-348, 1993.

12. V.R. Voller, M.S. Stachowicz and B.G. Thomas, *Materials Processing in the Computer Age*, Publication of TMS, Warrendale, Pennsylvania, 1991.

13. J.A. Sehkar and J. Dantzig, *Nature and Properties of Semi-Solid Materials*, TMS, Warrendale, Pennsylvania, 1991.

14. C. Beckermann, L.A. Bertram, S.J. Pien and R.E. Smelser, *Micro/Macro Scale Phenomena in Solidification*, ASME HTD-Vol.218, ASME, New York, 1992.

15. T.S. Piwonka, V.R. Voller and L. Kategerman, *Modeling of Casting, Welding and Advanced Solidification Processes VI*, TMS, Warrendale, Pennsylvania, 1993.

16. W.C Winegard, *An Introduction to the Solidification of Metals*, Institute of Metals, London, 1964.

17. B. Chalmers, *Principles of Solidification*, John Wiley, New York, 1964.

18. W. Kurz and D.J. Fisher, *Fundamentals of Solidification*, 3rd ed., Trans Tech, Aedermannsdorf, Switzerland, 1989.

19. A.P. Hohaus, Übergang von der transkristallinen zur globulitischen Erstarrung, *Diplom Thesis*, RWTH Aachen, Aachen, Germany, 1993.

20. A. Hellawell, J.R. Sarazin and R.S. Stuebe, Channel Convection in Partly Solidified Systems, *Phil. Trans. R. Soc. Lond. A*, Vol.345, pp.507-544, 1993.

21. C. Beckermann, R.J. Feller, T.R. Irwin, H. Muller-Spath and C.Y. Wang, Visualization of Sedimentation and Thermo-Solutal Convection during Equiaxed Alloy Solidification, *AIAA 94-0570*, Reno, Nevada, 1994.

22. S. Engler and K. Göckmann, Zur Enstehung der Gussstruktur bei Gericteter Erstarrung, *Metall*, Vol.29, pp.252-263, 1975.

23. D.G. McCartney, Grain Refining of Aluminum and its Alloys Using Inoculants, *Int. Mat. Rev.*, Vol.34, pp.247-260, 1989.

24. C.Y. Wang and C. Beckermann, Prediction of Columnar to Equiaxed Transition during Diffusion-Controlled Dendritic Alloy Solidification, *Metall. Mater. Trans. A*, Vol.25A, pp.1081-1093, 1994.

25. I. Ziv and F. Weinberg, The Columnar-to-Equiaxed Transition in Al 3 pct Cu, *Metall. Trans. B*, Vol.20B, pp.731-734, 1989.

26. A. Ohno, *Solidification, the Separation Theory and Its Practical Applications*, Springer-Verlag, Heidelberg, 1987.

27. T.L. Finn, M.G. Chu and W.D. Bennon, The Influence of Mushy Region Microstructure on Macrosegregation in Direct Chill Cast Aluminum-Copper Round Ingots, in *Micro/Macro Scale Phenomena in Solidification*, eds. by C. Beckermann et al., ASME HTD-Vol.218, pp.17-26, 1992.

28. H. Yu and D.A. Ganger, Macrosegregation in Aluminum Alloy Ingot Cast by the Semicontinuous Direct Chill Method, in *Physical and Mechanical Properties*, Vol.1, pp.17-29, Proceedings of the International Conference, Charlottesville, VA, published by EMAS, UK.

29. W. Böhmer, personal communication, Iowa City, Iowa, 1994.

30. H.C. de Groh III and V. Laxmann, Macrosegregation in Undercolled Pb-Sn Eutectic Alloys, in *Solidification Processing of Eutectic Alloys*, eds. by D.M. Stefanescu et al., The Metallurgical Society, pp.229-242, 1988.

31. J. Ni and C. Beckermann, A Volume-Averaged Two-Phase Model for Transport Phenomena during Solidification, *Metall. Trans. B*, Vol.22B, pp.349-361, 1991.

32. S. Ganesan and D.R. Poirier, Conservation of Mass and Momentum for the Flow of Interdendritic Liquid during Solidification, *Metall. Trans. B*, Vol.21B, pp.173-181, 1990.

33. I. Dustin and W. Kurz, Modeling of Cooling Curves and Microstructures during Equiaxed Dendritic Solidification, *Z. Metallkd.*, Vol.77, pp.265-273, 1986.

34. M. Rappaz and Ph. Thevoz, Solute Diffusion Model for Equiaxed Dendritic Growth, *Acta Metall.*, Vol. 35, pp.1487-1497, 1987.

35. M. Rappaz and Ph. Thevoz, Solute Diffusion Model for Equiaxed Dendritic Growth: Analytical Solution, *Acta Metall.* , Vol.35, pp.2929-2933, 1987.

36. S.C. Flood and J.D. Hunt, A Model of a Casting, *Appl. Sci. Res.*, Vol.44, pp.27-42, 1987.

37. B. Giovanola and W. Kurz, Modeling of Microsegregation under Rapid Solidification Conditions, *Metall Trans. A*, Vol.21A, pp.260-263, 1990.

38. R.C. Kerr, A.W. Woods, M.G. Worster and H.E. Huppert, Solidification of an Alloy Cooled from above. Part 2. Non-Equilibrium Interfacial Kinetics, *J. Fluid Mech.*, Vol.217, pp.331-348, 1990.

39. C.Y. Wang and C. Beckermann, A Multiphase Solute Diffusion Model for Dendritic Alloy Solidification, *Metall. Trans. A*, Vol.24A, pp.2787-2802, 1993b.

40. C.Y. Wang and C. Beckermann, A Unified Solute Diffusion Model for Columnar and Equiaxed Dendritic Alloy Solidification, *Mater. Sci. and Eng. A*, Vol.A171, pp.199-211, 1993c.

41. C.Y. Wang and C. Beckermann, Multi-Scale/-Phase Modeling of Dendritic Alloy Solidification, to be presented at *Symposium on Transport Phenomena in Solidification* at the ASME Winter Annual Meeting, Chicago, November, 1994.

42. N. Wakao and J.M. Smith, Diffusion in Catalyst Pellets, *Chem. Eng. Sci.*, Vol.17, pp.825-834, 1962.

43. O.A. Plumb and S. Whitaker, Adsorption and Dispersion in Porous Media: Small-Scale Averaging and Local Volume Averaging, in *Dynamics of Fluids in Hierarchical Porous Media*, J.H. Cushman, ed., Academic Press, London, Chap.**5**, pp.97-148, 1990.

44. M. Kaviany, *Principles of Heat Transfer in Porous Media*, Springer-Verlag, New York, 1991.

45. C.Y. Wang and C. Beckermann, Single- vs. Dual-Scale Volume Averaging for Heteregeneous Multiphase Systems, *Int. J. Multiphase Flow*, Vol.19, pp.397-407, 1993a.

46. D.A. Drew, Mathematical Modeling of Two-Phase Flow, *Ann. Rev. Fluid Mech.*, Vol.15, pp.261-291, 1983.

47. S.M. Hassanizadeh and W.G. Gray, General Conservation Equations for Multi-Phase Systems: 1. Averaging Procedure, *Adv. Wat. Resour.*, Vol.2, pp.131-144, 1979.

48. S.M. Hassanizadeh and W.G. Gray, General Conservation Equations for Multi-Phase Systems: 2. Mass, Momentum, Energy and Entropy Equations, *Adv. Wat. Resour.*, Vol.2, pp.191-208, 1979.

49. S.M. Hassanizadeh and W.G. Gray, General Conservation Equations for Multi-Phase Systems: 3. Constitutive Theory for Porous Media, *Adv. Wat. Resour.*, Vol.3, pp.25-41, 1980.

50. M. Ishii, *Thermo-Fluid Dynamic Theory of Two-Phase Flow*, Eyrolles, Paris, 1975.

51. S.P. Marsh and M.E. Glicksman, A Stereological Basis for Numerical Implementation of Microstructure and Defect Models in Casting Simulations, in *Modeling of Casting, Welding and Advanced Solidification Processes VI*, eds. by T.S. Piwonka, V.Voller and L. Kategerman, TMS, Pennsylvania, pp.55-62, 1993.

52. M.E. Glicksman, R.N. Smith, S.P. Marsh and R. Kuklinski, Mushy Zone Modeling with Microstructural Coarsening Kinetics, *Metall. Trans. A*, Vol.23A, pp.659-667, 1992.

53. R.T. DeHoff and F.N. Rhines, *Quantitative Microscopy*, McGraw-Hill, New York, 1968.

54. R.B. Bird, W.E. Stewart and E.N. Lightfoot, *Transport Phenomena*, John Wiley, New York, 1960.

55. T.Z. Kattamis, J.C. Coughlin and M.C. Flemings, Influence of Coarsening on Dendritic Arm Spacing of Aluminum-Copper Alloys, *Trans. TMS-AIME*, Vol.239, pp.1504-1511, 1967.

56. S.P. Marsh and M.E. Glicksman, Thermal and Micro-Structure Characteristics of Mushy Zones, in Modeling and Control of Casting and Welding Processes IV, eds. by A.F. Giame and G.J. Abbashian, TMS, Warrendale, PA, pp.15-23, 1988.

57. M. Avrami, Kinetics of Phase Change II. Transformation--Time Relations for Random Distribution of Nuclei , *J. Chem. Phys.*, Vol.8, pp.212-224, 1940.

58. G.R. Speich and R.M. Fisher, Recrystallization of a Rapidly Heated 31/4% Silicon Steel, in Margolin, H. (ed.) *Recrystallization, Grain Growth and Textures*, ASM, Metals Park, OH, pp.563-598, 1966.

59. S. Ahuja, Solid/Liquid Interfacial Drag in Equiaxed Solidification, *M.S.M.E. Thesis*, The University of Iowa, Iowa City, 1992.

60. D. Turnbull, Kinetics of Heterogeneous Nucleation, *J. Chem. Phys.*, Vol.18, p.198, 1950.

61. Ph. Thevoz, J.L. Desbiolles and M. Rappaz, Modeling of Equiaxed Microstructure Formation in Casting, *Metall. Trans. A*, Vol.20A, pp.311-322, 1989.

62. D.M. Stefanescu, G. Upadhya and D. Bandyopahyoy, Heat Transfer-Solidification Kinetics Modeling of Solidification of Castings, *Metall. Trans. A*, Vol.21A, pp.997-1005, 1990.

63. J.D. Hunt, *Solidification and Casting of Metals*, Metal Society, London, pp.1-9, 1979.

64. I. Ohnaka, Mathematical Analysis of Solute Redistribution during Solidification with Diffusion in Solid Phase, *Trans ISIJ*, Vol.26, pp.1045-1051, 1986.

65. L. Nastac and D.M. Stefanescu, An Analytical Model for Solute Redistribution during Solidification of Planar, Columnar, or Equiaxed Morphology, *Metall. Trans. A*, Vol.24A, pp.2107-2118, 1993.

66. J. Lipton, M.E. Glicksman and W. Kurz, Dendritic Growth into Undercooled Alloy Melts, *Mater. Sci. and Eng.*, Vol.65, pp.57-63, 1984.

67. S. Kobayashi, A Mathematical Model for Solute Redistribution during Solidification, *J. Crystal Growth*, Vol.88, pp.87-96, 1988.

68. H.B. Brody and M.C. Flemings, Solute Redistribution in Dendritic Solidification, *Trans. AIME* , Vol.236, pp.615-624, 1966.

69. T.W. Clyne and W. Kurz, Solute Redistribution during Solidification with Rapid State Diffusion, *Metall. Trans. A*, Vol.12A, pp.965-971, 1981.

70. T.P. Battle, Mathematical Modeling of Solute Segregation in Solidifying Materials, *Int. Mat. Rev.*, Vol.37, pp.249-270, 1992.

71. M.C. Flemings, Behaviors of Metal Alloys in the Semi-Solid State, *Metall. Trans. A*, Vol.22A, pp.957-981, 1991.

72. W. Kurz, B. Giovanola and R. Trivedi, Theory of Microstructural Development during Rapid Solidification, *Acta Metall.*, Vol.34, pp.823-830, 1986.

73. L.A. Bendersky and W.J. Boettinger, Cellular Microsegregation in Rapidly Solidified Ag-15wt% Cu Alloys, in *Rapidly Quenched Metals*, eds. by S. Warlimont, Vol.1, pp.887-890, Elsevier Sci. Publishers, 1985.

74. J.A. Sarreal and G.J. Abbaschian, The Effect of Solidification Rate on Microsegregation, *Metall. Trans. A*, Vol.17A, pp.2063-2073, 1986.

75. T.P. Battle and R.D. Pelhke, Mathematical Modeling of Microsegregation in Binary Metallic Alloys, *Metall. Trans.*, Vol. 21B, pp.357-375, 1990.

76. A. Roosz and H. E. Exner, A Complete Model for Microsegregation during Columnar Dendrite Growth, in *Modeling of Casting, Welding and Advanced Solidification Processes VI*, eds. by T.S. Piwonka, V. Voller and L. Kategerman, TMS, Warrendale, Pennsylvania, pp.243-250, 1993.

77. V.R. Voller and S. Sundarraj, A Comprehensive Microsegregation Model for Binary Alloys, in *Modeling of Casting, Welding and Advanced Solidification Processes VI*,

eds. by T.S. Piwonka, V. Voller and L. Kategerman, TMS, Warrendale, Pennsylvania, pp.251-259, 1993.

78. J.D. Hunt, Steady State Columnar and Equiaxed Growth of Dendrites and Eutectics,*Mat. Sci. Eng.*, Vol.65, pp.75-83, 1984.

79. S.G.R. Brown and J.A. Spittle, Computer Simulation of Grain Growth and Macrostructure Development during Solidification, *Mat. Sci. Tech.*, Vol.5, pp.362-368, 1989.

80. P. Zhu and R.W. Smith, Dynamic Simulation of Crystal Growth by Monte Carlo Method---II. Ingot Microstructures, *Acta Metall. Mater.*, Vol.40, pp.3369-3379, 1992.

81. M. Rappaz and Ch.-A. Gandin, Probabilistic Modeling of Microstructure Formation in Solidification Processes, *Acta Metall. Mater.*, Vol.42, pp.345-360, 1993.

82. R.B. Mahapatra and F. Weinberg, The Columnar to Equiaxed Transition in Tin-Lead Alloys, *Metall. Trans. B*, Vol.21B, pp.425-432, 1987.

83. F. Weinberg, Recent Research in Solidification, in *Proc. of F. Weinberg Int. Symp. on Solidification Processing*, eds. by J.E. Lait and I.V. Samarasekera, Pergamon press, pp.3-11, 1990.

84. J. Lipton, W. Heinemann and W. Kurz, Columnar to Equiaxed Transition (CET) in Castings --- Part I: Determination of the CET from Cooling Curves, *Arch. Eisenhuttenwes.*, Vol.55, pp.195-200, 1984.

85. S.G.R. Brown and J.A. Spittle, A 2D Implicit Finite Difference Model to Simulate the Columnar to Equiaxed Zone Transition, in *Modeling of Casting, Welding and Advanced Solidification Processes V*, eds. by M. Rappaz, M.R. Ozgu and K.W. Mahin, TMS, Warrendale, PA, pp.395-402, 1991.

86. W.D. Bennon and F.P. Incropera, The Evolution of Macrosegregation in Statically Cast BInary Ingots, *Metall. Trans. B*, Vol.18B, pp.611-616, 1987.

87. C. Beckermann and R. Viskanta, Double-Diffusive Convection during Dendritic Solidification of a Binary Mixture, *PhysicoChem. Hydrodyn.*, Vol.10, pp.195-213, 1988.

88. V.R. Voller, A.D. Brent and C. Prakash, The Modelling of Heat, Mass and Solute Transport in Solidification Systems, *Int. J. Heat Mass Transfer*, Vol.32, pp.1719-1731, 1989.

89. G. Amberg, Computation of Macrosegregation in an Iron-Carbon Cast, *Int. J. Heat Mass Transfer*, Vol.34, pp.217-227, 1991.

90. S.D. Felicelli, F.C. Heinrich and D.R. Poirier, Simulation of Freckles during Vertical Solidification of Binary Alloys, *Metall. Trans. B*, Vol.22B, pp.847-859, 1991.

91. P.J. Prescott and F.P. Incropera, Numerical Simulation of a Solidifying Pb-Sn Alloy: The Effects of Cooling Rate on Thermosolutal Convection and Macrosegregation, *Metall. Trans. B*, Vol.22B, pp.529-540, 1991.

92. D.G. Neilson and F.P. Incropera, Effect of Rotation on Fluid Motion and Channel Formation during Unidirectional Solidification of a Binary Alloy, *Int. J. Heat Mass Transfer*, Vol.36, pp.489-503, 1993.

93. M.C. Schneider and C. Beckermann, A Numerical Study of the Combined Effects of Microsegregation, Mushy Zone Permeability and Contraction Driven Flow on Macrosegregation and Eutectic Formation in Binary Alloy Solidification, submitted to *Int. J. Heat Mass Transfer*, 1994.

94. M. Rappaz and V.R. Voller, Modeling of Micro-Macrosegregation in Solidification Processes, *Metall. Trans. A*, Vol.21A, pp.749-753, 1990.

95. M.C. Schneider and C. Beckermann, Effects of Simplified Enthalpy Relations on the Prediction of Heat Transfer during Solidification of a Lead-Tin Alloy, *Appl. Math. Modelling*, Vol.15, pp.596-605, 1991.

96. D.R. Poirier, P.J. Nandapurkar and S. Ganesan, The Energy and Solute Conservation Equations for Dendritic Solidification, *Metall. Trans. B*, Vol.22B, pp.889-900, 1991.

97. D.R. Poirier, Permeability for Flow of Interdendritic Liquid in Columnar-Dendritic Alloys, *Metall. Trans. B*, Vol.18B, pp.245-255, 1987.

98. C.Y. Liu, K. Murakami and T. Okamoto, Permeability of Dendrite Network of Cubic Alloys, *Mat. Sci. Tech.*, Vol.5, pp.1148-1152, 1989.

99. S. Ganesan, C.L. Chan and D.R. Poirier, Permeability for Flow Parallel to Primary Dendrite Arms, *Mat. Sci. Eng.*, Vol.A151, pp.97-105, 1992.

100. S.K. Sinha, T. Sundararajan and V.K. Garg, A Variable Property Analysis of Alloy Solidification using the Anisotropic Porous Medium Approach, *Int. J. Heat Mass Transfer*, Vol.35, pp.2865-2877, 1992.

101. H. Yoo and R. Viskanta, Effect of Anisotropic Permeability on the Transport Process during Solidification of a Binary Mixture, *Int. J. Heat Mass Transfer*, Vol.35, pp.2335-2346, 1992.

102. K.C. Chiang and H.L. Tsai, Shrinkage-Induced Fluid Flow and Domain Change in Two-Dimensional Alloy Solidification, *Int. J. Heat Mass Transfer*, Vol.35, pp.1763-1770, 1992.

103. K.C. Chiang and H.L. Tsai, Interaction between Shrinkage-Induced Fluid Flow and Natural Convection during Alloy Solidification, *Int. J. Heat Mass Transfer*, Vol.35, pp.1771-1778, 1992.

104. J.H. Chen and H.L. Tsai, Inverse Segregation for a Unidirectional Solidification of Aluminum-Copper Alloys, *Int. J. Heat Mass Transfer*, Vol.36, pp.3069-3075, 1993.

105. Q.Z. Diao and H.L. Tsai, Modeling of Solute Redistribution in the Mushy Zone during Solidification of Aluminum-Copper Alloys, *Metall. Trans. A*, Vol.24A, pp.963-973, 1993.

106. Q.Z. Diao and H.L. Tsai, The Formation of Negative and Positive Segregated Bands during Solidification of Aluminum-Copper Alloys, *Int. J. Heat Mass Transfer*, Vol.36, pp.4299-4305, 1993.

107. Q.Z. Diao and H.L. Tsai, Modeling of the Formation of Under-Riser Macrosegregation during Solidification of Binary Alloys, *Metall. Trans. A*, Vol.25A, pp.1051-1062, 1994.

108. D. Xu and Q. Li, Numerical Method for Solution of Strongly Coupled Binary Alloy Solidification Problems, *Numer. Heat Transfer A*, Vol.20A, pp.181-201, 1991a.

109. D. Xu and Q. Li, Gravity- and Solidification-Shrinkage-Induced Liquid Flow in a Horizontally Solidified Alloy Ingot, *Numer. Heat Transfer A*, Vol.20A, pp.203-221, 1991b.

110. D. Xu, Q. Li and R.D. Pehlke, Computer Simulation of Al-Cu Alloy Solidification using a Continuum Model, *AFS Trans.*, Vol.91, pp.737-745, 1991.

111. C.M. Oldenburg and F.J. Spera, Hybrid Model for Solidification and Convection, *Numer Heat Transfer Part B*, Vol.21, pp.217-229, 1992.

112. S.C. Flood, L. Kategerman and V.R. Voller, The Calculation of Macrosegregation and Heat and Fluid Flows in the DC Casting of Aluminum Alloys, in *Modeling of Casting, Welding and Advanced Solidification Processes V*, eds. by M. Rappaz, M.R. Ozgu and K.W. Mahin, TMS, Warrendale, Pennsylvania, pp.683-690, 1991.

113. V.R. Voller, Effect of Solidification Morphology on the Macroscopic Behavior of Solidification Systems, presented at *NATO Advanced Research Workshop on Interactive Dynamics in Convection and Solidification*, Chamonix, France, 1992.

114. P.J. Prescott, F.P. Incropera and D.R. Gaskell, The Effects of Undercooling, Recalescence and Solid Transport on the Solidification of Binary Metal Alloys, presented at *28th Nat. heat Transfer Conf.*, ASME, New York, 1992.

115. C. Prakash, Two-Phase Model for Binary Solid-Liquid Phase Change, Part I: Governing Equations, *Numer Heat Transfer Part B*, Vol.18, pp.131-145, 1990.

116. C. Prakash, Two-Phase Model for Binary Solid-Liquid Phase Change, Part II: Some Illustrative Examples, *Numer Heat Transfer Part B*, Vol.18, pp.147-167, 1990.

117. J. Ni and C. Beckermann, Modeling of Globulitic Alloy Solidification with Convection, *J. Materals Processing & Manufacturing Science*, Vol.2, pp.217-231, 1993.

118. C. Beckermann and J. Ni, Modeling of Sedimentation in Equiaxed Alloy Solidification, presented at *TMS 1993 Fall Meeting*, Pittsburgh; also *Metall. Mater. Trans. B*, under review, 1994.

119. C.Y. Wang, Multi-Scale/-Phase Modeling of Dendritic Alloy Solidification, *Ph.D Thesis*, The University of Iowa, Iowa City, 1994.

120. P.M. Adler, Streamlines in and around Porous Particles, *J. Coll. Int. Sci.*, Vol.81, pp.531-535, 1981.

121. Y.-W. Lee, R. Ananth and W.N. Gill, Selection of a Length Scale in Unconstrained Dendritic Growth with Convection in the Melt, *J. Crystal Growth*, Vol.132, pp.226-230, 1993.

122. R. Ananth and W.N. Gill, Self-Consistent Theory of Dendritic Growth with Convection, *J. Crystal Growth*, Vol.108, pp.173-189, 1991.

123. S.C. Huang and M.E. Glicksman, Fundamentals of Dendritic Solidification -- I. Steady-State Tip Growth, *Acta Metall.*, Vol.29, pp.701-715, 1981.

124. P.C. Carman, *Flow of Gases through Porous Media*, Butterworth Scientific, London, 1956.

125. J. Happel and H. Brenner, *Low Reynolds Number Hydrodynamics*, Noordhoff International Publishing, 1976.

126. C.Y. Wang, S. Ahuja, C. Beckermann and H.C. de Groh III, Multiparticle Interfacial Drag in Equiaxed Solidification, *Metall. Mater. Trans. B*, accepted for publication, 1994.

127. H.C. de Groh III, P.D. Weidman, R. Zakhem, S. Ahuja and C. Beckermann, Calculation of Dendrite Settling Velocity Using a Porous Envelope, *Metall. Trans. B*, Vol.24B, pp.749-753, 1993.

128. P.K. Agarwal, Transport Phenomena in Multi-Particle Systems -- II. Particle-Fluid Heat and Mass Transfer, *Chem. Sci. Eng.*, Vol.43, pp.2501-2510, 1988.

129. A. Ramani, personal communication, Iowa City, Iowa, 1994.

130. R.H. Davis, Microhydrodynamics of Particulate Suspensions, *Adv. in Colloid Interface Science*, Vol.43, pp.17-50, 1993.

131. I.M. Krieger, Rheology of Monodisperse Lattices, *Adv. in Coll. Interf. Sci.*, Vol.3, pp.111-136, 1972.

132. L. Arnberg, G. Chai and L. Backerud, Determination of Dendritic Coherency in Solidifying Melts by Rheological Measurements, *Mat. Sci. Eng.*, Vol.A173, pp.101-103, 1993.

133. S. Ganesan and D.R. Poirier, Densities of Aluminum-Rich Aluminum-Copper Alloys during Solidification, *Metall. Trans. A*, Vol.18A, pp.721-723, 1987.

134. S.M. Eldighidy, R.Y. Chen and R.A. Comparin, Deposition of Suspensions in the Entrance of a Channel, *ASME J. Fluid Eng.*, Vol.99, pp.365-370, 1977.

135. J. Ding and D. Gidaspow, A Bubble Fluidization Model Using Kinetic Theory of Granular Flow, *AIChE J.*, Vol.36, pp.523-538, 1990.

136. C. Beckermann and C.Y. Wang, Equiaxed Dendritic Solidification with Convection. Part III: Comparisons with NH_4Cl-H_2O Experiments, in preparation, 1994.

137. K.A. Jackson, J.D. Hunt, D.R. Uhlmann and T.R. Seward, On the Origin of of the Equiaxed Zone in Castings, *Trans. AIME*, Vol.236, pp.149-158, 1966.

138. R.S. Steube and A.Hellawell, An Alternative Approach to Medeling of the Grain Structure of Castings, in *Micro/Macro Scale Phenomena in Solidification*, eds. by C. Beckermann, L.A. Bertram, S.J. Pien and R.E. Smelser, ASME HTD-Vol.218, 1992.

139. C.J. Paradies, G.T. Kim, M.E. Glicksman and R.N. Smith, The Effect of Flow Interactions with Dendritic Mushy Zones: A Model Experiment, in *Modeling of Casting, Welding and Advanced Solidification Processes VI*, eds. by T.S. Piwonka et al., TMS, Warrendale, PA, pp.309-316, 1993.

List of Tables

Table 1. Summary of the microscopic and macroscopic conservation equations together with some constitutive relations

	Microscopic conservation equations	Macroscopic conservation equations	Interfacial balances	Dispersive fluxes
Mass	$\frac{\partial}{\partial t}\rho_k + \nabla\cdot(\rho_k \mathbf{v}_k) = 0$	$\frac{\partial}{\partial t}(\varepsilon_k\rho_k) + \nabla\cdot(\varepsilon_k\rho_k\langle \mathbf{v}_k\rangle^k) = \sum_{j,j\neq k}\Gamma_{kj}$	$\Gamma_{kj}+\Gamma_{jk}=0$	—
Momentum	$\frac{\partial}{\partial t}(\rho_k\mathbf{v}_k) + \nabla\cdot(\rho_k\mathbf{v}_k\mathbf{v}_k) =$ $-\nabla p_k + \nabla\cdot\tau_k + \mathbf{b}_k$	$\frac{\partial}{\partial t}(\varepsilon_k\rho_k\langle \mathbf{v}_k\rangle^k) + \nabla\cdot(\varepsilon_k\rho_k\langle \mathbf{v}_k\rangle^k\langle \mathbf{v}_k\rangle^k) =$ $-\varepsilon_k\nabla\langle p_k\rangle^k + \nabla\cdot(\langle\tau_k\rangle + \langle\tau_k^t\rangle) + \sum_{j,j\neq k}\mathbf{M}_{kj} + \varepsilon_k\langle \mathbf{b}_k\rangle^k$	$\mathbf{M}_{kj}+\mathbf{M}_{jk}=0$	$\langle\tau_k^t\rangle = -\langle\rho_k\hat{\mathbf{v}}_k\hat{\mathbf{v}}_k\rangle$
Energy	$\frac{\partial}{\partial t}(\rho_k h_k) + \nabla\cdot(\rho_k h_k\mathbf{v}_k) =$ $-\nabla\cdot\mathbf{q}_k$	$\frac{\partial}{\partial t}(\varepsilon_k\rho_k\langle h_k\rangle^k) + \nabla\cdot(\varepsilon_k\rho_k\langle h_k\rangle^k\langle \mathbf{v}_k\rangle^k) =$ $-\nabla\cdot(\langle\mathbf{q}_k\rangle + \langle\mathbf{q}_k^t\rangle) + \sum_{j,j\neq k}Q_{kj}$	$Q_{kj}+Q_{jk}=0$	$\langle\mathbf{q}_k^t\rangle = \langle\rho_k\hat{h}_k\hat{\mathbf{v}}_k\rangle$
Species	$\frac{\partial}{\partial t}(\rho_k C_k) + \nabla\cdot(\rho_k C_k\mathbf{v}_k) =$ $-\nabla\cdot\mathbf{j}_k$	$\frac{\partial}{\partial t}(\varepsilon_k\rho_k\langle C_k\rangle^k) + \nabla\cdot(\varepsilon_k\rho_k\langle C_k\rangle^k\langle \mathbf{v}_k\rangle^k) =$ $-\nabla\cdot(\langle\mathbf{j}_k\rangle + \langle\mathbf{j}_k^t\rangle) + \sum_{j,j\neq k}J_{kj}$	$J_{kj}+J_{jk}=0$	$\langle\mathbf{j}_k^t\rangle = \langle\rho_k\hat{C}_k\hat{\mathbf{v}}_k\rangle$

	Total interfacial transfers	Interfacial transfers due to phase change	Interfacial stress and transfers due to diffusion/convection
Mass	Γ_{kj}	$\Gamma_{kj} = -\frac{1}{V_o}\int_{A_{kj}}\rho_k(\mathbf{v}_k - \mathbf{w}_k)\cdot\mathbf{n}_k\,dA = S_{kj}\rho_k\overline{w}_{nkj}$	---
Momentum	$\mathbf{M}_{kj} = \mathbf{M}_{kj}^{\Gamma} + \mathbf{M}_{kj}^{d}$	$\mathbf{M}_{kj}^{\Gamma} = -\frac{1}{V_o}\int_{A_{kj}}\rho_k\mathbf{v}_k(\mathbf{v}_k - \mathbf{w}_k)\cdot\mathbf{n}_k dA = \overline{\mathbf{v}}_{kj}\Gamma_{kj}$	$\mathbf{M}_{kj}^{d} = \frac{1}{V_o}\int_{A_{kj}}\tau_k\cdot\mathbf{n}_k dA$ (see Section 5.2.4)
Energy	$Q_{kj} = Q_{kj}^{\Gamma} + Q_{kj}^{d}$	$Q_{kj}^{\Gamma} = -\frac{1}{V_o}\int_{A_{kj}}\rho_k h_k(\mathbf{v}_k - \mathbf{w}_k)\cdot\mathbf{n}_k dA = \overline{h}_{kj}\Gamma_{kj}$	$Q_{kj}^{d} = -\frac{1}{V_o}\int_{A_{kj}}\mathbf{q}_k\cdot\mathbf{n}_k dA$ (local thermal equlibrium)
Species	$J_{kj} = J_{kj}^{\Gamma} + J_{kj}^{d}$	$J_{kj}^{\Gamma} = -\frac{1}{V_o}\int_{A_{kj}}\rho_k C_k(\mathbf{v}_k - \mathbf{w}_k)\cdot\mathbf{n}_k dA = \overline{C}_{kj}\Gamma_{kj}$	$J_{kj}^{d} = -\frac{1}{V_o}\int_{A_{kj}}\mathbf{j}_k\cdot\mathbf{n}_k dA = \frac{S_{kj}\rho_k D_k}{l_{kj}}(\overline{C}_{kj} - \langle C_k\rangle^k)$

Table 2. Summary of the macroscopic conservation equations describing columnar solidification.

Mixture Mass Conservation

$$\frac{\partial}{\partial t}(\varepsilon_l\rho_l) + \nabla\cdot(\varepsilon_l\rho_l v_l) = -\frac{\partial}{\partial t}(\varepsilon_\alpha\rho_\alpha) - \frac{\partial}{\partial t}(\varepsilon_\gamma\rho_\gamma)$$

Liquid Species Conservation

$$\varepsilon_l\rho_l \frac{\partial C_l}{\partial t} + \varepsilon_l\rho_l\, v_l\cdot\nabla C_l = \nabla\cdot(\varepsilon_l\rho_l D_l \nabla C_l)$$
$$- \varepsilon_\alpha\rho_\alpha \frac{\partial C_\alpha}{\partial t} - \varepsilon_\gamma\rho_\gamma \frac{\partial C_\gamma}{\partial t}$$
$$+ [C_l - C_\alpha]\frac{\partial}{\partial t}(\varepsilon_\alpha\rho_\alpha) + [C_l - C_\gamma]\frac{\partial}{\partial t}(\varepsilon_\gamma\rho_\gamma)$$

Solid Species Conservation (s = α, γ)

$$\varepsilon_s\rho_s \frac{\partial C_s}{\partial t} = [\bar{C}_{sl} - C_s]\left\{\frac{\partial}{\partial t}(\varepsilon_s\rho_s) + S_s\frac{\rho_s D_s}{l_{sl}}\right\}$$

Mixture Energy Conservation

$$\varepsilon_l\rho_l \left.\frac{\partial h_l}{\partial T}\right|_{C_l}\frac{\partial T}{\partial t} + \varepsilon_l\rho_l \left.\frac{\partial h_l}{\partial T}\right|_{C_l} v_l\cdot\nabla T = \nabla\cdot\{(\varepsilon_l k_l + \varepsilon_s k_s)\nabla T\}$$
$$-\left[\varepsilon_\alpha\rho_\alpha \left.\frac{\partial h_\alpha}{\partial T}\right|_{C_\alpha} + \varepsilon_\gamma\rho_\gamma \left.\frac{\partial h_\gamma}{\partial T}\right|_{C_\gamma}\right]\frac{\partial T}{\partial t}$$
$$- \varepsilon_l\rho_l \left.\frac{\partial h_l}{\partial C_l}\right|_T \frac{\partial C_l}{\partial t} - \varepsilon_\alpha\rho_\alpha \left.\frac{\partial h_\alpha}{\partial C_\alpha}\right|_T \frac{\partial C_\alpha}{\partial t} - \varepsilon_\gamma\rho_\gamma \left.\frac{\partial h_\gamma}{\partial C_\gamma}\right|_T \frac{\partial C_\gamma}{\partial t}$$
$$+ \left.\frac{\partial h_l}{\partial C_l}\right|_T \left\{ \varepsilon_l\rho_l \frac{\partial C_l}{\partial t} + \varepsilon_\alpha\rho_\alpha \frac{\partial C_\alpha}{\partial t} + \varepsilon_\gamma\rho_\gamma \frac{\partial C_\gamma}{\partial t}\right.$$
$$\left. - [C_l - C_\alpha]\frac{\partial}{\partial t}(\varepsilon_\alpha\rho_\alpha) - [C_l - C_\gamma]\frac{\partial}{\partial t}(\varepsilon_\gamma\rho_\gamma)\right\}$$
$$+ [h_l - h_\alpha]\frac{\partial}{\partial t}(\varepsilon_\alpha\rho_\alpha) + [h_l - h_\gamma]\frac{\partial}{\partial t}(\varepsilon_\gamma\rho_\gamma)$$

Liquid Momentum Conservation

$$\varepsilon_l\rho_l \frac{\partial v_l}{\partial t} + \varepsilon_l\rho_l\, v_l\cdot\nabla v_l = -\varepsilon_l\nabla p_l + \nabla\cdot(\varepsilon_l\mu_l \nabla v_l)$$
$$+ \nabla\cdot\{\varepsilon_l\mu_l[\nabla v_l]^t + \mu_l[v_l\nabla\varepsilon_l + \nabla\varepsilon_l v_l]\}$$
$$+ v_l\left[\frac{\partial}{\partial t}(\varepsilon_\alpha\rho_\alpha) + \frac{\partial}{\partial t}(\varepsilon_\gamma\rho_\gamma)\right] - \varepsilon_l^2\mu_l\mathbf{K}^{(2)^{-1}}v_l + \varepsilon_l\rho_l g$$

Table 3. Summary of a multiphase model for equiaxed dendritic solidification

Mass Conservation

Solid Phase

$$\frac{\partial}{\partial t}(\rho_s \varepsilon_s) + \nabla\cdot(\rho_s \varepsilon_s \mathbf{v}_s) = \Gamma_s$$

Total Liquid Phase

$$\frac{\partial}{\partial t}(\rho_f \varepsilon_f) + \nabla\cdot(\rho_f \varepsilon_f \mathbf{v}_f) = -\Gamma_s$$

Interfacial Species Balance (for Calculating Phase Change Rate)

$$(\bar{C}_e - \bar{C}_{sd})\Gamma_s = \frac{\rho_s S_s D_s}{l_{sd}}(\bar{C}_{sd} - C_s) + \frac{\rho_l S_e D_l}{l_{ld}}(\bar{C}_e - C_l) +$$

$$[\rho_d \varepsilon_d \frac{\partial \bar{C}_e}{\partial t} + \rho_d \varepsilon_d \mathbf{v}_d \cdot \nabla \bar{C}_e - \nabla\cdot(\rho_d \varepsilon_d D_d^* \nabla \bar{C}_e)]$$

Momentum Conservation

Solid Phase

$$\frac{\partial}{\partial t}(\rho_s \varepsilon_s \mathbf{v}_s) + \nabla\cdot(\rho_s \varepsilon_s \mathbf{v}_s \mathbf{v}_s) = -\varepsilon_s \nabla p + \nabla\cdot(\mu_s^* \varepsilon_s \nabla \mathbf{v}_s) + \mathbf{M}_s^d + \rho_s \varepsilon_s \mathbf{g}$$

Total Liquid Phase

$$\frac{\partial}{\partial t}(\rho_f \varepsilon_f \mathbf{v}_f) + \nabla\cdot(\rho_f \varepsilon_f \mathbf{v}_f \mathbf{v}_f) = -\varepsilon_f \nabla p + \nabla\cdot(\mu_f^* \varepsilon_f \nabla \mathbf{v}_f) - \mathbf{M}_s^d + \varepsilon_f \rho_f \mathbf{g} + \nabla\cdot[\gamma \rho_f \varepsilon_f (\mathbf{v}_f - \mathbf{v}_s)(\mathbf{v}_f - \mathbf{v}_s)]$$

Species Conservation

Solid Phase

$$\frac{\partial}{\partial t}(\rho_s \varepsilon_s C_s) + \nabla\cdot(\rho_s \varepsilon_s \mathbf{v}_s C_s) = \nabla\cdot(\rho_s \varepsilon_s D_s^* \nabla C_s) + \bar{C}_{sd}\Gamma_s + \frac{\rho_s S_s D_s}{l_{sd}}(\bar{C}_{sd} - C_s)$$

Total Liquid Phase

$$\frac{\partial}{\partial t}(\rho_f \varepsilon_f C_f) + \nabla\cdot(\rho_f \varepsilon_f \mathbf{v}_f C_f) = \nabla\cdot(\rho_f \varepsilon_f D_f^* \nabla C_f) - [\bar{C}_{sd}\Gamma_s + \frac{\rho_s S_s D_s}{l_{sd}}(\bar{C}_{sd} - C_s)]$$

$$+ \nabla\cdot\{\rho_f \varepsilon_f (\mathbf{v}_f - \mathbf{v}_s)[C_f - \kappa_v C_d - (1-\kappa_v) C_l]\}$$

Mixture Energy Conservation

$$\frac{\partial}{\partial t}[(\rho_s \varepsilon_s c_s + \rho_f \varepsilon_f c_f)T] + \nabla\cdot[(\rho_s \varepsilon_s c_s \mathbf{v}_s + \rho_f \varepsilon_f c_f \mathbf{v}_f)T] =$$

$$\nabla\cdot[(\varepsilon_s k_s^* + \varepsilon_f k_f^*)\nabla T] + \Gamma_s[\Delta h + (c_s - c_l)T_E]$$

Auxiliary Relations for Secondary Variables

Interdendritic Liquid Fraction

$$\frac{\partial}{\partial t}(\rho_d \varepsilon_d) + \nabla\cdot(\rho_d \varepsilon_d \mathbf{v}_d) = S_e \rho_l \bar{w}_{ne} - \Gamma_s$$

Extradendritic Liquid Fraction

$$\varepsilon_l = \varepsilon_f - \varepsilon_d$$

Extradendritic Liquid Concentration

$$C_l = (\rho_f \varepsilon_f C_f - \rho_d \varepsilon_d \bar{C}_e)/(\rho_l \varepsilon_l)$$

Inter- and Extra-dendritic Liquid Velocities

$$\mathbf{v}_d = \mathbf{v}_s + \kappa_v \frac{\rho_f \varepsilon_f}{\rho_d \varepsilon_d}(\mathbf{v}_f - \mathbf{v}_s) \; ; \quad \mathbf{v}_l = \mathbf{v}_s + (1-\kappa_v)\frac{\rho_f \varepsilon_f}{\rho_l \varepsilon_l}(\mathbf{v}_f - \mathbf{v}_s)$$

LIST OF FIGURES

Fig.12 Schematic of shape factors for (a) an equiaxed dendrite envelope, and (b) a square arrangement of columnar dendrite envelopes.

Fig.13 Equivalent sphere model for species diffusion in the extradendritic liquid: (a) geometry, and (b) concentration profile.

Fig.14 Microsegregation of P in δ-Fe, as predicted by various solute diffusion models [40].

Fig.15 Effect of dendrite tip undercooling on the temperature *vs* solid fraction relation for columnar solidification of an Al-4.5wt% Cu alloy [40].

Fig.16 Comparisons of the present prediction of microsegregation in a rapidly solidified Ag-15wt% Cu alloy with the Giovanola and Kurz's calculation [37] and the experimental data by Bendersky and Boettinger [73] (from [40]).

Fig.17 Effect of cooling rate on the eutectic fraction. Comparison of the present predictions with Sarreal and Abbaschian's experiments [74] (from [40]).

Fig.18 Comparisons of cooling curves for equiaxed dendritic growth, as predicted by the present model (solid lines) and Rappaz and Thevoz [34] (dashed lines) for final grain radii of (A) 100μm, (B) 1 mm and (C) 10 mm [40].

Fig.19 Schematic of the physical problem and illustration of the multiphase approach used in the CET simulations.

Fig.20 (a) Cooling curves and (b) solid and grain volume fraction evolutions for a 1-D casting of an Al-3wt% Cu alloy ($h=65$ W/m^{2}K, $n=10^5$ m^{-3} and $\Delta T_0=20$ K). The curves from left to right correspond to five locations between $x/L = 0.025$ and 0.825 with an interval of 0.2 [24].

Fig.21 Map of different regions developing in a 1-D casting of an Al-3wt% Cu alloy ($h=65$ W/m^{2}K, $n=10^5$ m^{-3} and $\Delta T_0=20$ K) [24].

Fig.22 Evolution of the interface between the columnar and equiaxed zones in (a) 100×100mm square and (b) 50×100mm rectangular castings of an Al-3wt% Cu alloy ($h=65$ W/m^{2}K, $n=10^5$ m^{-3} and $\Delta T_0=20$ K). The dashed line denotes the final CET position [24].

Fig.23 Effects of nuclei density and chill heat transfer coefficient on the CET position in a 1-D casting of an Al-3wt% Cu alloy. Comparison with Ziv and Weinberg's data [25] (from [24]).

Fig.24 Comparison of the predicted CET positions with all experimental data reported in [82,25] (Sn-Pb alloys: $n=10^7$ m^{-3}, Al-3wt% Cu alloy: $n=10^5$ m^{-3}) [24].

Fig.25 (a) Schematic illustration of the domain and boundary conditions used by Schneider and Beckermann [93] to simulate the solidification of a Pb-20 wt% Sn alloy. (b) A typical averaging volume that includes α-phase solid, eutectic ($\alpha + \gamma$) solid, and liquid. (c) Schematic illustration of the assumed microscopic temperature and concentration profiles for the case of complete microscopic solid species diffusion. (d) Schematic illustration of the assumed microscopic temperature and concentration profiles for the case of no microscopic solid species diffusion.

Fig.26 Final macrosegregation and eutectic fraction patterns for the solidification of Pb-20 wt.% Sn alloy [93]: (a) Macrosegregation with no microscopic solid species diffusion. (b) Macrosegregation with complete microscopic solid species diffusion. (c) Eutectic fraction with no microscopic solid species diffusion. (d) Eutectic fraction with complete microscopic solid species diffusion.

Fig.27 Variation of the permeabilities perpendicular, $K_{\eta\eta}$, and parallel, $K_{\xi\xi}$, to the primary dendrite arms for typical primary, d_1, and secondary, d_2, dendrite arm spacings, as well as for an approximate isotropic permeability. Also shown is the variation of the ratio of the perpendicular and parallel permeabilities with the liquid fraction.

Fig.28 Velocity field, solid fraction isopleths and macrosegregation distributions after 250 seconds for the solidification of a Pb-20 wt% Sn alloy [93]: (a) Velocity field and solid fraction distritution using an anisotropic permeability model. (b) Velocity field and solid fraction distritution using an isotropic permeability model. (c) Macrosegregation pattern using an anisotropic permeability model. (d) Macrosegregation pattern using an isotropic permeability model.

Fig.29 Velocity field and solid fraction isopleths near the end of solidification of a Pb-20 wt% Sn alloy [93]: (a) after 800 s assuming no microscopic solid species diffusion. (b) after 2050 s assuming complete microscopic solid species diffusion.

Fig.30 Macrosegregation profiles for the unidirectional solidification of a Pb-20 wt% Sn alloy with no buoyancy driven flow: (a) near the chill and (b) throughout the casting [93].

Fig.31 Schematic of the partitioning of the liquid flow through the interdendritic and extradendritic regions in equiaxed solidification.

Fig.32 Flow partition coefficient as functions of the extradendritic liquid fraction and internal solid fraction for S_s/S_e=0.1 [126].

Fig.33 Schematic of the physical system used in the simulation of equiaxed dendritic solidification with convection.

Fig.34 Results for equiaxed dendritic solidification of an Al-4wt% Cu alloy (n_o=10^9 m^{-3}) at t=50 s: (a) solid fraction and liquid velocity vectors; (b) mixture concentration; (c) isotherms, and (d) relative velocity vectors (v_f - v_s) [41].

Fig.35 Evolution of the grain density for equiaxed dendritic solidification of an Al-4wt% Cu alloy (n_o=10^9 m^{-3}): (a) t=10 s; (b) t=30 s; (c) t=50 s; (d) t=100 s, and (e) final [41].

Fig.36 Predicted final grain size (R_e) distribution for (a) n_o=10^9 m^{-3}, and (b) n_o=10^{11} m^{-3} [41].

Fig.37 Final Macrosegregation patterns for: (a) a stationary solid (n_o=10^9 m^{-3}), (b) moving solid (n_o=10^9 m^{-3}), and (c) moving solid (n_o=10^{11} m^{-3}) [41].

Fig.38 Comparison of predictions with NH_4Cl-H_2O experiments: (a) schematic of the test cell, (b) shadowgraph image at t=13.5 min, and (c) predicted solid fraction image (white for ε_s<0.1%; black for ε_s>1%, and continuous gray scale for 0.1%<ε_s<1%) and liquid velocity vectors ($|v|_{max}$=1.7 cm/s) at t=13.5 min [136].

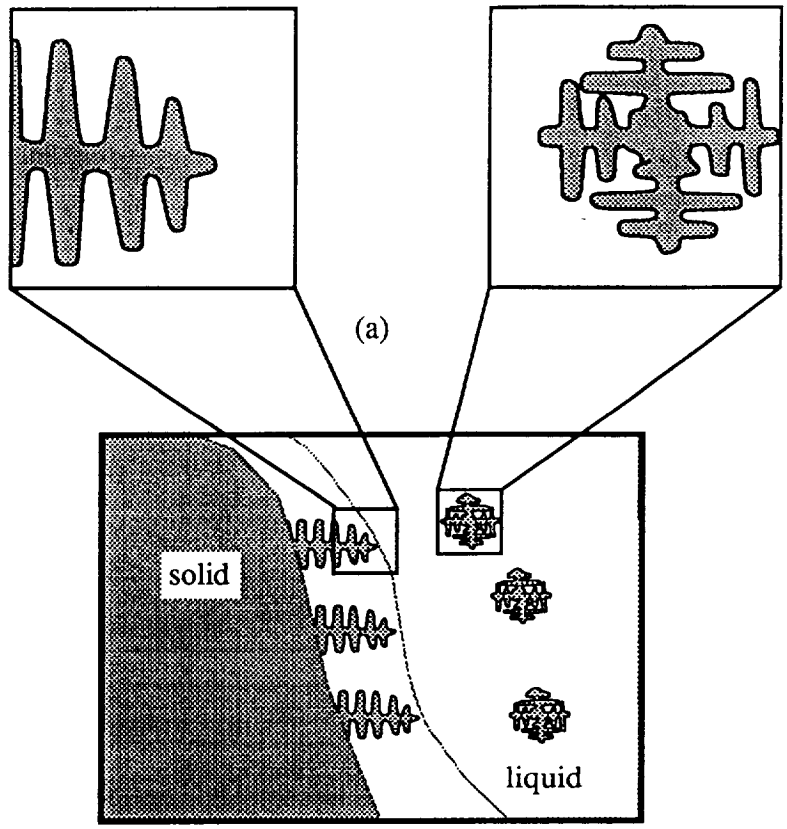
(a)
solid
liquid
(b)
$\kappa = C_{li}/C_{si}$
liquid
liquidus ($\kappa<1$)
solidus
T_i
T_E
Temperature
α
solid
α + liquid
liquidus ($\kappa>1$)
γ + liquid
C_E
α + γ
solid
γ solid
C_{si}
C_{li}
Concentration
(c)

Fig. 1

(a)

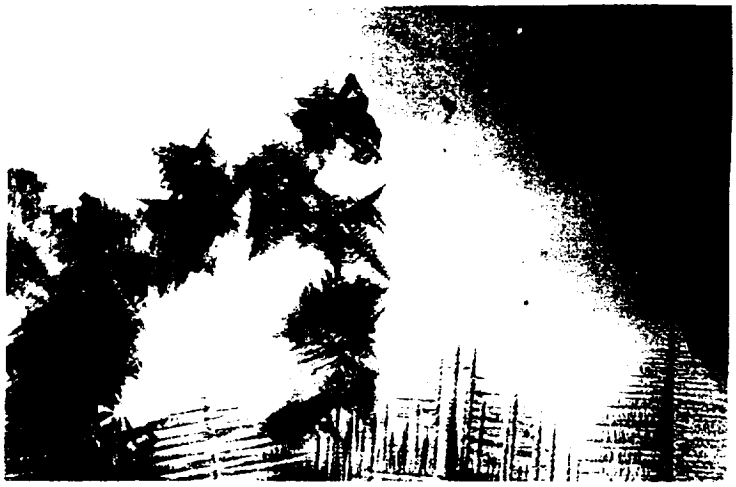

(b)

Fig. 2

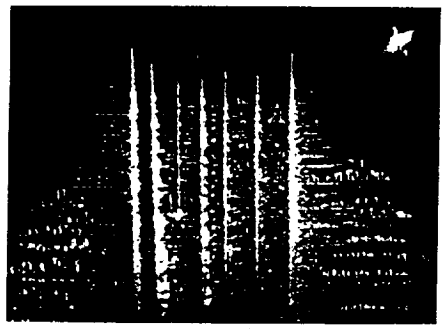

(a)

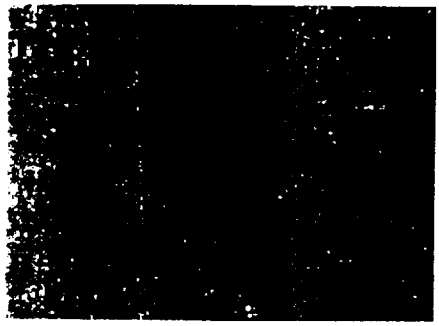

(b)

Fig. 3

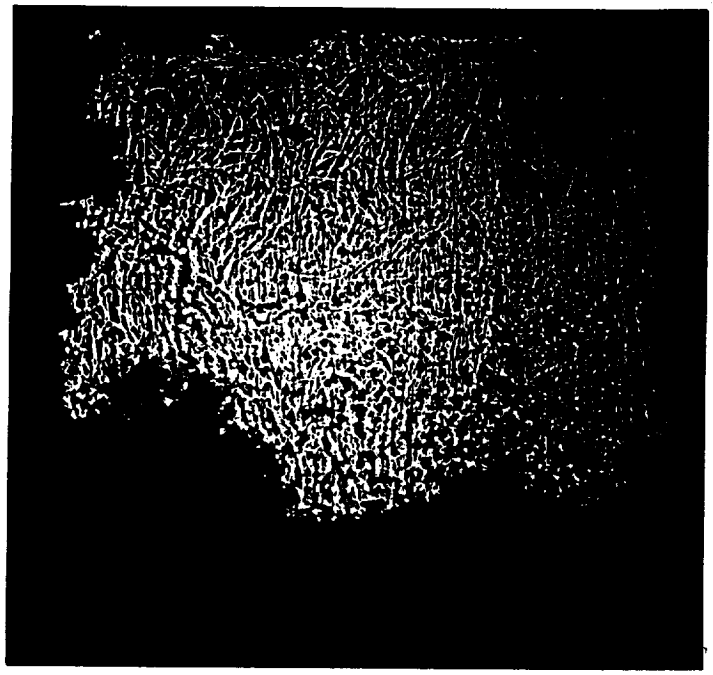

(a)

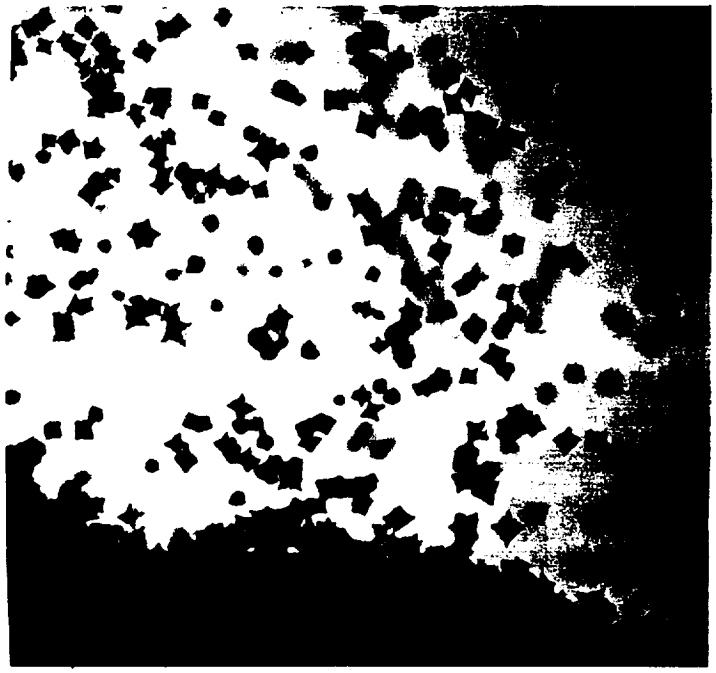

(b)

Fig. 4

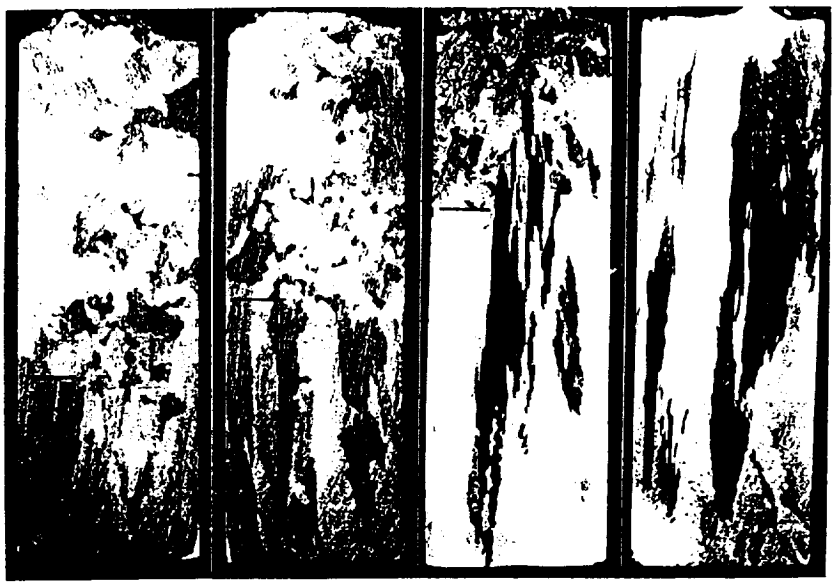

(a)

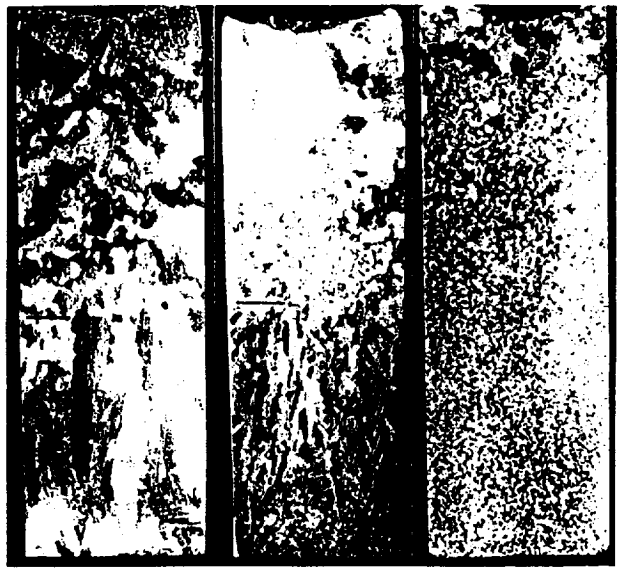

(b)

Fig. 5

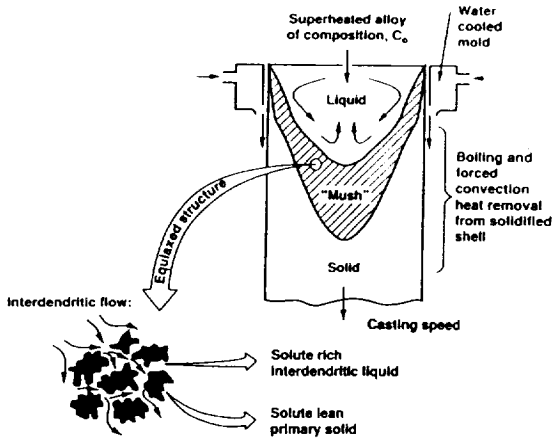

(a)

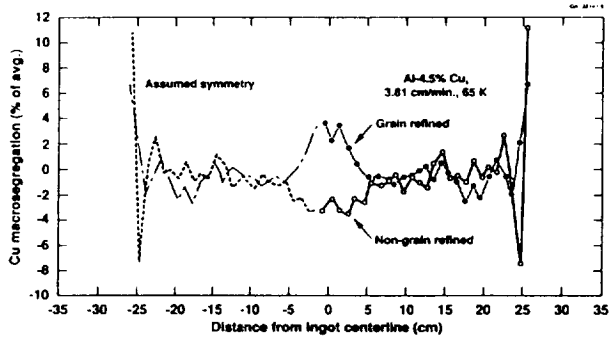

(b)

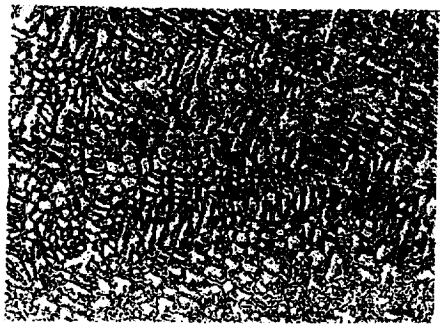

(c) 200 µm

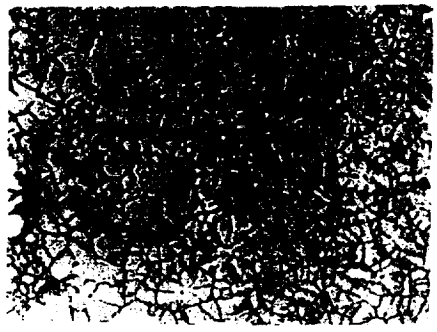

(d) 200 µm

Fig. 6

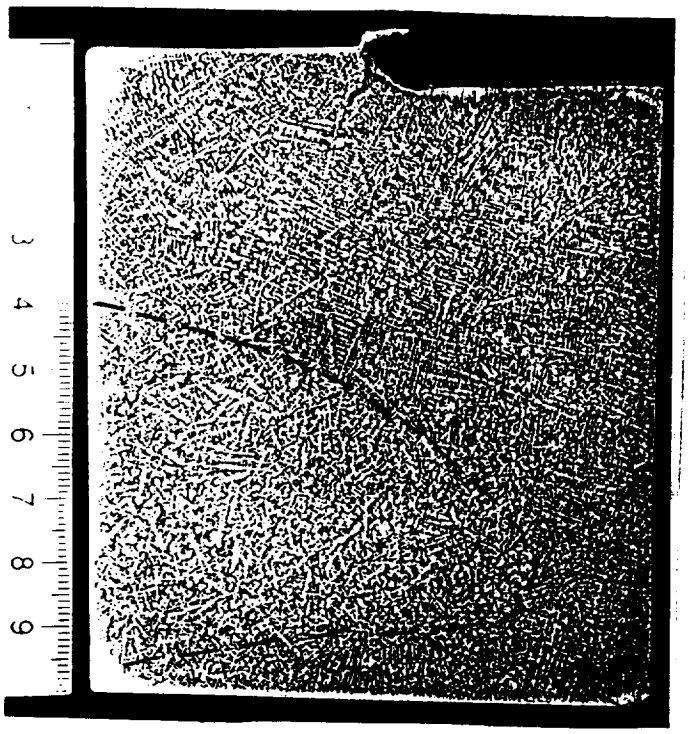

(a)

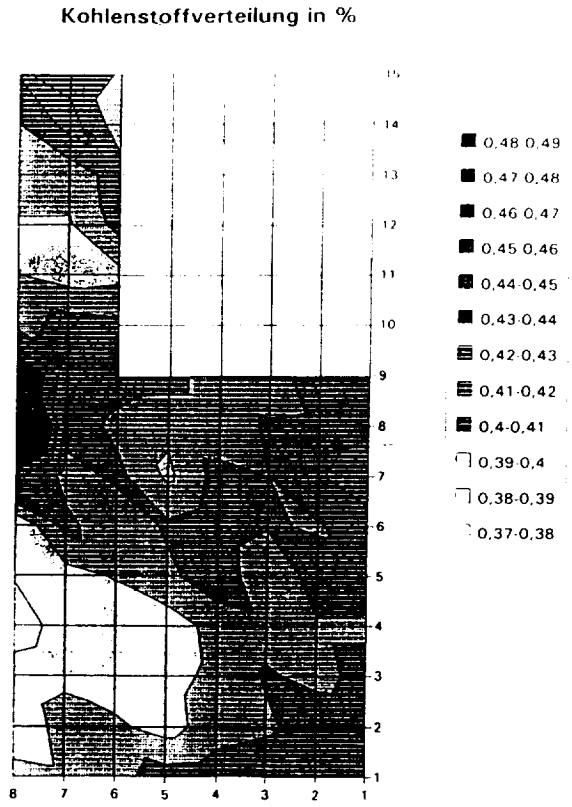
Kohlenstoffverteilung in %
0,48 0,49
0,47 0,48
0,46 0,47
0,45 0,46
0,44-0,45
0,43-0,44
0,42-0,43
0,41-0,42
0,4-0,41
0,39-0,4
0,38-0,39
0,37-0,38

(b)

Fig. 7

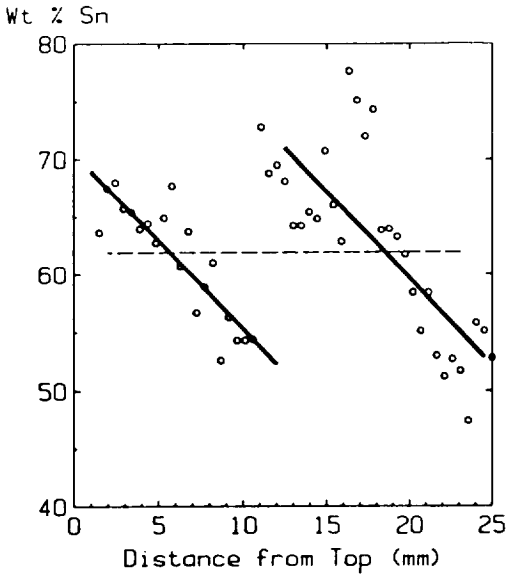
Wt % Sn
80
70
60
50
40
0
5
10
15
20
25
Distance from Top (mm)

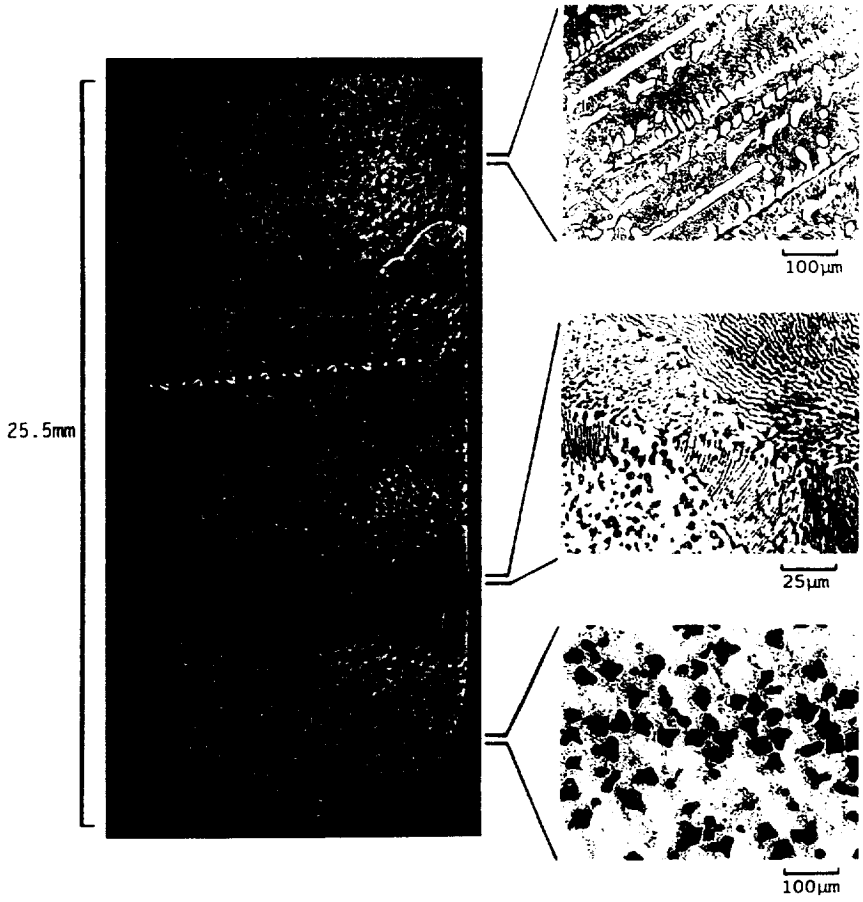
25.5mm
100μm
25μm
100μm

Fig. 8

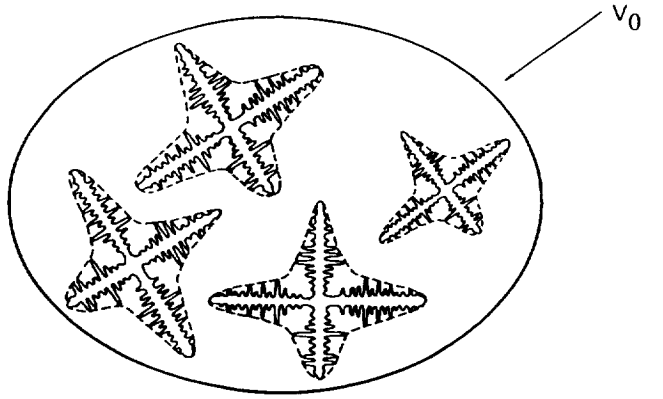

(a)

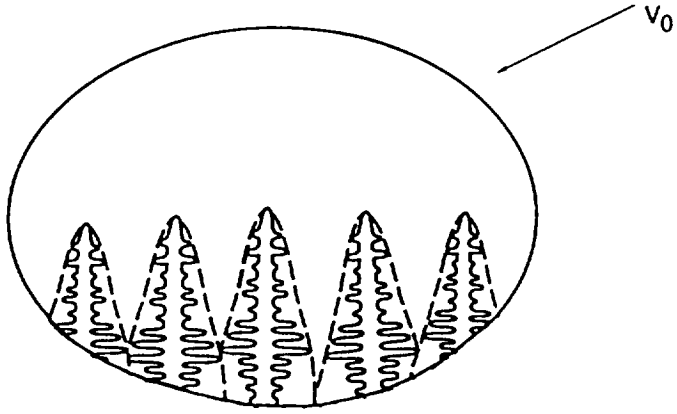

(b)

Fig. 9

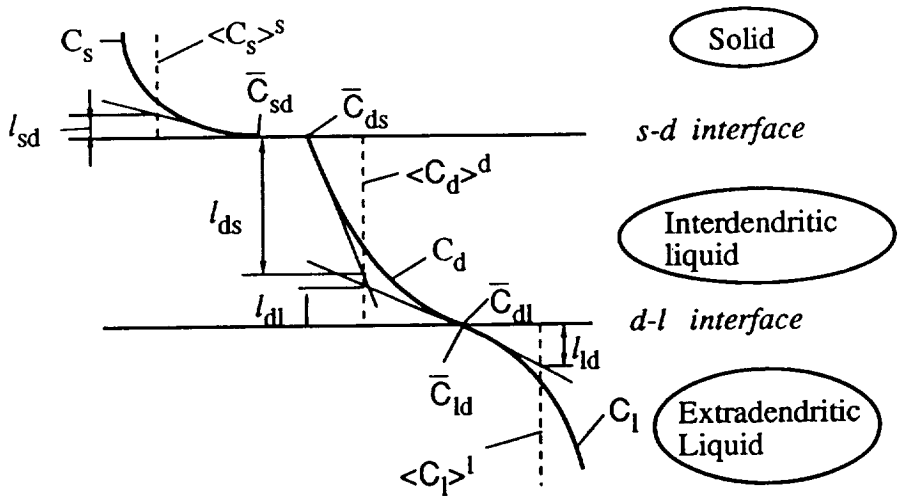
C_s
$\langle C_s \rangle^s$
$\bar{C}_{sd}$
$\bar{C}_{ds}$
l_{sd}
Solid
s-d interface
$\langle C_d \rangle^d$
l_{ds}
Interdendritic liquid
C_d
$\bar{C}_{dl}$
l_{dl}
d-l interface
l_{ld}
$\bar{C}_{ld}$
C_l
Extradendritic Liquid
$\langle C_l \rangle^l$

Fig. 10

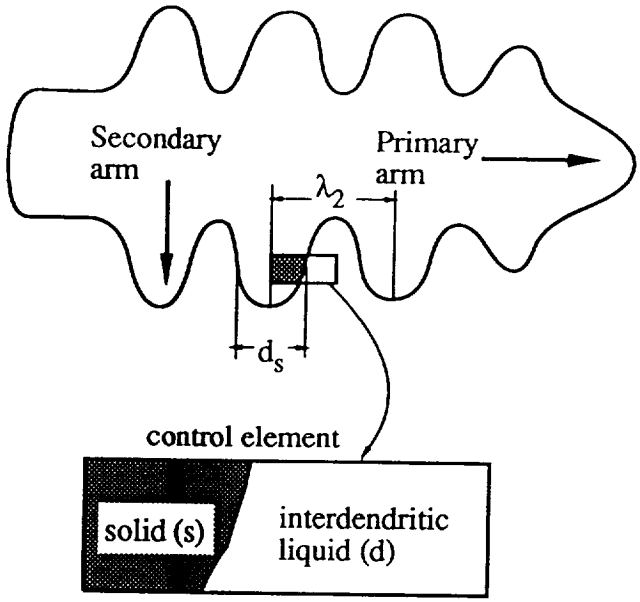
Secondary arm
Primary arm
λ_2
d_s
control element
solid (s)
interdendritic liquid (d)

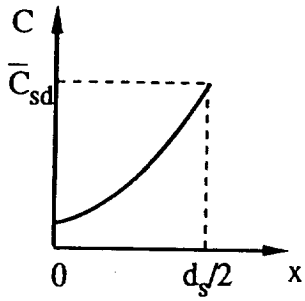
C
$\bar{C}_{sd}$
0
$d_s/2$
x

Fig. 11

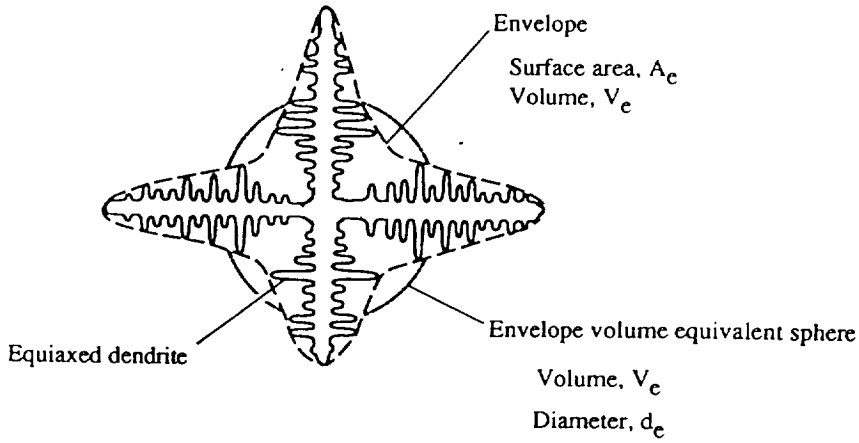

Shape factor : $\phi_e = \frac{\pi}{4} d_e^2 / A_e$

(a)

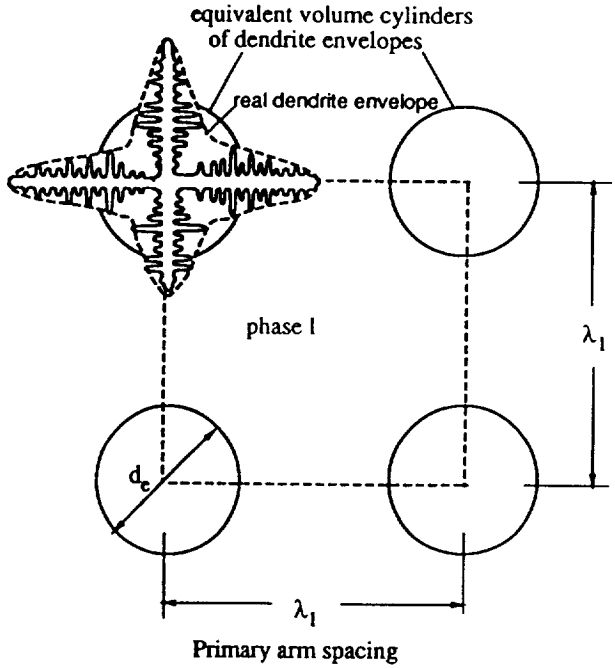

Primary arm spacing

(b)

Fig. 12

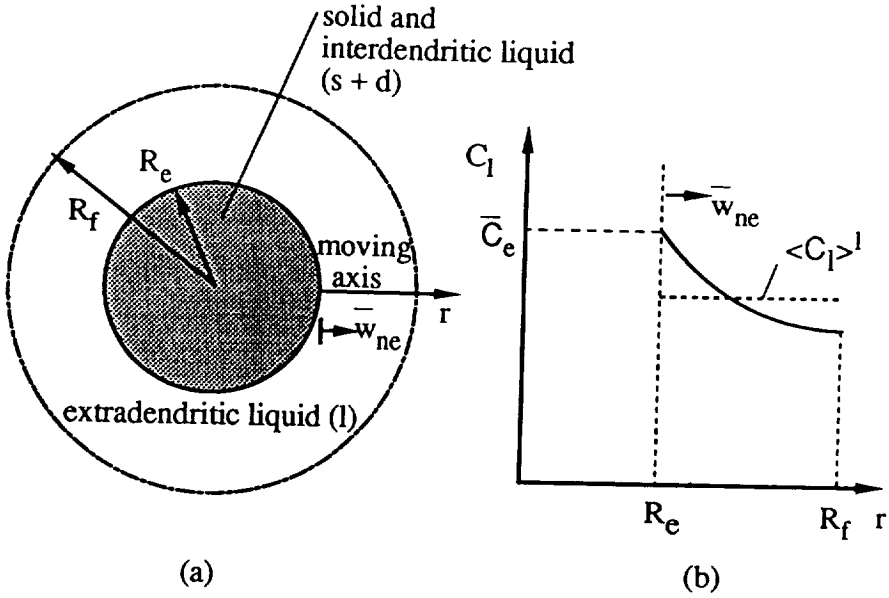
solid and
interdendritic liquid
(s + d)
R_e
R_f
moving
axis
r
$\bar{w}_{ne}$
extradendritic liquid (l)
C_l
$\bar{C}_e$
$\bar{w}_{ne}$
$<C_l>^l$
R_e
R_f r

(a) (b)

Fig. 13

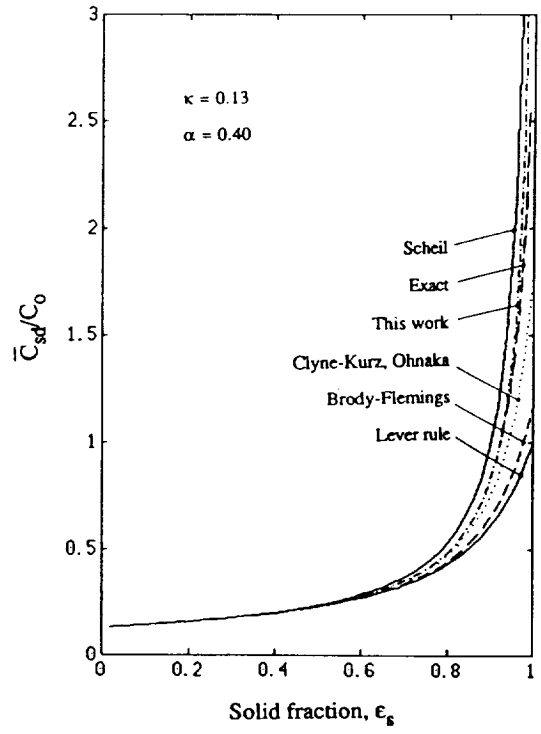
κ = 0.13
α = 0.40
Scheil
Exact
This work
Clyne-Kurz, Ohnaka
Brody-Flemings
Lever rule
$\bar{C}_{sd}/C_o$
Solid fraction, ϵ_s
0
0.5
1
1.5
2
2.5
3
0.2
0.4
0.6
0.8

Fig. 14

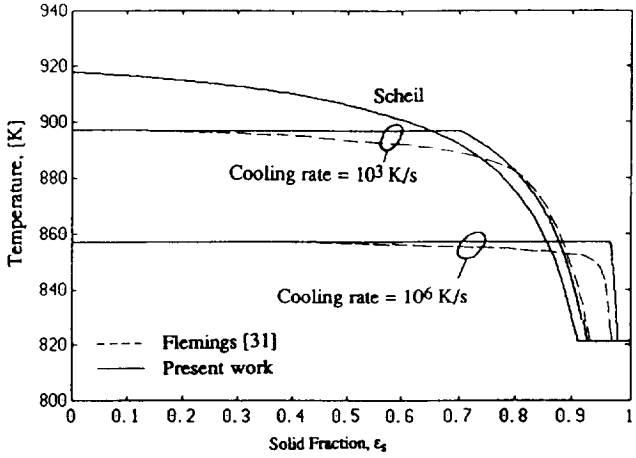
940
920
900
880
860
840
820
800
Temperature, [K]
0
0.1
0.2
0.3
0.4
0.5
0.6
0.7
0.8
0.9
1
Solid Fraction, ε_s
Scheil
Cooling rate = 10^3 K/s
Cooling rate = 10^6 K/s
Flemings [31]
Present work

Fig. 15

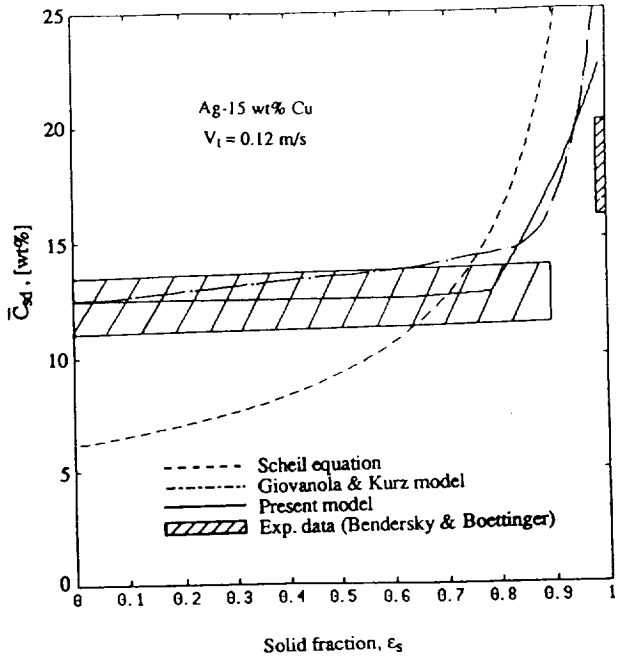
Ag-15 wt% Cu
V_t = 0.12 m/s
$\bar{C}_{sd}$, [wt%]
Scheil equation
Giovanola & Kurz model
Present model
Exp. data (Bendersky & Boettinger)
Solid fraction, ε_s

Fig. 16

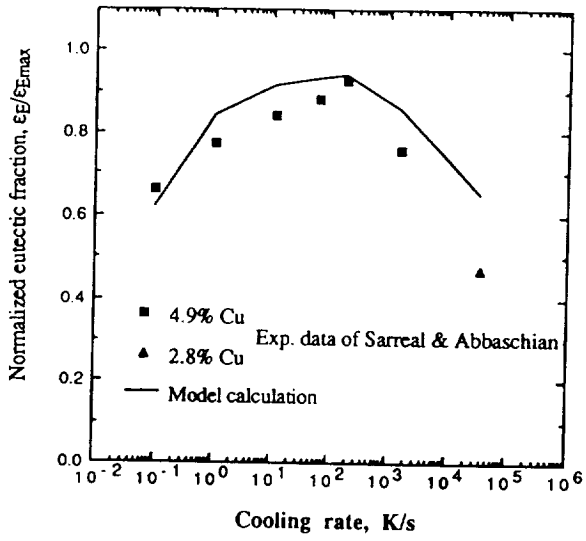
Normalized eutectic fraction, εE/εEmax
1.0
0.8
0.6
0.4
0.2
0.0
10-2 10-1 100 101 102 103 104 105 106
Cooling rate, K/s
4.9% Cu
2.8% Cu
Exp. data of Sarreal & Abbaschian
Model calculation

Fig. 17

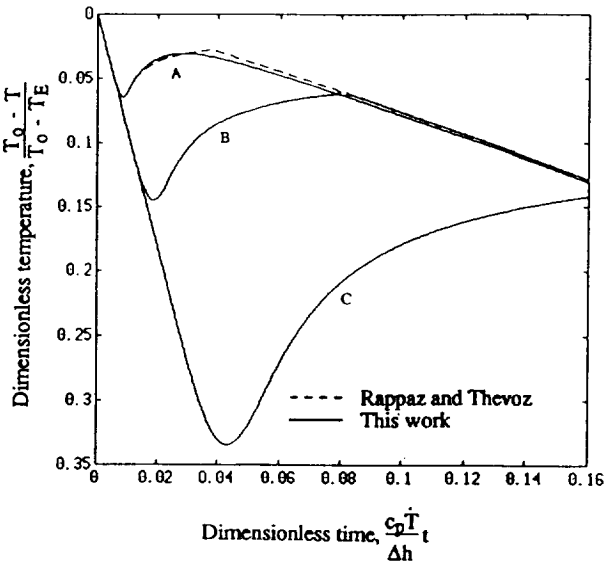
Dimensionless temperature, $\frac{T_0 - T}{T_0 - T_E}$
Dimensionless time, $\frac{c_p \dot{T}}{\Delta h} t$
0
0.05
0.1
0.15
0.2
0.25
0.3
0.35
0
0.02
0.04
0.06
0.08
0.1
0.12
0.14
0.16
A
B
C
Rappaz and Thevoz
This work

Fig. 18

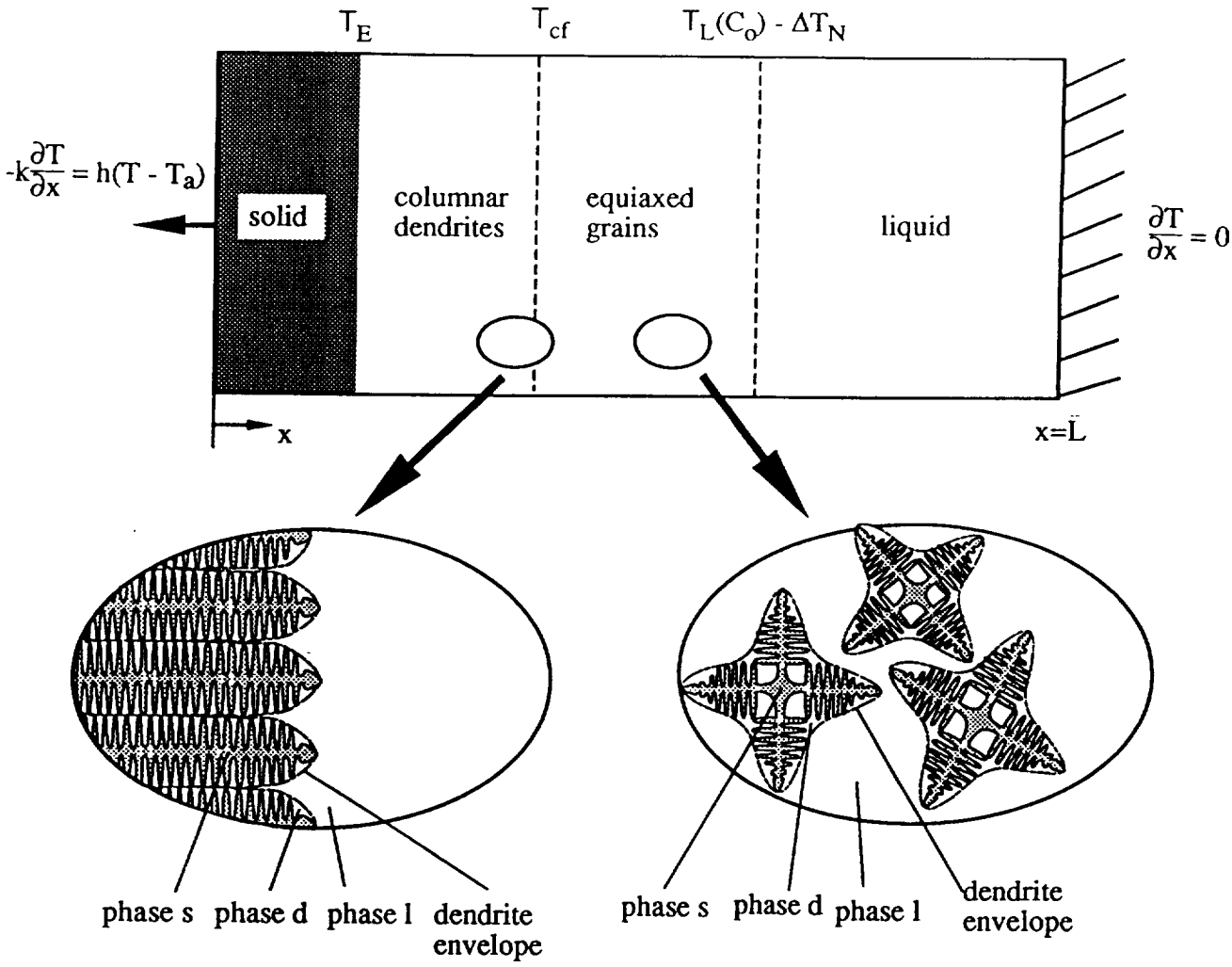
T_E
T_{cf}
$T_L(C_o) - \Delta T_N$
$-k\frac{\partial T}{\partial x} = h(T - T_a)$
solid
columnar dendrites
equiaxed grains
liquid
$\frac{\partial T}{\partial x} = 0$
x
x=L
phase s
phase d
phase l
dendrite envelope
phase s
phase d
phase l
dendrite envelope

Fig. 19

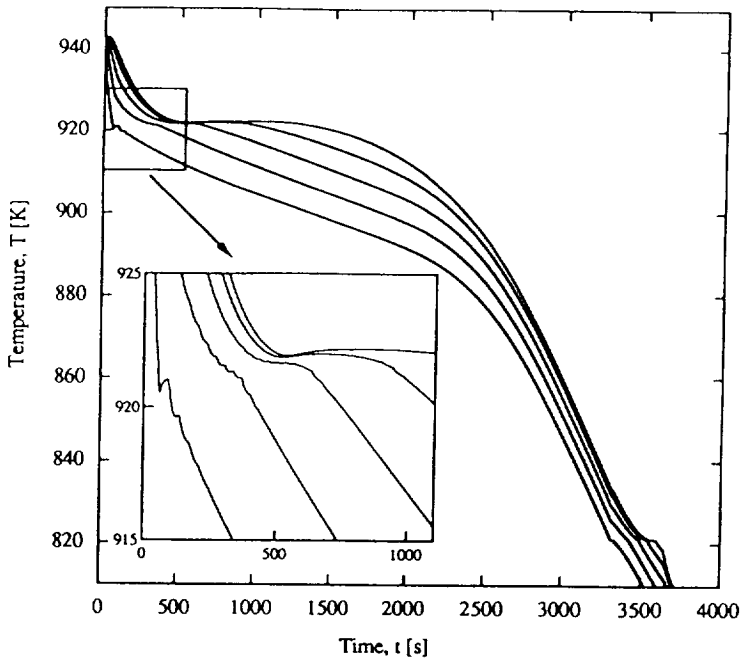
Temperature, T [K]
940
920
900
880
860
840
820
925
920
915
0
500
1000
0
500
1000
1500
2000
2500
3000
3500
4000
Time, t [s]

(a)

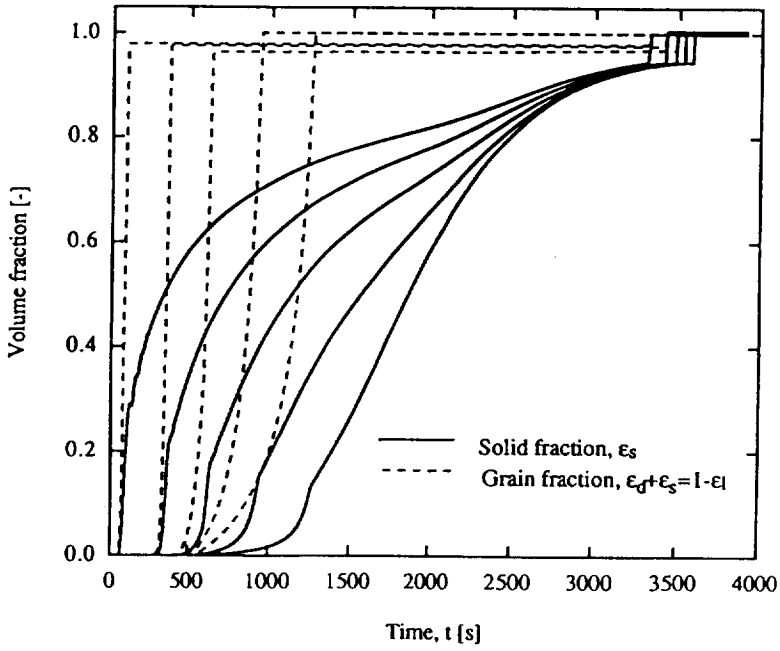
Volume fraction [-]
1.0
0.8
0.6
0.4
0.2
0.0
Solid fraction, ϵ_s
Grain fraction, $\epsilon_d+\epsilon_s=1-\epsilon_l$
0
500
1000
1500
2000
2500
3000
3500
4000
Time, t [s]

(b)

Fig. 20

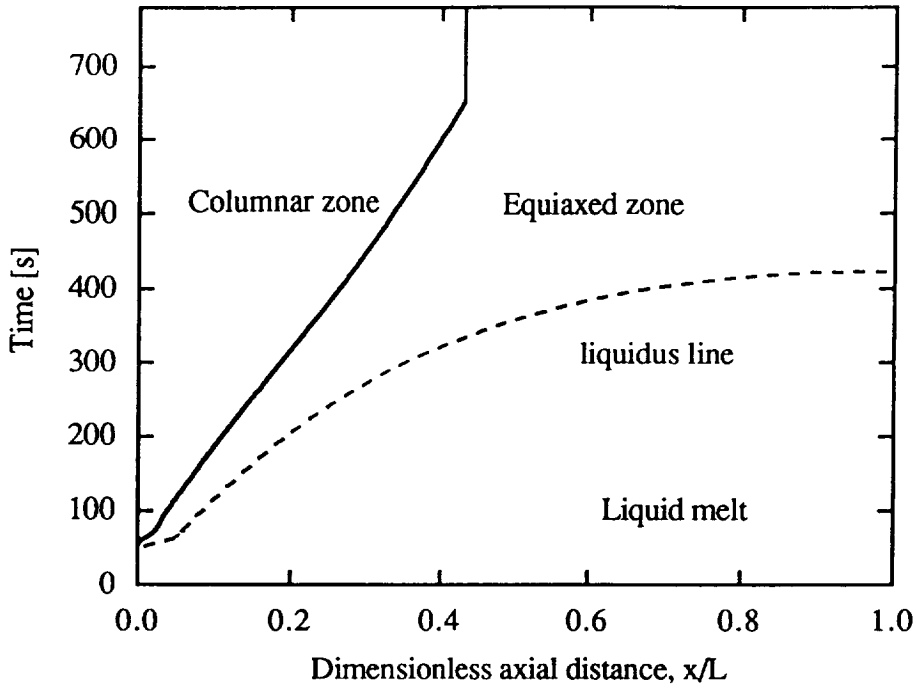
700
600
500
400
300
200
100
0
Time [s]
Columnar zone
Equiaxed zone
liquidus line
Liquid melt
0.0
0.2
0.4
0.6
0.8
1.0
Dimensionless axial distance, x/L

Fig. 21

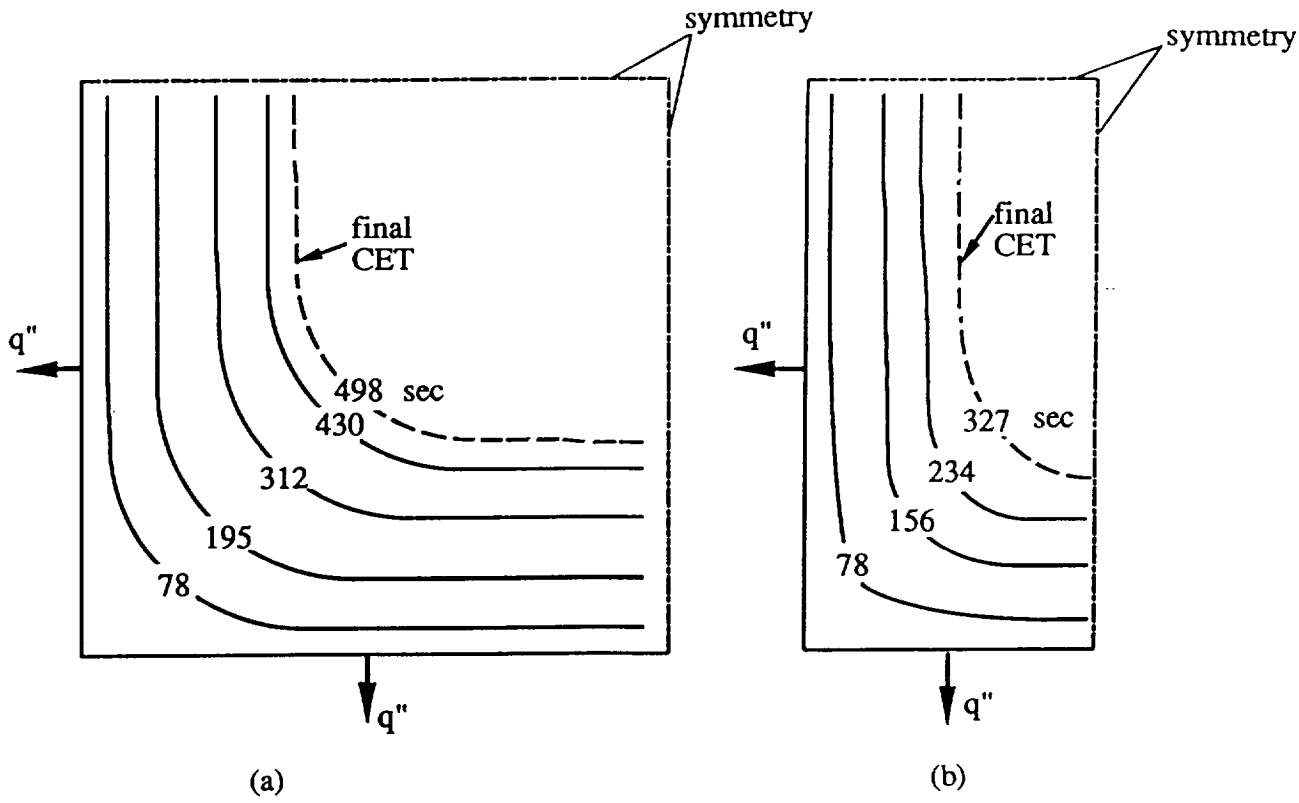
symmetry
final
CET
q"
498 sec
430
312
195
78
q"
(a)
symmetry
final
CET
q"
327 sec
234
156
78
q"
(b)

Fig. 22

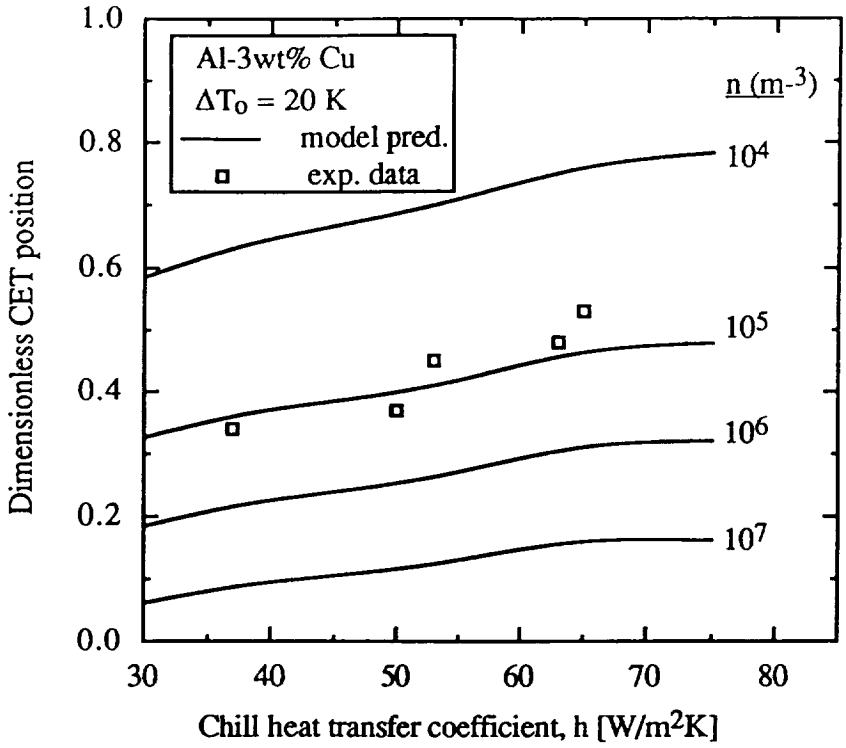
Al-3wt% Cu
ΔT₀ = 20 K
model pred.
exp. data
n (m⁻³)
10⁴
10⁵
10⁶
10⁷
Dimensionless CET position
Chill heat transfer coefficient, h [W/m²K]
1.0
0.8
0.6
0.4
0.2
0.0
30
40
50
60
70
80

Fig. 23

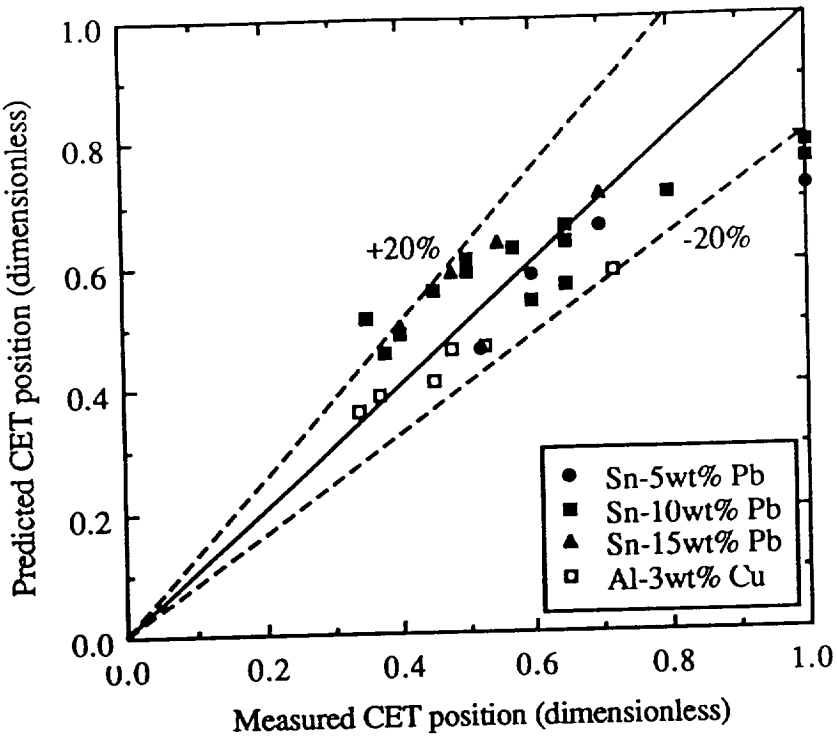
Predicted CET position (dimensionless)
Measured CET position (dimensionless)
1.0
0.8
0.6
0.4
0.2
0.0
0.0
0.2
0.4
0.6
0.8
1.0
+20%
-20%
Sn-5wt% Pb
Sn-10wt% Pb
Sn-15wt% Pb
Al-3wt% Cu

Fig. 24

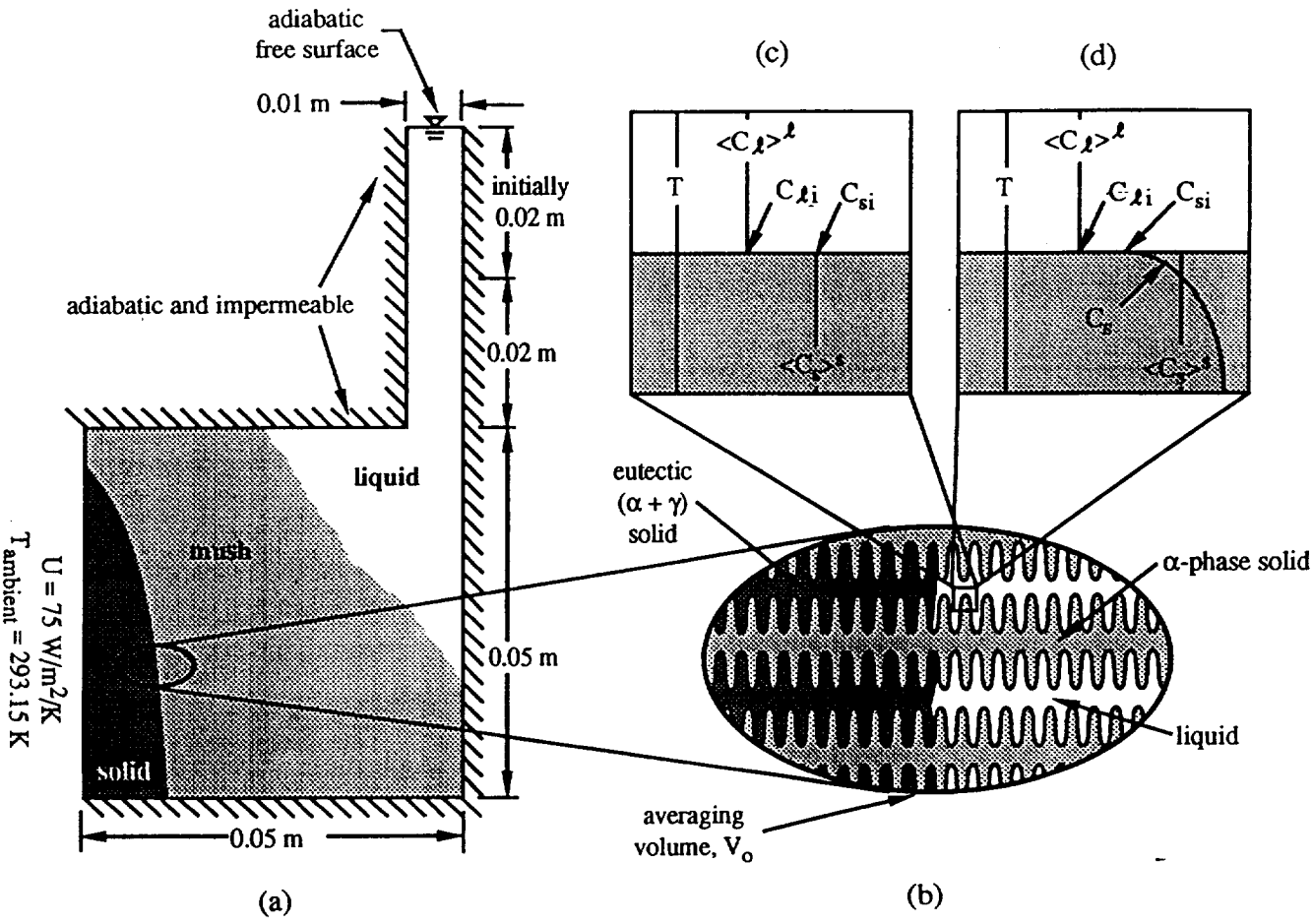
adiabatic
free surface
0.01 m
initially
0.02 m
0.02 m
adiabatic and impermeable
liquid
mush
solid
0.05 m
0.05 m
U = 75 W/m²/K
T ambient = 293.15 K
(a)
(c)
(d)
T
C_ℓi
C_si
C_s
eutectic
(α + γ)
solid
α-phase solid
liquid
averaging
volume, V_o
(b)

Fig. 25

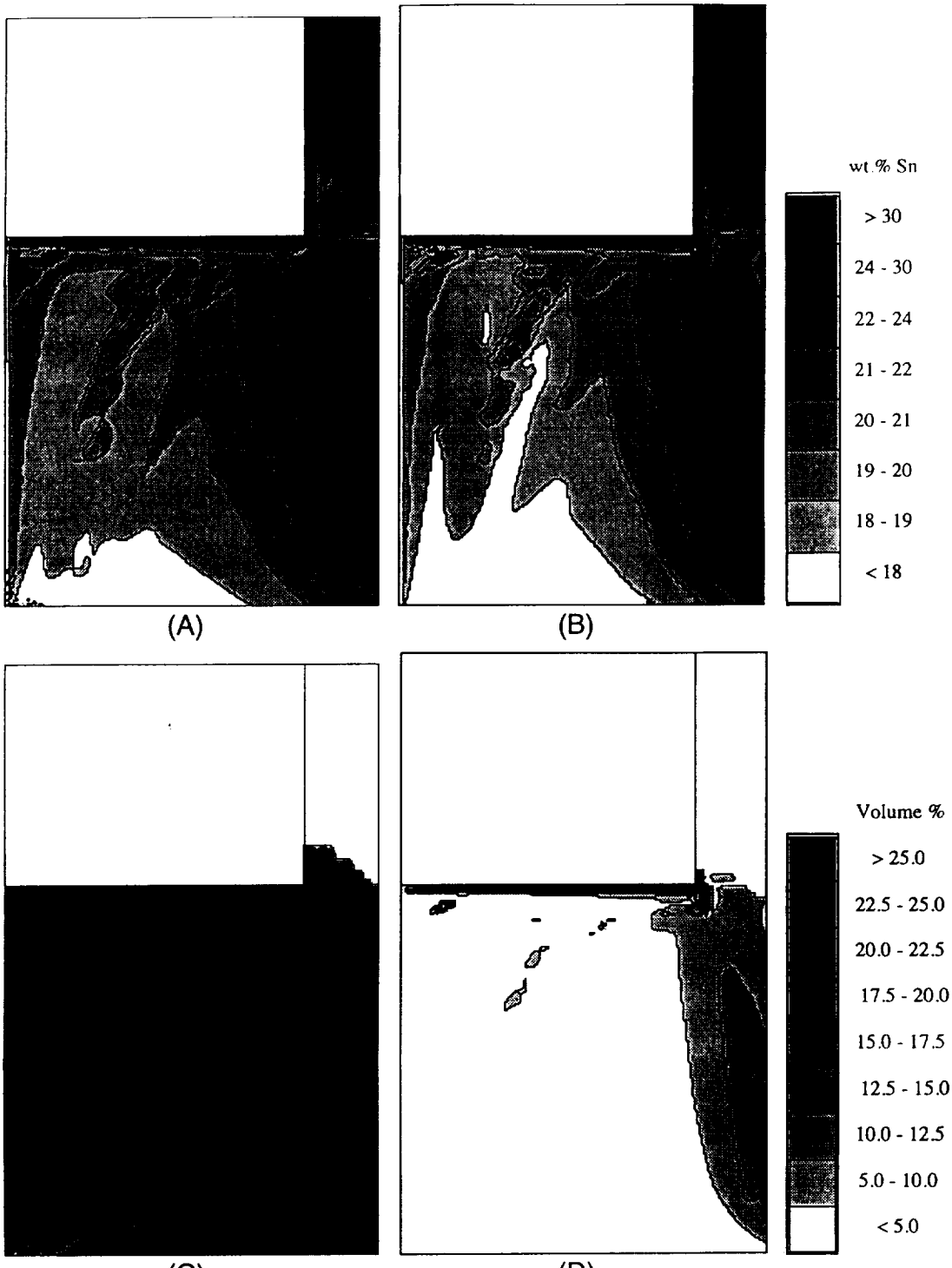
wt.% Sn
> 30
24 - 30
22 - 24
21 - 22
20 - 21
19 - 20
18 - 19
< 18
(A)
(B)
Volume %
> 25.0
22.5 - 25.0
20.0 - 22.5
17.5 - 20.0
15.0 - 17.5
12.5 - 15.0
10.0 - 12.5
5.0 - 10.0
< 5.0
(C)
(D)

Fig. 26

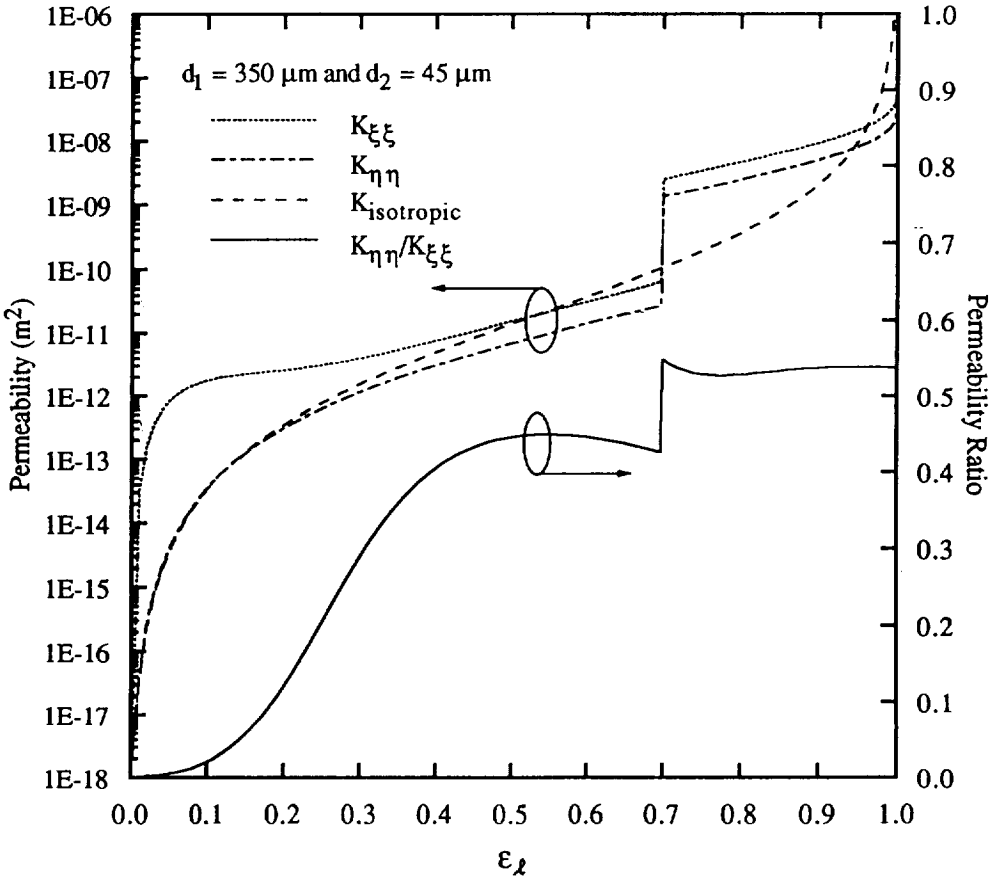
d_1 = 350 μm and d_2 = 45 μm
$K_{\xi\xi}$
$K_{\eta\eta}$
$K_{isotropic}$
$K_{\eta\eta}/K_{\xi\xi}$
Permeability (m^2)
Permeability Ratio
1E-06
1E-07
1E-08
1E-09
1E-10
1E-11
1E-12
1E-13
1E-14
1E-15
1E-16
1E-17
1E-18
1.0
0.9
0.8
0.7
0.6
0.5
0.4
0.3
0.2
0.1
0.0
0.0 0.1 0.2 0.3 0.4 0.5 0.6 0.7 0.8 0.9 1.0
ε_ℓ

Fig. 27

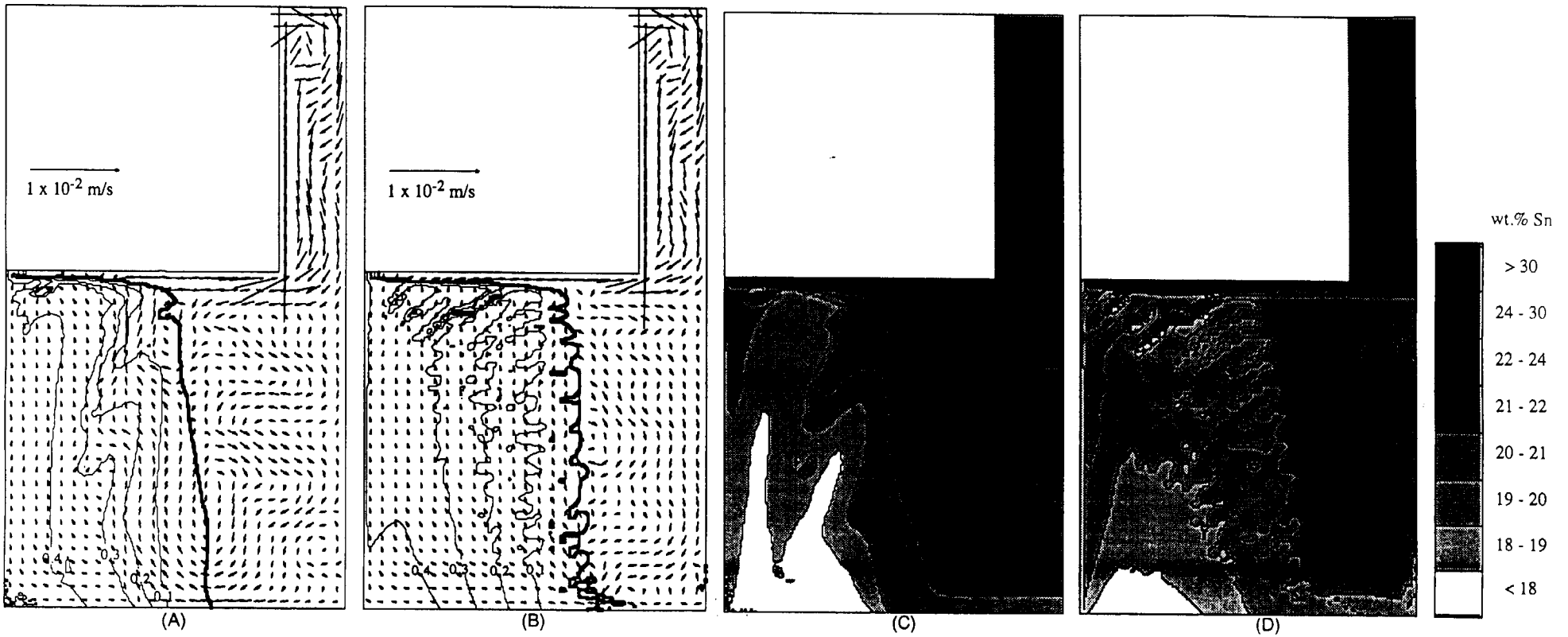
1 x 10-2 m/s
1 x 10-2 m/s
(A)
(B)
(C)
(D)
wt.% Sn
> 30
24 - 30
22 - 24
21 - 22
20 - 21
19 - 20
18 - 19
< 18

Fig. 28

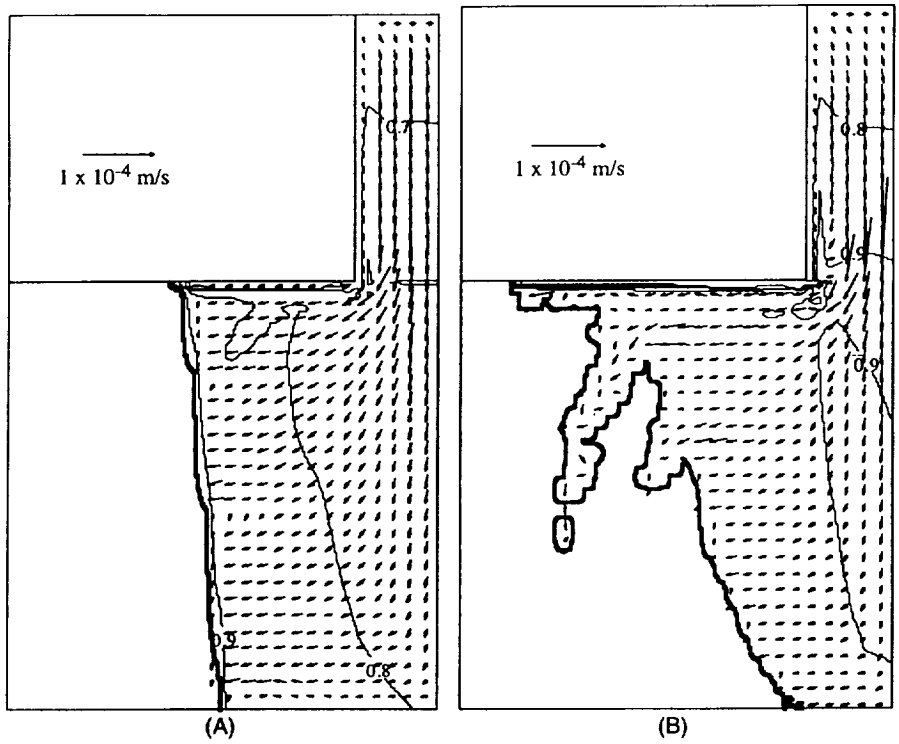

Fig. 29

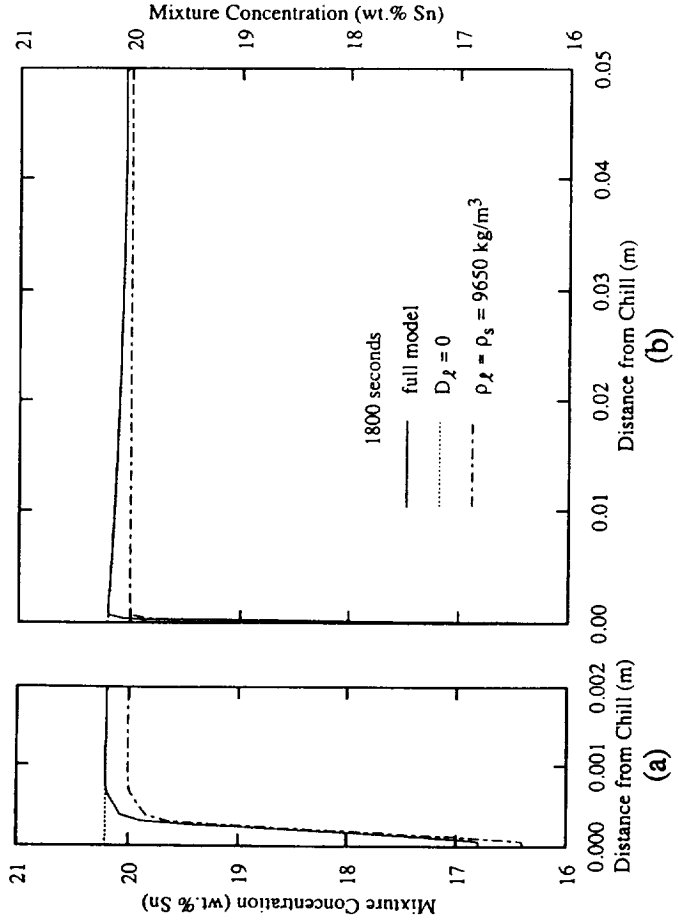
Mixture Concentration (wt.% Sn)
21
20
19
18
17
16
0.00
0.01
0.02
0.03
0.04
0.05
Distance from Chill (m)
(b)
1800 seconds
full model
$D_\ell = 0$
$\rho_\ell = \rho_s = 9650\ kg/m^3$
Mixture Concentration (wt.% Sn)
21
20
19
18
17
16
0.000
0.001
0.002
Distance from Chill (m)
(a)

Fig. 30

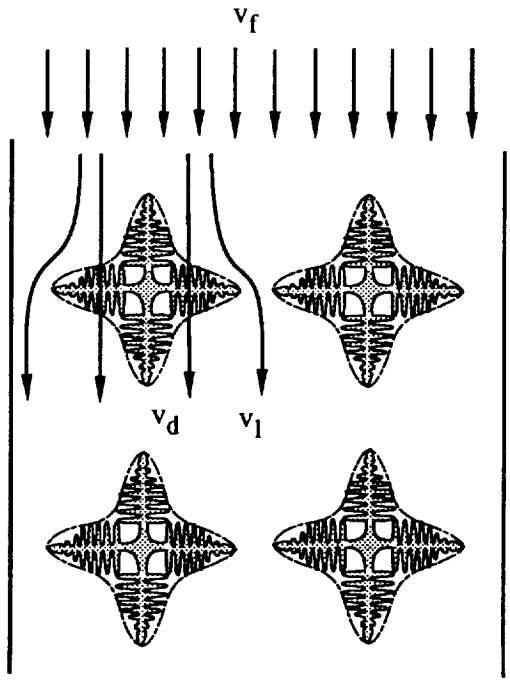

Fig. 31

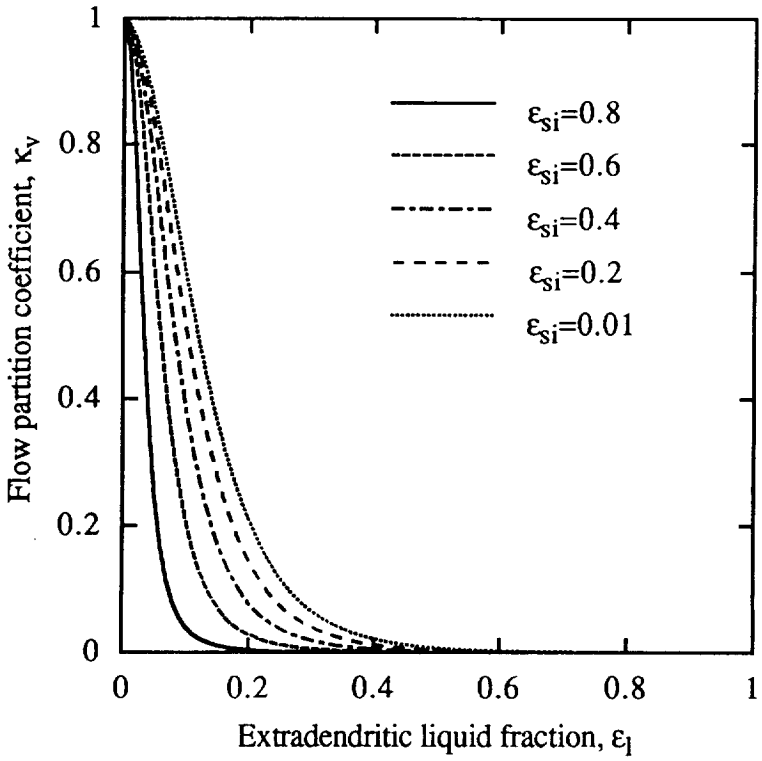
Flow partition coefficient, κ_v
Extradendritic liquid fraction, ε_l
ε_{si}=0.8
ε_{si}=0.6
ε_{si}=0.4
ε_{si}=0.2
ε_{si}=0.01
0
0.2
0.4
0.6
0.8
1

Fig. 32

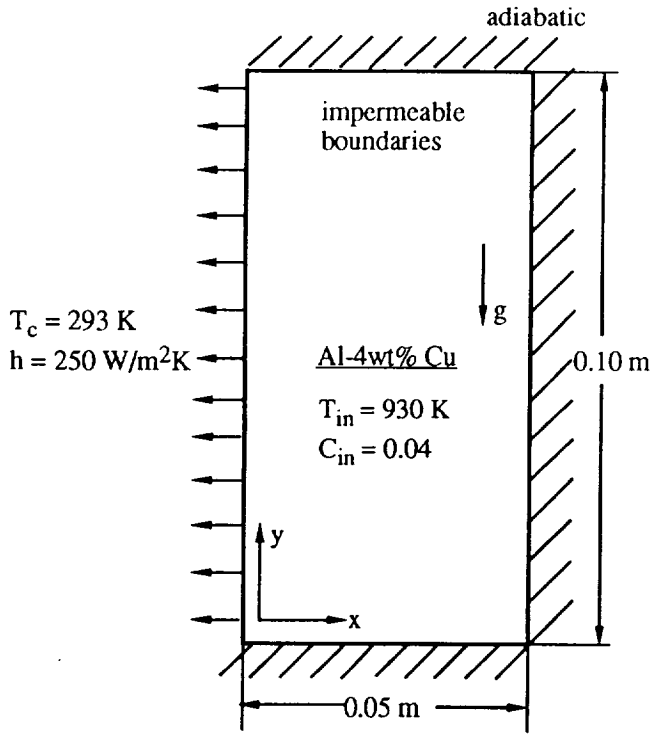

Fig.6.2 Schematic of the simulation system

Fig. 33

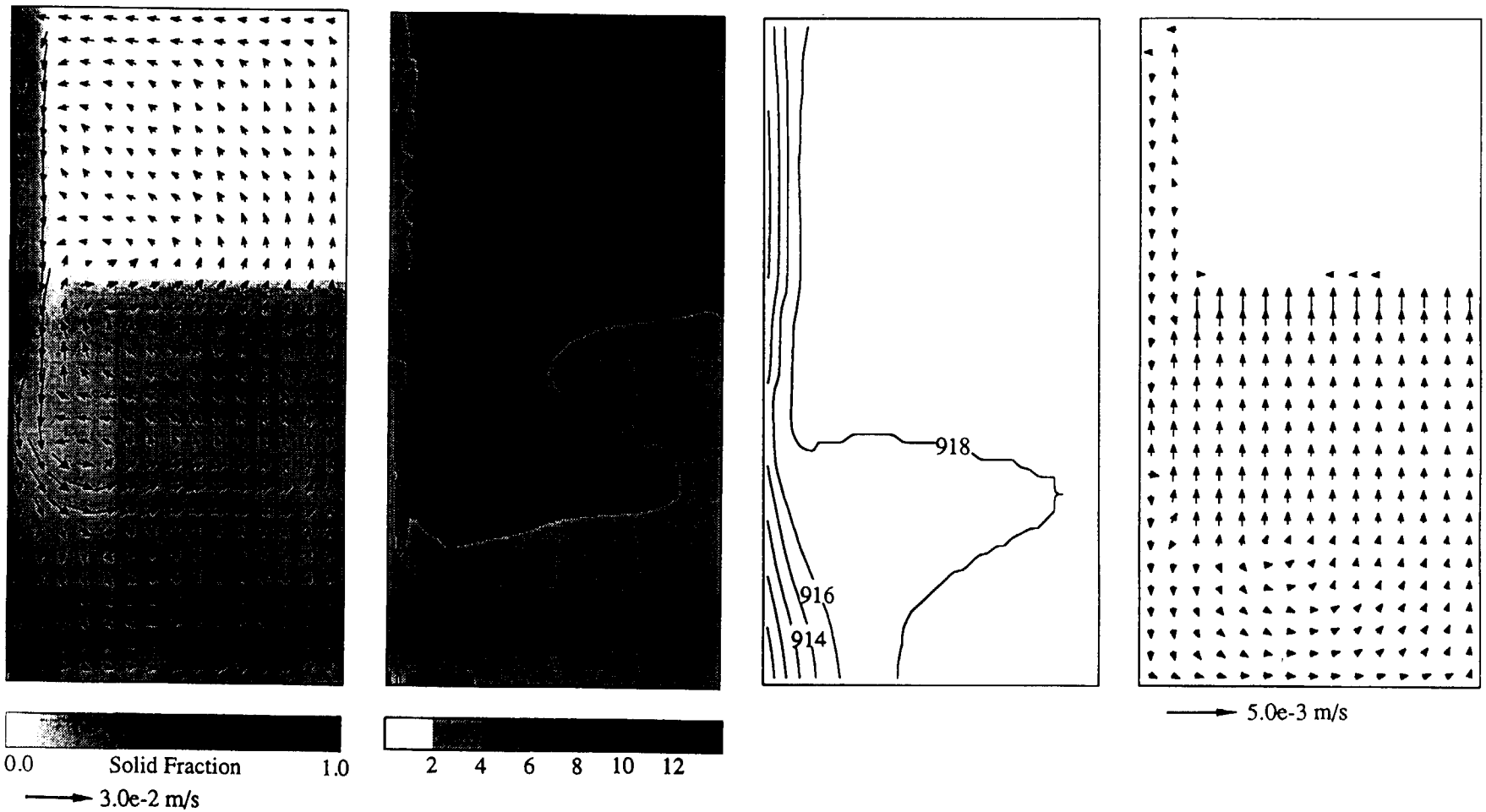

(a) Solid fraction/liquid velocity (b) Mixture concentration [wt%] (c) Temperature [K] (d) relative velocity

Fig. 34

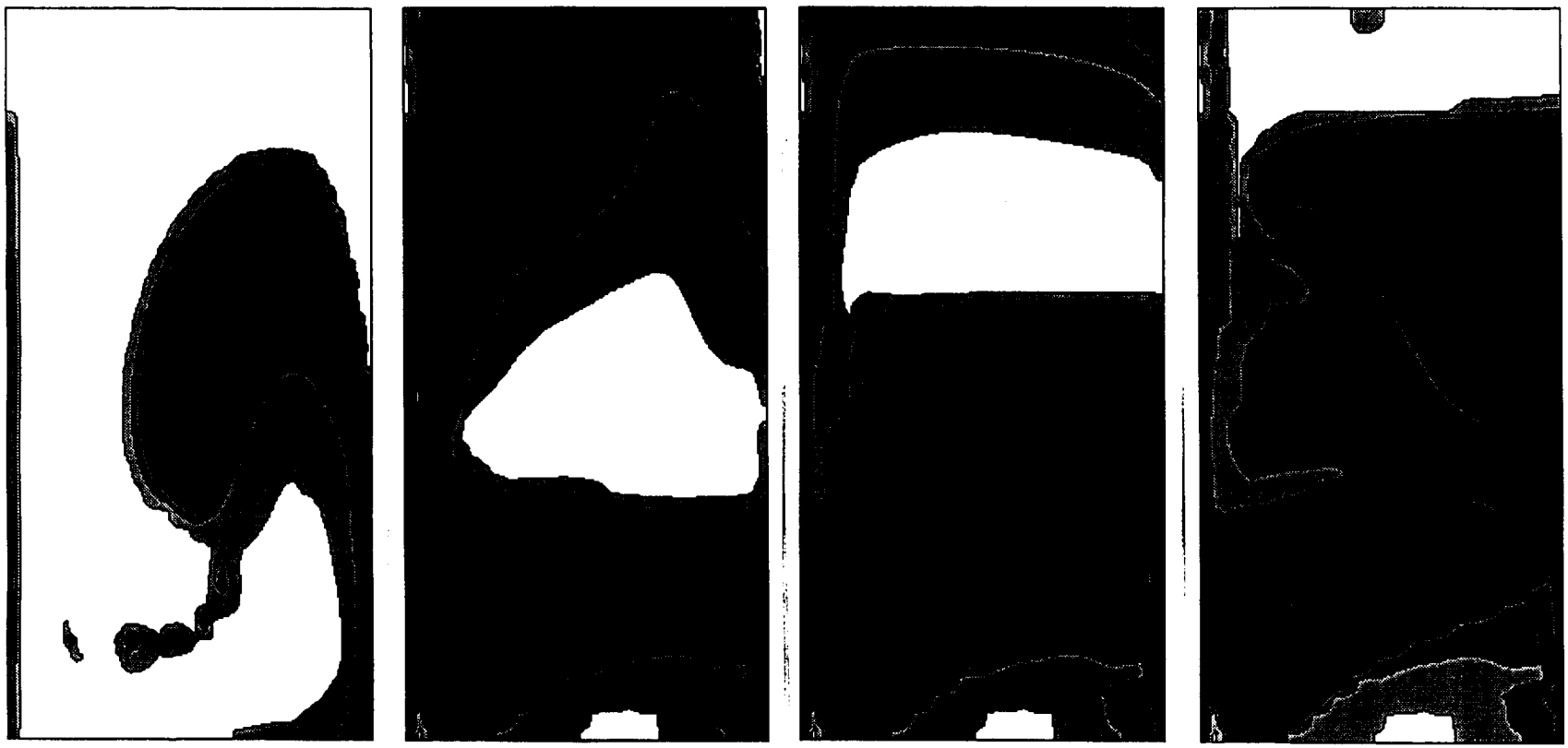

(a) t=10 s (b) t=30 s (c) t=50 s (d) t=100 s

Fig. 35

Fig. 29

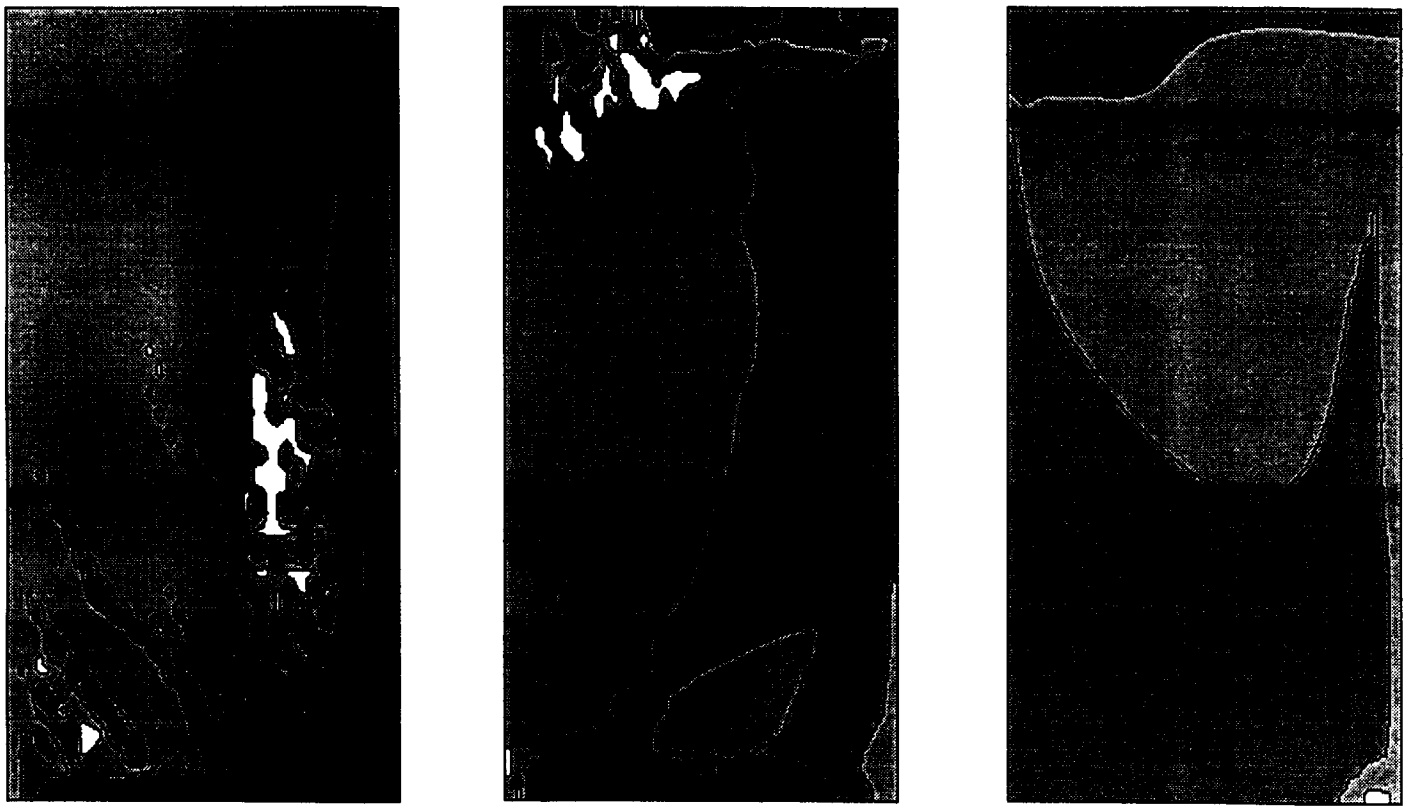

Fig. 37

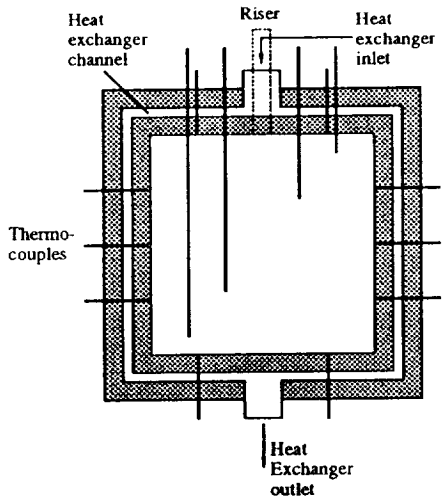
Heat
exchanger
channel
Riser
Heat
exchanger
inlet
Thermo-
couples
Heat
Exchanger
outlet

(a)

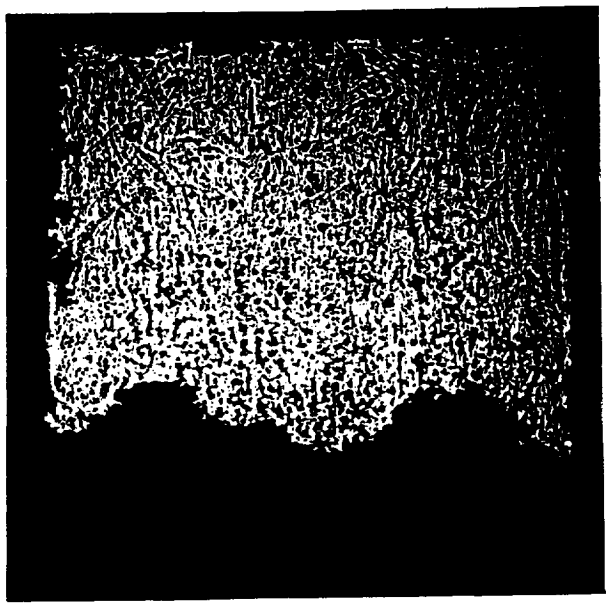

(b)

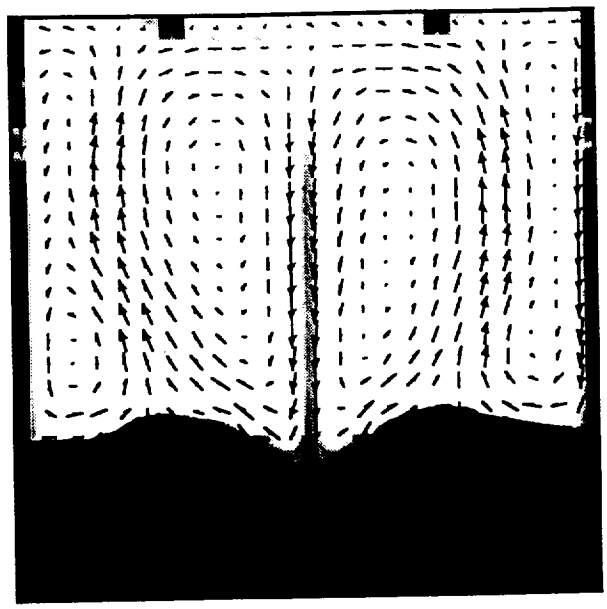

(c)

Fig. 38